TEMPORAL DYNAMICS IN *C. elegans* DEVELOPMENT AND STRESS RESPONSE

TEMPORAL DYNAMICS IN *C. elegans* DEVELOPMENT AND STRESS RESPONSE

Dissertation

for the purpose of obtaining the degree of doctor
at Delft University of Technology
by the authority of the Rector Magnificus Prof. dr. ir. T. H. J. J. van der Hagen
chair of the Board for Doctorates
to be defended publicly on
Wednesday 31 March 2021 at 12:30 o'clock

by

Olga FILINA

Master of Science
Technische Universität Dresden, Germany
born in Petrozavodsk, Russia.

This dissertation has been approved by the promotors.

Composition of the doctoral committee:

Rector Magnificus,	chairperson
Prof. dr. G. H. Koenderink,	Delft University of Technology, promotor
Dr. J. S. van Zon,	AMOLF, copromotor

Independent members:

Prof. dr. ir. S. J. Tans,	Delft University of Technology,
Prof. dr. H. Grosshans,	University of Basel, Switzerland,
Prof. dr. ir. B. M. T. Burgering,	UMC Utrecht
Dr. M. Olmedo,	University of Seville, Spain
Dr. G. J. Stephens,	Vrije Universiteit Amsterdam
Prof. dr. A. M. Dogterom,	Delft University of Technology, reserve member

AMOLF physics of functional complex matter

The work described in this thesis was performed at AMOLF, Science Park 104, 1098 XG Amsterdam, The Netherlands. This work is part of the Netherlands Organisation for Scientific Research (NWO).

ISBN 978-94-6332-746-6

CONTENTS

1

INTRODUCTION

1.1. THE ROLE OF TIME IN BIOLOGY

Time is a key aspect of all processes in life, from the millions of years of evolution, to the microseconds of biochemical reactions. Cells and organisms have evolved processes that are remarkably timed. For example, circadian rhythms, driven by an endogenous clock oscillating at a ~24-hour period, allow organisms to anticipate day-night changes and are found in nearly all organisms on earth [1, 2].

Proper and accurate timing is of utmost importance in development [3]. In order to ensure the correct body formation, many physiological processes need to be carefully orchestrated in time and space, including cell division, differentiation and migration. For instance, vertebrates utilize an elegant molecular oscillator, termed the segmentation clock, to generate a precise number of somites, which are precursors of various tissues in the segmented vertebral column [4]. The number of somites and their size are determined by the rate of the segmentation clock compared to the overall rate of development [5]. Another astonishing example of precise timing is found in periodical cicadas, insects that spend more than a decade underground in larval form and emerge from the ground as adults all at once in massive numbers, every 13 or 17 years depending on the breed [6]. A more familiar example is the onset of puberty in humans, which is known to be determined (in part) genetically and similarly regulated over a very long time scale [7, 8]. These examples illustrate the importance and ubiquity of precise temporal regulation.

Though the regulation of developmental timing has been studied in great detail in many organisms, many open questions remain. How is the correct sequence of events maintained during development, such that they always occur in the right order relative to each other? Do organisms also measure the absolute time and if so, through which mechanisms?

1.2. DEVELOPMENTAL CHECKPOINTS AND STRESS RESPONSE

During development, organisms may encounter a wide range of conditions, external or internal, that are unfavourable and thus do not support normal developmental progression. Organisms evolved elaborate mechanisms to deal with such unpredictable situations. For example, on the cellular level various checkpoints regulate progression through the cell cycle, ensuring that important events such as DNA replication have been completed correctly before the cell is ready to divide [9]. Similarly, there is evidence that multicellular organisms use checkpoints to coordinate the developmental progression on the body-wide level [10–15]. Such checkpoints represent an opportunity to reversibly arrest development, waiting for unfavourable conditions to resolve. For example, fruit fly *Drosophila* undergoes metamorphosis only upon attaining a certain critical weight, while arresting development under conditions of insufficient nutrient intake that prevent growth [10, 16]. Bypassing this important checkpoint requires activation of the insulin/insulin-like growth factor-1 signalling (IIS) pathway, which is directly linked to nutrient availability and becomes deactivated upon starvation [16]. These examples illustrate that decision whether to continue or arrest development is tightly linked to the molecular pathways that sense the physiological stress and issue an appropriate body-wide response.

Despite the IIS pathway being extensively studied in multiple biological systems, it remains unclear how exactly it senses environmental conditions such as nutrient availability and convert it to an appropriate developmental decision. Moreover, it is unknown how the decision to arrest development is coordinated throughout the body, such that all cells and organs are impacted in the same way.

1.3. VARIABILITY IN BIOLOGY

It is known that genetically identical individuals exhibit variations in phenotype and behaviour, even when environmental factors and overall life history are the same. Such variation is thought to emanate from the stochastic nature of biochemical processes within the cells, largely due to the small number of molecules involved [17, 18]. In the recent years, thanks to improvements in long-term imaging of single cells and organisms, molecular noise and its implications has been uncovered in diverse biological systems [17, 18]. For example, molecular noise in the *E. coli* chemotaxis network leads to variability in swimming behaviour of individual bacteria, which possibly underlies an adaptive strategy [19]. Another example is the budding yeast transcription factor Crz1, which undergoes stochastic bursts of nuclear localization in response to the external calcium stress [20]. These stochastic nuclear translocations allow Crz1 to effectively transmit information about the extracellular calcium concentration to its downstream genes, coordinating their expression in a manner proportional to stress.

One may wonder what is the impact of variability at the single-cell level on developmental timing. For instance, molecular noise could alter the order of developmental events that occur close together in time. If so, do organisms employ strategies to mitigate such stochastic and possibly fatal disruptions in development? When studying developmental processes and their regulation in time, it is thus particularly important to take into account the individual variability.

1.4. *C. elegans* AS A MODEL SYSTEM

An important model system for studying the regulation of timing and stress response is the nematode worm *Caenorabditis elegans*. Since its choice by Sydney Brenner in the sixties [21], *C. elegans* has been extensively used as a model organism to study a wide range of physiological phenomena and processes, from neural networks [22] to cell polarity [23] and aging [24]. These studies led to numerous breakthroughs and discoveries, such as the description of genes that control apoptosis [25], discovery of microRNAs [26] and RNA interference [27], to name a few. In 1998 *C. elegans* became the first multicellular organism to have its genome sequenced, firmly establishing itself as a go-to genetic model [28].

The qualities that make *C. elegans* so appealing for research are, among others, its anatomical simplicity and the ease of maintenance in the laboratory setting. *C. elegans* proliferate as self-reproducing hermaphrodites, producing a large number (~300) of progeny that are genetically identical. Conveniently, the ability to generate males in the lab also enables genetic crosses. Thanks to its small size (~1 mm long for an adult) and transparent body, *C. elegans* is uniquely suited for microscopy, as it is possible to use fluorescent markers for *in vivo* observations of cellular processes. Finally, many components of genetic pathways are conserved between *C. elegans* and higher organisms, including humans, making it a relevant model organism to study mechanisms associated with human diseases [29]. *C. elegans* is particularly well suited to study developmental processes, due to its short and robust (post-)embryonic development, as well as its fixed number of somatic cells (959 for an adult hermaphrodite) and their fully mapped lineages [30, 31].

1.5. *C. elegans* DEVELOPMENT

The development of *C. elegans* is divided into embryonic and post-embryonic development, with the latter being the focus of this thesis. Post-embryonic development progresses through four larval stages that comprise both unique and recurring developmental events and are punctuated by molts (Fig. 1.1). Each larval stage starts with a period of active feeding and growth, is followed by a sleep-like state (lethargus) where the new cuticle is synthesised, and finally terminates with shedding of the old cuticle (ecdysis) and progression to the next larval stage or, eventually, adulthood [32]. Many recurring developmental processes occur in a manner that is tightly coupled to this cycle of larval progression. Examples of such processes include divisions of seam cells, stem cell-like cells that divide once every larval stage (with an extra proliferative division in L2) to give rise to more seam cells as well as differentiated hypodermal or neural cells. The periodic nature of development is also manifested by the oscillations in the expression of a multitude of genes, where gene transcripts peak once per larval stage, albeit at different times [33–35].

C. elegans is an ideal model organism to study the timing of larval development, as the control of timing has been extensively studied on the genetic level. In partic-

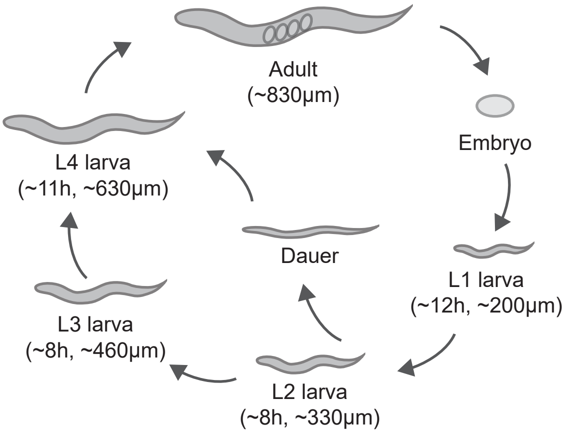

Figure 1.1: *C. elegans* life cycle. Cartoon illustration of *C. elegans* life cycle, which starts as an embryo, followed by post-embryonic development consisting of four larval stages (L1-L4), finally becoming a mature fertile adult. Transitions between the larval stages require molting - a process of cuticle remodelling. An alternative, long-lived developmental stage, dauer, is formed in response to unfavourable environmental conditions. The duration of larval stages with the corresponding body lengths (measured at the beginning of each stage) correspond to wild-type animals developing at 23 °C.

ular, genetic screens have revealed many mutants with specific perturbations in the developmental timing, called heterochronic mutants. Heterochronic genes encode proteins and small non-coding RNAs (microRNAs) that act as molecular switches to promote stage-specific developmental programs and regulate stage-to-stage transitions [36–38]. Heterochronic mutants typically cause stage-specific events either to occur precociously, in an earlier larval stage, or to be reiterated in subsequent stages. The heterochronic pathway thus ensures the correct order of developmental progression. One particular heterochronic gene, *lin-42*, is thought to play a crucial role in the regulation of developmental timing, as it negatively regulates the transcription of multiple key microRNAs [39–41], and its defects are associated with severely perturbed development [42].

Interestingly, the rate of post-embryonic development in *C. elegans* is highly flexible and depends strongly on environmental conditions, such as food availability and diet. For example, dietary restriction extends the duration of larval stages as much as ten-fold, without resulting in apparent defects in development [43]. How timing of cell-level events is adapted in response to such changes in external conditions remains poorly understood.

When conditions become too severe (complete lack of food, high temperature or population density), *C. elegans* can halt its developmental progression by transforming itself into dauer, a long-lived morphologically distinct larvae optimized for survival, and resume development upon the return to normal conditions [44, 45]. Entry into dauer is timed to occur precisely at the end of the second larval stage, with the decision to enter dauer taking place one stage earlier [45]. In addition to dauer diapause, other checkpoints at which development can transiently and reversibly arrest have been identified in every larval stage as well as in early adulthood [12, 46]. The common feature of these checkpoints is that they occur at a particular time early in the molting cycle and are not associated with morphological changes, unlike dauer larvae. The arrest at these checkpoints is regulated by the IIS pathway [12, 46]. In addition to its role in developmental arrest, this pathway also ensures that the correct, highly specific response is mounted to a wide range of stresses, including starvation, heat or osmotic stress [47], yet how it achieves this task remains unknown.

1.6. THESIS OUTLINE

This thesis focuses on the following open questions in *C. elegans* biology: i) how the timing of individual events is adjusted when the total duration of development is extended due to external conditions and ii) how the IIS signaling pathway discriminates between different types of stress in order to issue a tailored, stress-specific response. To address these questions, it is necessary to monitor individual *C. elegans* animals over extended periods of time. However, while embryonic development has been extensively studied in *C. elegans*, post-embryonic development represents a challenge for long-term time-lapse microscopy, as animals actively move around in order to feed. Therefore, reliable methods to image motile larvae at the single cell resolution are necessary to ensure future progress in *C. elegans* biology.

In Chapter 2, we introduce a time-lapse microscopy technique used throughout this thesis that allows studying diverse processes in post-embryonic development of *C. elegans*. This technique combines single-animal confinement, fast image acquisition and (semi-) automated image analysis to follow single cells inside individual developing larvae. We further show two proof-of-principle applications: studying cell lineages and oscillatory gene expression dynamics in individual animals.

In Chapter 3, we combine this imaging technique with phenomenological mathematical models to study how the timing of developmental events adjusts under environmental conditions and in mutants that alter the rate of developmental progression. In particular, we measure the timing of three recurring developmental processes (seam cell divisions, gene expression oscillations and ecdysis). We uncovered striking variability in the timing of these events between individual isogenic animals developing in the same environment. Moreover, we found pervasive changes in timing at the population level when environmental conditions, such as temperature and diet, were varied. Surprisingly, all variation in timing between individuals and environmental conditions was explained by temporal scaling, i.e. in all cases events occurred at the same time when measured relative to the duration of total development. Unexpectedly, we observed that *lin-42* mutants developed with highly perturbed and variable timing, yet the timing of events we measured was still explained by temporal scaling.

Finally, in Chapter 4, we use our time-lapse technique to explore how *C. elegans* responds to external stresses that do not support normal developmental progression and cause early developmental arrest. In particular, we investigate the dynamics of DAF-16, a transcription factor downstream of the IIS pathway, in response to diverse physiological stresses, namely starvation, heat and osmotic stress during the L1 arrest. We find that, in contrast to the current paradigm, DAF-16 undergoes pulsatile translocations between the nucleus and the cytoplasm in response to constant levels of stress. Strikingly, pulses are synchronized between different cells along the body. Moreover, we find that DAF-16 pulses adopt unique dynamics depending on the type and magnitude of the external stress, suggesting a potential strategy to generate a tailored response. Finally, we observe similar stochastic pulsatile dynamics in DAF-16 homologue FOXO3a in human cells under low nutrient levels, suggesting that translocation pulses are a general and so far unrecognized feature of insulin signalling.

2

LONG-TERM TIME-LAPSE MICROSCOPY OF *C. elegans* POST-EMBRYONIC DEVELOPMENT

We present a microscopy technique that enables long-term time-lapse microscopy at single-cell resolution in moving and feeding Caenorhabditis elegans larvae. Time-lapse microscopy of C. elegans post-embryonic development is challenging, as larvae are highly motile. Moreover, immobilization generally leads to rapid developmental arrest. Instead, we confine larval movement to microchambers that contain bacteria as food, and use fast image acquisition and image analysis to follow the dynamics of cells inside individual larvae, as they move within each microchamber. This allows us to perform fluorescence microscopy of 10-20 animals in parallel with 20 minute time resolution. We demonstrate the power of our approach by analyzing the dynamics of cell division and gene expression over the full 48 hours of development from larva to adult. Our approach now makes it possible to study the behavior of individual cells inside the body of a feeding and growing animal.

This Chapter is adapted from N. Gritti, S. Kienle, **O. Filina**, J.S. van Zon. (2016) *Long-term time-lapse microscopy of C. elegans post-embryonic development*, Nature Communications 7.1: 1-9. [48]

2.1. INTRODUCTION

Recent advances in microscopy have made it possible to follow the dynamics of many, if not all cells in the development of entire zebrafish and fruit fly embryos [49]. However, in these model organisms time-lapse microscopy is typically restricted to early stages of embryonic development. Due to their small and transparent anatomy, nematode such as *Caenorhabditis elegans* are currently the only animals where the entire development from embryo to adult can in principle be studied with single-cell resolution [30, 50–52]. This also makes *C. elegans* uniquely suited to study the interplay between development and environmental cues such as diet, food availability and pheromones [53–55].

However, long-term time-lapse microscopy is currently rarely used to study *C. elegans* post-embryonic development. This is because *C. elegans* larvae are highly motile and thus difficult to image at high magnification. Immobilizing larvae either mechanically or by paralysis-inducing drugs allows time-lapse microscopy only for limited time periods, as it prevents the animal from feeding, resulting in developmental arrest within hours [56, 57]. Microfluidics has been used to immobilize nematodes for microscopy by mechanical clamping [58, 59], flow [60, 61] or changes in the physicochemical environment [62–64], but most of these devices are geared towards immobilizing adult nematodes and are not designed to support sustained development. Experiments that did support normal larval growth so far lacked the resolution to study development at the single-cell level [43, 65, 66].

To perform time-lapse microscopy of *C. elegans* post-embryonic development we instead use a different approach (Fig. 2.1): first, we constrain larval movement to the field of view of the microscope, using microfabricated hydrogel chambers containing bacteria as food. Next, we use fast image acquisition to capture sharp images of larvae as they move inside each microchamber, precluding the need for immobilization altogether. Finally, we use image analysis to track the dynamics of cells inside the animal's body. Microchambers have two main advantages over active microfluidics: first, they are simple to use, requiring no moving parts or flow. Second, in contrast to microfluidics, microchambers do not require using liquid culture. Instead, animals move and feed under conditions similar to standard *C. elegans* culture on agar plates and the established microscopy protocols for studying nematode development [30]. Hydrogel microchambers have been used to constrain nematode movement for studying behavior [67] but so far not development.

Here we show that, using arrays of microchambers, we can perform fluorescence microscopy of developmental dynamics in 10-20 animals simultaneously, with 20 min time resolution for the full 48 h of post-embryonic development. To demonstrate the power of our approach we measured, in single animals, the dynamics of i) seam cell divisions and ii) molting cycle gene expression oscillations, processes that because of their ~ 30 – 40 h duration were so far inaccessible for immobilization-based time-lapse microscopy. The control of cell division and gene expression is the hallmark of development and our analysis shows that the dynamical information captured by our approach can provide new insight into the mechanisms that control these processes. In general, we expect that the ability to follow individual cells in freely moving and growing animals will provide an unprecedented view on development.

2.2. RESULTS

To constrain *C. elegans* larvae to the field of view of the microscope, we microfabricated 250 × 250 × 20 μm chambers in a 10% polyacrylamide hydrogel (Fig. 2.1A). We created 10 × 10 microchamber arrays from a master mold created with standard soft-lithography techniques (see Methods). To fabricate chambers we used polyacrylamide rather than agarose hydrogels, as used previously [67], because in our hands thin polyacrylamide layers were less brittle and easier to handle [68]. We filled chambers with a single *C. elegans* egg and *E. coli* OP50 bacteria as food (see Methods). Subsequently, we clamped the polyacrylamide microchamber array between a standard microscope slide and a glass coverslip to prevent the sample from drying during the experiment.

Upon hatching, larvae moved and fed inside the microchambers (Fig. 2.1C). Larval movement can be fast (peaking at 50 μm·s^{-1} for reversals). To minimize larval movement during image acquisition, we optimized our microscopy setup for short acquisition times (Fig. 2.1B). First, we used LED trans-illumination and laser epi-illumination to reduce exposure times to 1-10 ms. Second, we used a fast piezo Z-stage to scan the microchamber in the axial direction. Together, this enables us to acquire Z-stacks of 20-30 Z-slices with two imaging channels in <500 ms. By combining a sCMOS camera with large camera chip (2048 × 2048 pixel, 6.5 × 6.5 μm per pixel) with a high numerical aperture 40X objective we could image the entire microchamber (~ 250 μm) while still resolving subcellular features (~0.3 μm for 1.3 N.A.). By moving between individual chambers in the microchamber array using an X-Y motorized stage, we routinely imaged 10-20 larvae in a single imaging session. In addition, we integrated a temperature control system to enable experiments at different temperatures (see Methods and Chapters 3, 4).

We observed that after hatching individual larvae developed into adult animals over the course of ~ 40 h, without leaving the chamber (Fig. 2.1D). To confirm that the observed growth corresponded to normal development, we measured two markers of developmental progression. *C. elegans* development is divided into four larval stages, labeled L1-L4. Animals molt at the end of each larval stage, an event called ecdysis. We first measured, for each animal, the time of all ecdyses, marked by the appearance of an old cuticle inside the chamber (Fig. 2.1E). The observed average duration of each larval stage (average and standard deviation are 11.1±0.2 h, 7.3±0.2 h, 7.1±0.3 h and 10.2 ± 0.4 h for L1-L4) agreed with established values under standard culturing conditions [69]. Second, we measured body length extension as a function of time (Fig. 2.1E). We found that body length varied between individual time points, likely reflecting the deformability of the animal's body. However, on average we observed that body length increased with a fixed, larval stage-dependent rate, with pauses in growth observed prior to molts, as observed before [43, 69]. Body length extension in microchambers agreed well with growth as observed on standard agar plates and occurred with limited compression of the animal in the vertical direction, (Fig. S2.1). Moreover, the body length at the start of each larval stage agreed well with previous measurements [69]. Together, this showed that *C. elegans* larvae developed normally inside our microchambers.

We found significant animal-to-animal variability, both in timing of ecdysis and body

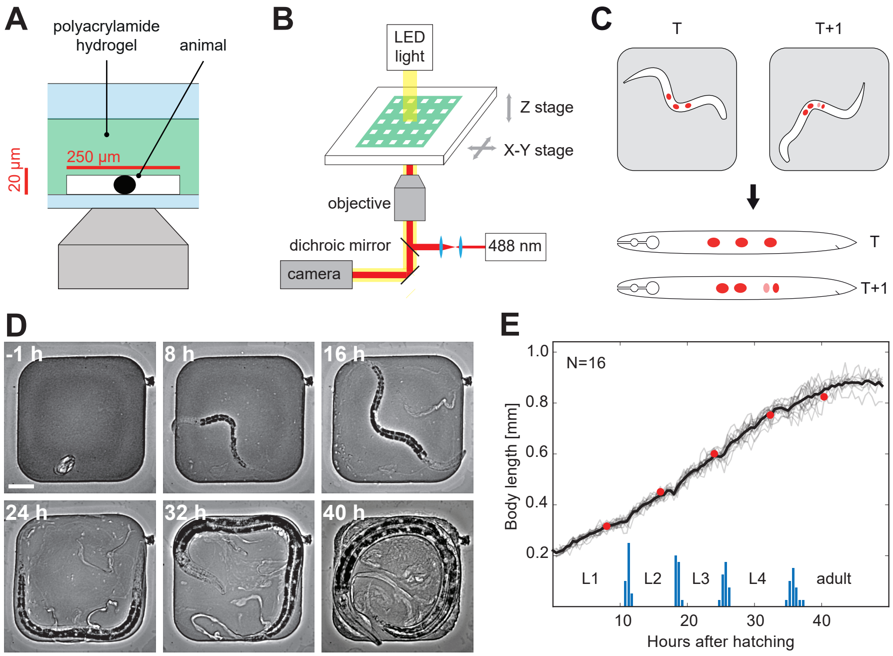

Figure 2.1: Imaging development of nematodes in polyacrylamide microchambers. **(A)** Schematic cross-section of a single microchamber. The hydrogel layer is clamped between a cover slip (blue, bottom) and a cover glass (blue, top). **(B)** Imaging setup. To image animals moving within microchambers, we used LED and laser illumination to achieve short (1-10 ms) exposure times and a fast piezo Z-stage to move rapidly between imaging planes. To image multiple animals in parallel, an X-Y motorized stage cycled between individual microchambers in a microchamber array (green). **(C)** Image analysis. For each image, the body axis and positions of fluorescently labeled cells (red) are manually annotated. Cell positions are then converted to body axis coordinates to allow systematic comparison between time points. Finally, cell divisions, cell movements or changes in gene expression are recorded. **(D)** Images of a single growing animal in a 250 x 250 x 20 μm microchamber. Time is indicated in hours after hatching. Old cuticles, which are shed at the end of each larval stage (L1-L4), are also visible. Scale bar, 50 μm. **(E)** Body length (grey lines for individual animals and black line for population average) and fraction of animals in ecdysis (blue bars) as a function of time for $N = 16$ animals. Red markers correspond to the body length of the animal shown in Panel (D). Time of ecdysis is defined by the appearance of a newly shed cuticle in the microchamber.

length extension (Fig. 2.1E), even in animals imaged simultaneously. Similar variability was observed recently in *C. elegans* larvae developing in liquid culture [43]. However, to exclude that this variability was due to insufficient food in the microchambers, we also quantified timing of ecdysis and body length extension in animals contained in larger microchambers (290 × 290 × 25 μm) (Fig. S2.1A). We observed no changes in the dynamics of development nor a decrease in animal-to-animal variability. This suggested that the observed variability is intrinsic to *C. elegans* development.

2.2.1. SEAM CELL LINEAGE

Because of its invariant cell lineage, *C. elegans* is uniquely suited to study the genetic control of cell lineages [30, 70]. However, obtaining lineages remains laborious as it relies on manual observation over extended time periods. To test whether our setup could simplify lineage analysis, we used it to study the seam cell lineage. Seam cells form a row of cells along the left and right side of *C. elegans* animals (Fig. 2.2A), that divide with a complex pattern of asymmetric and symmetric cell divisions over a ~ 40 h period [30]. Asymmetric divisions result in a new undifferentiated seam cell and a differentiated hypodermal (H1,H2,V1-V6,T) or neuronal/glial cell (H2,V5,T). In the L2 stage, this is preceded by a symmetric division that doubles the seam cell number (H1,V1-V4,V6). At the L4 molt, the remaining seam cells terminally differentiate. Because of the long duration, full seam cell lineages have never been imaged in a single animal. As a consequence, it remains poorly understood how the timing of seam cell divisions is controlled. To visualize the seam cells, we used a strain, *wIs51[SCMp::GFP]*, that carries a nuclear seam cell marker [71]. This marker is sufficiently bright that we could visualize seam cells on both sides of the body over all four larval stages (Fig. 2.2C). We detected cell divisions by the first appearance of two daughter nuclei at the position previously occupied by the mother cell. We could unambiguously assign the fate of each daughter cell, as only the seam cell daughter retained nuclear fluorescence. In this way, we could reconstruct the full lineage for all seam cells (Fig. 2.2B).

Our analysis extends the standard lineaging approach [30] by providing the exact time of each division relative to the time of hatching, allowing us to study variation in timing both between seam cell lineages and, within each lineage, between animals. We compared the average cell division timing between the different lineages (Fig. 2.2D). We measured, at each larval stage, the division time of each individual seam cell with respect to the average division time of all seam cells in the same animal. We found that seam cell divisions followed a particular sequence, with seam cells at the center of the body (V2-V4) on average dividing before those closer to the head and tail (H1,H2,V6,T). This difference in timing is most pronounced in the earlier larval stages. The main deviation from this sequence was V5, which typically divided first in the L1 and L2 larval stage. However, we observed significant variability around the mean division times (Fig. 2.2D), leading to deviations from the average sequence. For instance, in 3/16 animals other seam cells divided before V5 at the L1 stage (Fig. S2.2). We also observed significant animal-to-animal variability in division time within seam cell lineages (Fig. 2.2E), with typical standard deviations of ~ 0.3 h. Such quantitative measurements of average timing and variability can contribute towards understanding the cues that trigger seam cell divisions.

2.2.2. OSCILLATORY GENE EXPRESSION

So far, we used fluorescence only to determine cell position. We next tested whether we could also quantify fluorescence intensity as a measure of gene expression dy-

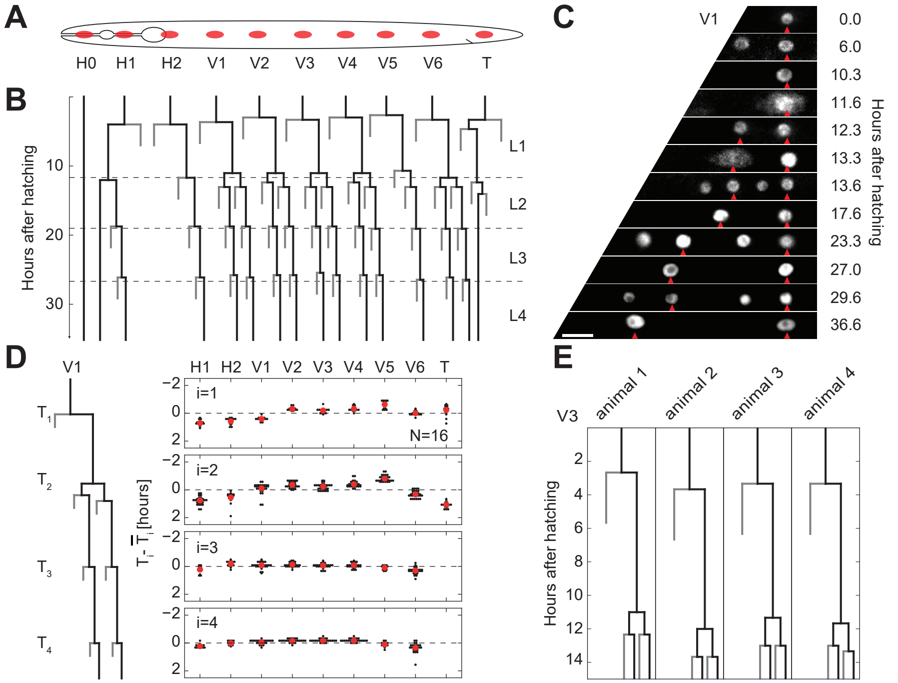

Figure 2.2: Seam cell lineage. **(A)** Position of seam cells (in red) along the body axis. **(B)** Example of seam cell lineages measured in a single animal. Black lines represent seam cells and grey lines differentiated cells. Dashed lines indicate time of ecdysis, separating the different larval stages, L1-L4. Divisions are indicated at the exact time of occurrence, with 20 min resolution. **(C)** Image sequence of the V1 lineage in a single animal carrying a *wIs51[SCMp::GFP]* nuclear seam cell marker. Seam cell nuclei are indicated by red arrows. Other nuclei belong to hypodermal cells. Images were computationally straightened and aligned to the posterior-most seam cell. Scale bar, 10 μm. **(D)** Analysis of cell division timing. For each seam cell division i, we plot the relative division time $T_i - \overline{T}_i$ (black markers), where T_i is the cell division time and $\overline{T}_i$ is the division time averaged over all nine lineages, H1-T, on both sides of the animal. Also shown is the relative division time averaged over all animals (red markers). **(E)** Animal-to-animal variability in cell division time in the first three divisions of the V3 lineage.

namics, focusing on the oscillatory expression of molting cycle genes. Dynamic regulation of gene expression is essential for development. A striking example is provided by the molting cycle genes in *C. elegans*, whose expression peaks once every larval stage [72]. Moreover, recent RNA-sequencing experiments found that many genes exhibited oscillatory expression in phase with the molting cycle [33, 57]. However, so far such gene expression oscillations were characterized at the population level, but not in single animals or single cells. Hence, it is not known with what precision the period of the oscillations is controlled and how strongly they are synchronized within the body.

First, we characterized the expression dynamics of the molting cycle gene *mlt-10*, which is essential for molting and expressed in the hypodermis only during the molt. We studied a transcriptional reporter strain, *mgIs49[mlt-10p::GFP-PEST]*, used previously to characterize *mlt-10* expression dynamics at the population level [72]. We could follow expression dynamics in the *mlt-10* reporter for all four larval stages, with a clear pulse in fluorescence intensity observed close to each ecdysis. To study the spatiotemporal *mlt-10* expression dynamics, we quantified both the average fluorescence intensity along the A-P axis (Fig. 2.3A,B) and the total fluorescence intensity (Fig. 2.3C) as a function of time. We found that the oscillatory dynamics was uniform, i.e. with a phase independent of A-P position (Fig. 2.3A,B). We observed significant animal-to-animal variability in the exact timing of the *mlt-10* expression peak (Fig. 2.3D, 28 ± 1 h for the L3 peak). However, *mlt-10* expression dynamics was tightly correlated with the subsequent ecdysis (Fig. 2.3E, peaking 1.1 ± 0.1 h before L3 ecdysis).

The *mlt-10* reporter was expressed in many cells. To test whether we could follow expression dynamics with single cell resolution, we also measured *wrt-2* expression dynamics. The gene *wrt-2* is expressed exclusively in seam cells [73] and was recently found to exhibit oscillatory gene expression at the population level in the L3-L4 stage [33]. We followed *wrt-2* expression in *heIs63[wrt-2p::H2B::GFP, wrt-2p::PH::GFP]* animals, where GFP is targeted both to the seam cell nucleus and membrane [74]. We found that the fluorescence signal was bright enough to visualize expression in seam cells on the side of the animal closest to the objective, but not on the opposite side, likely due to light scattering in the intervening tissue (Fig. S2.4). As animals sometimes flip from one side to the other around the molt [75], we could not follow single seam cells over the entire course of development. However, focusing only on the seam cells closest to the objective, we could clearly observe oscillations in *wrt-2* expression in single seam cells over all four larval stages (Fig. 2.3F). To quantify *wrt-2* expression, we measured the total nuclear fluorescence intensity in the seam cells V1-V5 as a function of time (Fig. 2.3G). We found that both the period and phase of *wrt-2* oscillations agreed with previous measurements of *wrt-2* mRNA dynamics [33]. Moreover, *wrt-2* oscillations were strongly correlated even between seam cells such as V1 and V5, that reside in different parts of the body (Fig. 2.3H). Similar to *mlt-10* expression oscillations, we observed that, while there existed significant animal-to-animal variability in the exact time of the *wrt-2* expression peaks (Fig. 2.3D, I, 26 ± 1 h for the L3 peak), the expression peaks were nevertheless precisely timed with respect to the ecdysis (Fig. 2.3E, peaking 1.5±0.4h before L3 ecdysis). In general, for both *mlt-10* and *wrt-2* we find that, despite clear animal-to-animal variability, the

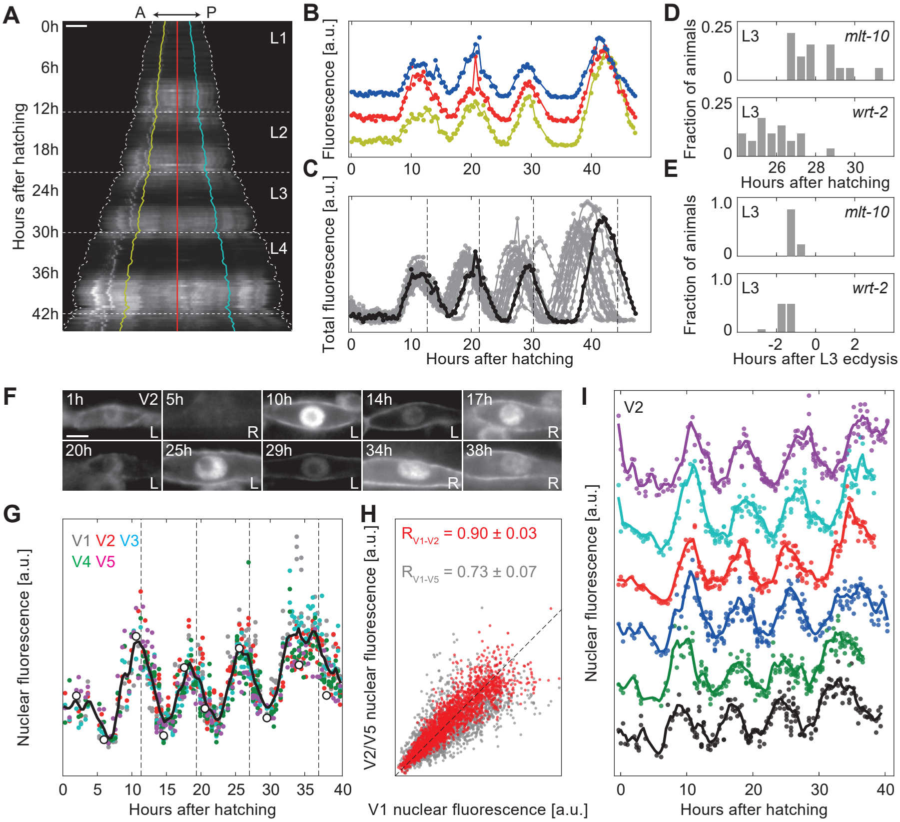

Figure 2.3: Oscillatory gene expression. **(A)** Kymograph of *mlt-10* expression along the A-P axis as a function of time in a single *mgIs49[mlt-10p::GFP-PEST]* animal. Dotted lines represent the position of head and tail and horizontal dashed lines represent ecdysis. Colored lines indicate the regions evaluated in Panel (B). Scale bar, 100 μm. **(B)** *mlt-10* expression oscillations at different A-P positions for the animal in Panel (A). **(C)** *mlt-10* expression integrated over the entire animal as a function of time for $N = 15$ animals. The *mlt-10* expression dynamics (black line) and time of ecdysis (dashed lines) are indicated for the animal in Panel (A). **(D, E)** Time distribution of the L3 peak in *mlt-10* ($N = 15$) and *wrt-2* ($N = 23$) expression relative to (D) time of hatching and (E) time of L3 ecdysis. **(F)** *wrt-2* expression oscillations in the posterior-most V2 seam cell in a *heIs63[wrt-2p::H2B::GFP, wrt-2p::PH::GFP]* animal. Time is hours after hatching. The label indicates whether the cell is the left (L) or right (R) V2 cell. Scale bar, 5 μm. **(G)** Single-animal *wrt-2* expression oscillations. White markers correspond to the images in Panel (F). The black line represents a sliding average with 2 h window size over V1-V5. **(H)** Correlation in *wrt-2* expression between the V1 and V2 (red) and V5 (grey) cells. Markers and correlation coefficient R are for $N = 23$ animals over all larval stages. **(I)** *wrt-2* expression oscillations in the V2 seam cell lineage in different animals. Lines correspond to sliding average with 2 h window size.

timing of expression peaks was tightly coupled to ecdysis and was strongly correlated between cells at different positions. This suggests that molting cycle gene expression and ecdysis are under strong global control.

2.3. DISCUSSION

Here, we describe a technique to perform time-lapse microscopy in moving *C. elegans* larvae, with single-cell resolution and for the full duration of post-embryonic development. We achieved this by using hydrogel microchambers that confine animal movement to the field of view of the microscope while containing sufficient food for development. Due to our use of high N.A. objectives, our approach is comparable in spatial resolution to existing immobilization-based time-lapse microscopy techniques, although the requirement for short exposure times to image moving animals makes it more challenging to combine with confocal microscopy to increase the axial resolution. We can envision several ways in which to expand on the design of our setup. For example, it could be combined naturally with RNA interference, by filling microchambers with bacteria that express the desired dsRNA [76]. Additionally, a separate microfluidic layer on top of the hydrogel chambers could be used to change the local chemical environment [68] in <10 min to deliver environmental cues, e.g. dauer pheromone, at precisely timed developmental stages.

We used our technique to study processes that, because of their long duration (30-40 h), had been inaccessible for time-lapse imaging: seam cell divisions and molting cycle gene expression oscillations. We were able to perform detailed analysis of the timing, kinetics and variability in these processes, an approach that can be extended to many other developmental processes in *C. elegans*. We typically imaged 10-20 animals per imaging session, even though, in principle, the combination of short (<1 s/animal) acquisition time and 20 min interval between acquisitions allows for hundreds of animals to be imaged simultaneously. This is because the bottleneck was formed by the manual annotation of the animal's body axis and cells. For the studies presented in Chapters 3 and 4, we developed automated image analysis tools to ease this process. We believe that our setup could make long-term time-lapse microscopy a routine technique to study *C. elegans* post-embryonic development, with the potential to significantly increase our understanding of lineage control, morphogenesis and regulation of gene expression.

We thank Allison Frand for providing us with *C. elegans* strains.

2.4. METHODS

2.4.1. C. ELEGANS CULTURE AND STRAINS

All C. elegans strains were cultured at 20 °C on NGM agar plates with OP50 bacteria. Wild-type nematodes were strain N2. The following mutations and integrated transgenic arrays were used: LGIV: *mgIs49 [mlt-10p::GFP-PEST]* [72], LGV: *wIs51 [SCMp::GFP]* [71], *heIs63 [wrt-2p::GFP::PH; wrt-2p::GFP::H2B]* [74].

2.4.2. MICROCHAMBER FABRICATION

Microfabricated arrays of chambers were made from a master mold as described in Ref. [68]. Master molds were created using standard soft-lithography techniques. Briefly, SU-8 2025 epoxy resin (MicroChem) was first spin-coated on a silicon wafer to form a 20 μm layer. The SU-8 layer was exposed with UV-light through a foil mask (SELBA S.A.) containing the micropattern (Fig. S2.5). Microchamber dimensions are $250 \times 250 \times 20$ μm for all experiments, unless specified otherwise. To create polyacrylamide microchamber arrays from the master mold, a 10% dilution of 29:1 acrylamide/ bis-acrylamide was mixed with 0.1% ammonium persulfate (Sigma) and 0.01% TEMED (Sigma) as polymerization initiators. The resulting aqueous solution was then poured in a cavity placed on top of the micropatterned silicon wafer. The cavity was closed with a silanized coverslip and sealed by mechanical clamping, allowing the solution to polymerize for 2 h. To remove the toxic unpolymerized acrylamide monomers, the resulting polyacrylamide microchamber arrays were washed at least three times for at least 3h each in distilled water. Fewer or shorter washing steps often resulted in developmental arrest. Microchamber arrays could be stored in distilled water for ~ 15 days. Single microchamber arrays were placed in M9 buffer for 4 h directly prior to timelapse imaging.

2.4.3. SAMPLE PREPARATION

To prepare the sample, a glass spacer with the same height as the polyacrylamide membrane was attached to a 76 × 26 × 1 mm microscope slide using high vacuum grease (Dow Corning). A single microchamber array was positioned with tweezers on the microscope slide, with the openings of the microchambers facing up. Excess liquid was removed with a tissue. With a pipet, drops of M9 buffer (~ 40 μl in total) were placed on the side and on the surface of the microchamber array, while preventing the liquid from filling the chambers. To load C. elegans embryos into the microchambers we followed the approach in Ref. [67]. Under a dissection microscope, a drop of bacterial suspension containing a single late-stage embryo was transferred from a NGM agar plate seeded with OP50 bacteria into a microchamber, using an eyelash attached to a Pasteur pipet. To facilitate the release of the bacteria and embryo into the chamber, the eyelash was dipped briefly into the M9 drop prior to touching the microchamber. Once the egg was transferred, more bacterial suspension was added to the microchamber using the eyelash, until completely filled. For each experiment, around 10-20 chambers were loaded. Subsequently, tissue paper was used to remove all excess M9 buffer. Finally, a 25 × 75 # 1 coverslip was lowered on the chambers to seal the sample, slow enough to avoid forming large air bubbles. The sample was placed on a custom fabricated holder and clamped to seal the chambers and avoid liquid evaporation during the duration of the experiment (Fig. S2.5).

2.4.4. MICROSCOPY IMAGING

We performed timelapse imaging on a Nikon Ti-E inverted microscope. Using a large chip camera (Hamamatsu sCMOS Orca v2), it was possible to fit single microchambers in the field of view of the camera while using a 40X magnification objective (Nikon CFI Plan Fluor 40X, NA=1.3, Oil immersion). Transmission imaging was performed using a red LED (CoolLED pE-100 615 nm) while fluorescence images were acquired using a 488nm laser (Coherent OBIS LS 488-100). The laser beam was expanded from 0.7 mm to 36 mm through a telescope composed of two achromatic lenses of 10 and 500 mm focal lengths (Thorlabs AC080-010-A-ML and AC508-500-A). The expanded beam was then aligned through additional dielectric mirrors (Thorlab BB2-E02) to enter the back aperture of the microscope. A tube lens (300 mm focal length, Thorlabs AC508-300-A) was used to focus the beam in the back focal plane of the objective. For fluorescence microscopy, we used a dual band filter set (Chroma, 59904-ET). An XY motorized stage (Micro Drive, Mad City Labs) was used to move between chambers, while a Z piezo stage (Nano Drive 85, Mad City Labs) was used to move the sample in the Z direction. To optimize acquisition speed, we synchronized the camera, laser illumination and stage movement as follows: to operate the rolling-shutter camera in global exposure mode, the laser beam was switched on (rise time <3 μs) once all the lines on the camera chip were active and switched off once the camera started reading out the chip. In order to rapidly acquire Z-stacks, we synchronized the piezo Z stage and the camera, so that the stage moved to the new Z position during the 10 ms that the camera read out the chip to its internal memory. The microscope and all its component were controlled with custom software implemented using a National Instruments card (PCIe-6323) installed on a computer with a solid state drive (Kingston V300-120GB), an Intel Core i7 processor (3.50 GHz) and 16 GB of RAM. By using sufficiently high laser power (80-100 mW) we could use exposure times that were short enough (1-10 ms) that animal movement during acquisition was negligible. Acquiring a single imaging volume, typically consisting of 20 Z-slices in two channels, took <0.4 s. Some animal movement along the A-P axis was observed between Z-slices, particularly in L3-L4 larvae directly after the molt. Each chamber was imaged every 20 min for ~ 48 h. We found that shorter time intervals sometimes led to larvae arresting in the L1 larval stage. During imaging intervals, we used the Perfect Focus system of the microscope to prevent sample drift. Images were acquired in a temperature-controlled room at 22 °C.

2.4.5. TEMPERATURE CONTROL

In order to enable experiments at different temperatures (see Chapters 3, 4), an additional temperature control system was implemented. A thermoelectric chiller (Thermotek T257P) was used to cool or heat up the custom made objective jacket by circulating an antifreeze fluid (a mixture of water and glycerin) between the chiller and the objective jacket. In order to calibrate the system (Fig. S2.4C), a thermocouple temperature sensor measuring 0.025 mm in diameter (RS Pro) was placed inside the sample in contact with the polyacrylamide hydrogel and connected to a digital thermometer (RS Pro). The temperature was then varied on the thermoelectric chiller while the resulting temperature inside the sample was being monitored.

2.4.6. IMAGE ANALYSIS

Custom Python software was used to analyze the acquired images. For all experiments, we used the transmitted light images to record the time of hatching and ecdysis as well as the body length. We obtained the body axis by manually selecting 10-20 points on the animal's center line and subsequently fitting a spline curve $\overline{x}(s)$ to these points, with s the arc length of the spline curve along the A-P axis (Fig. S2.5A). The body length was then given by the length of $\overline{x}(s)$. This coordinate transformation was also used to create the computationally straightened images of animals in Figs. 2.1, 2.2, 2.3. At each point along the A-P axis, the D-V axis was defined by orthogonal segments 50 μm long (Fig. S2.5B). The $\overline{r} = (x', y')$ coordinates of each point P' in the original image are then converted into the (s', t') coordinates in the A-P and D-V reference system. The A–P position was given by the arc length s that minimized the distance between $\overline{r}$ and $\overline{x}(s)$. Next, the magnitude of the D–V position t was given by this minimal distance and the sign of t was defined so that $t < 0$ for the ventral side (Fig. S2.5).

2.4.7. SEAM CELLS

The seam cells were identified by their position along the A-P axis. Initiation of cell division could be observed by the loss of nuclear fluorescence due to nuclear envelope breakdown. The division time was given by the first appearance of two smaller daughter nuclei at the old position of the mother cell.

2.4.8. MOLTING CYCLE GENES

For *mlt-10* expression, mean fluorescence intensity as function of A-P position s was obtained by averaging the fluorescence over a D-V window of $\mid t \mid < 60$ μm. The expression dynamics at different A-P position was determined by integrating fluorescence intensity over a region of 5% of body length, centered at positions at 25%, 50% and 75% of body length. To measure *wrt-2* expression in single seam cells, we manually labelled the nuclei of the V1-V5 seam cells on the side closest to the objective. As the size and shape of the nuclei changed over time, we used an image segmentation algorithm (Otsu's method) on a 5×5 μm region around each nucleus to obtain a mask of the nucleus. We then computed the mean fluorescence intensity of the pixels within this mask. To detect the time of peaks in *mlt-10* and *wrt-2* gene expression, we applied a Gaussian filter with width of 1 h to each fluorescence intensity time series and obtained for each larval stage the time at which the averaged timeseries exhibited its maximum.

2.5. SUPPLEMENTARY FIGURES

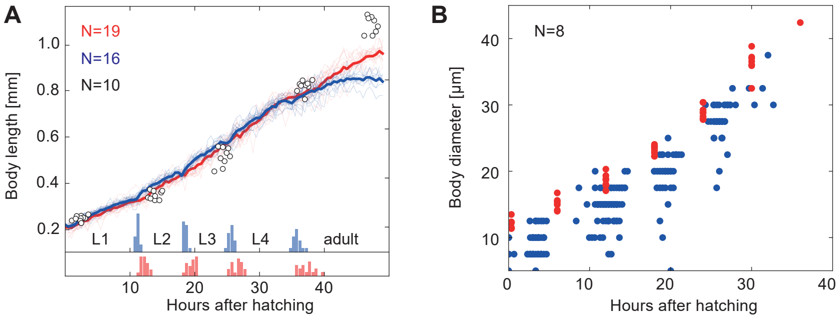

Figure S2.1: Dependence of growth and developmental timing on microchamber dimensions. (A) Body length (thin lines for individual animals and thick lines for population averages) and fraction of animals in ecdysis (bars) as a function of time for animals grown in 250 × 250 × 20 μm (blue) and 290 × 290 × 25 μm (red) microchambers. White markers represent body length of single animals grown on standard agar plates. Time of ecdysis is defined by the appearance of a newly shed cuticle. For animals on agar plates, we singled embryos onto 3.5 cm NGM agar plates spotted with *E. coli* OP50 and detected hatching time by visual inspection. Every 12 hours, we manually imaged animals with 40X or 10X objectives and measured body length. We observed only limited difference in dynamics between growth in the two different microchambers and on agar plates, for all larval stages. The slowdown of growth upon reaching adulthood observed in microchambers, as compared to agar plates, visually coincides with the depletion of food. Finally, the variability in developmental dynamics is not reduced in the larger microchambers, as compared to the standard microchambers. **(B)** Measure of the animal diameter in the vertical/Z direction(blue) and horizontal/XY direction (red). To quantify deformation of animals in 250 × 250 × 20 μm microchambers, we used the strain *wIs51[SCM::GFP]* (see Seam cell lineage section in the main text) and measured the distance between left-right pairs of the V3 seam cell as a measure of the dimension of the body in the Z direction. We quantified XY dimensions by measuring the dorsal-ventral distance in the center of the body in the transmitted light images. We find that for animals older than 20 hours, the average XY dimension (32.5 μm) is only 20% larger than the Z dimension (25.8 μm). This shows that the hydrogel deforms to accommodate the larger (> 20 μm) body width of older larvae, with only modest compression of the body in the vertical direction.

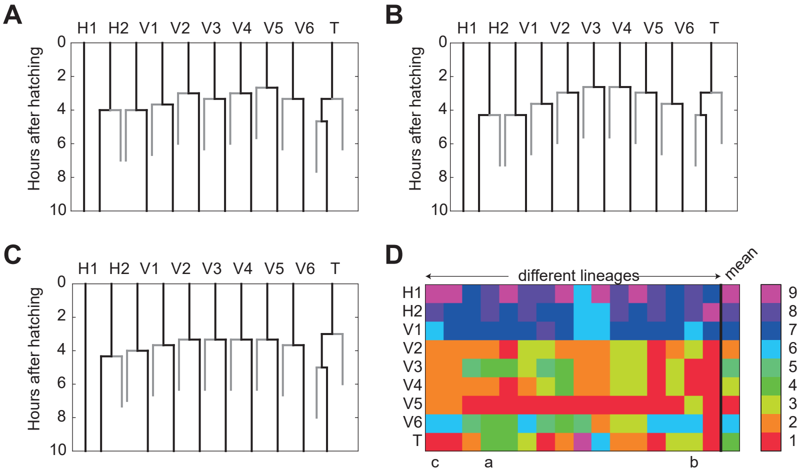

Figure S2.2: Variability in the sequence of seam cell divisions. (A), (B), (C) Examples of animals with a typical (A) and atypical sequence (B, C) of seam cell divisions in the L1 larval stage. In Panel (A), V5 divides first. In Panel (B), V3 and V4 divide simultaneously 20 minutes before V5. In Panel (C), T divides first. **(D)** Colormap showing the sequence of seam cell divisions in the L1 larval stage, for two sides (left/right) in $N = 8$ animals. Cells are color coded according to division sequence. The last column represents the mean division sequence. The columns labeled with (A), (B) or (C) correspond to the lineages shown in the corresponding panels.

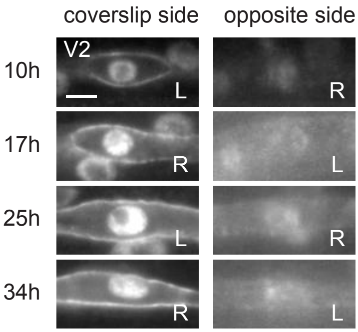

Figure S2.3: Dependence of single-cell fluorescence on cell position.‘ Images of seam cells in the V2 lineage at the time of each *wrt-2* expression peak. Time is hours after hatching. Left column: seam cell closest to the objective. Right Column: corresponding seam cell on the other side of the sample. Scale bar, 5 μm. The label indicated whether the seam cell is on the right (R) or left (L) side of the animal.

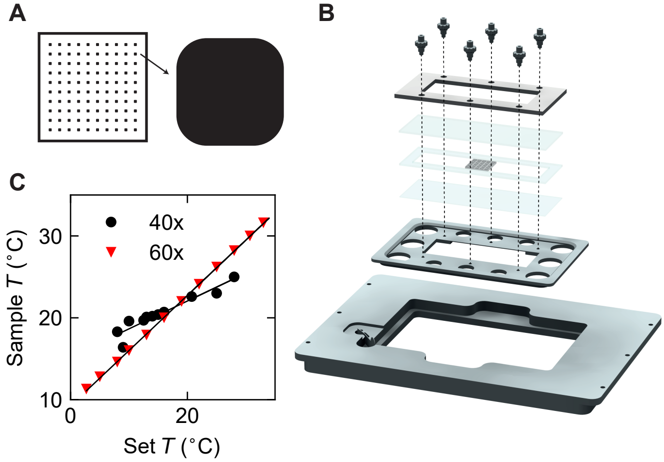

Figure S2.4: Design of microchambers and sample preparation. **(A)** Design of mask for the microchamber array. For both microchamber dimensions used here (250 μm and 290 μm), the distance between the centers of adjacent microchambers was 800 μm. Microchambers have rounded corners, as sharp corners often trapped the head of the animal, for reasons unknown to us, thereby preventing the animal from feeding. **(B)** Overview of sample holder and sample preparation. The microchambers array (in the center of the image) is sealed in between a coverslip (blue, bottom) and a standard glass slide (blue, top), using a glass spacer with the dimensions of a normal glass slide (blue, middle). Using screws, the sample is then clamped between two metallic holders. To facilitate rapid movement of the piezo Z-stage, the metal parts are made of aluminum and contain holes to reduce their weight. The sample in its holder is then placed on the Z-stage (bottom). **(C)** Temperature control calibration for the 60X (red triangles) and 40X (black circles) objectives. A thermocouple temperature sensor measuring 0.025 mm in diameter (RS Pro) was placed inside the sample in contact with the polyacrylamide hydrogel and connected to a digital thermometer (RS Pro). The temperature was then varied on the thermoelectric chiller while the resulting temperature inside the sample was being monitored. Deviations between the set and sample temperatures likely arise from heat losses through the objective and the circulation tubes. The different calibration trend between both objectives can be due to the different surface-area of contact between the objective and the objective jacket (smaller for the 40X objective, which makes heat transfer less efficient).

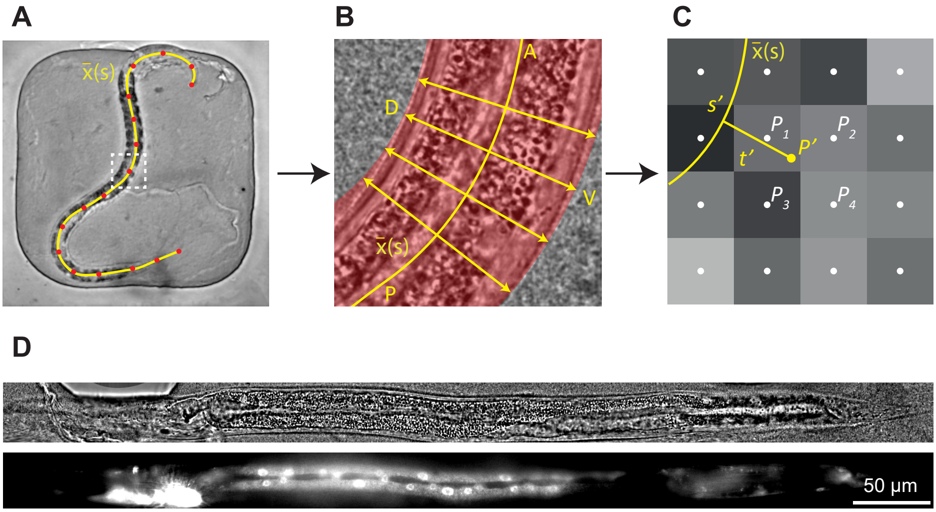

Figure S2.5: Straightening algorithm. **(A)** Average projection of a single transmission stack of a *mgIs49[mlt-10p::GFP-PEST]* animal. Red dots indicate manually selected points, yellow line indicates the spline curve fitted to the red dots. **B** Detailed view of the image enclosed by white dashed square in Panel A. Orange region indicates the part of the image containing the animal. Yellow arrows in the orthogonal direction to the spline curve indicate the dorsal-ventral (D-V) direction of the animal's body at different anteroposterior (A-P) positions. **C** Schematic overview of the interpolation algorithm. P_i indicates pixels in the (x, y) coordinate system. P' indicates the pixel in the (s, t) coordinate system. As P' does not coincide exactly with any of the pixels P_i, the value of P' was determined by 2D interpolation of the neighbouring pixels P_i. **D** Single computationally treated image corresponding to the animal shown in Panel A. Top image: transmission illumination, bottom image: fluorescence intensity. Figure from Nicola Gritti.

3

TEMPORAL SCALING IN *C. elegans* LARVAL DEVELOPMENT

It is essential that correct temporal order of cellular events is maintained during animal development. During post-embryonic development, the rate of development depends on external conditions, such as food availability, diet and temperature. How timing of cellular events is impacted when the rate of development is changed at the organism-level is not known. We used a novel time-lapse microscopy approach to simultaneously measure timing of oscillatory gene expression, hypodermal stem cell divisions and cuticle shedding in individual animals, during C. elegans larval development from hatching to adulthood. This revealed strong variability in timing between isogenic individuals under the same conditions. However, this variability obeyed 'temporal scaling', meaning that events occurred at the same time when measured relative to the duration of development in each individual. We also observed pervasive changes in population-averaged timing when temperature, diet or genotype were varied, but with larval development divided in 'epochs' that differed in how the timing of events was impacted. Yet, these variations in timing were still explained by temporal scaling when timing was rescaled by the duration of the respective epochs in each individual. Surprisingly, timing obeyed temporal scaling even in mutants lacking lin-42/Period, presumed a core regulator of timing of larval development, that exhibited strongly delayed, heterogeneous timing and growth arrest. Timing of larval development is likely controlled by timers based on protein degradation or protein oscillations, but such mechanisms do not inherently generate temporal scaling. Hence, our observations will put strong constraints on models to explain timing of larval development.

3.1. INTRODUCTION

Numerous cellular events that occur during animal development, such as cell division, cell movement and gene expression, must be tightly coordinated in time to allow formation of a functional organism with a correctly established body plan. However, despite our increasing understanding of the regulation of developmental timing [3, 36, 37], how cells in developing organisms measure time and execute events in the correct temporal order remains poorly understood. Moreover, the rate of postembryonic development in animals is significantly affected by external conditions, such as food availability, diet and temperature. For example, severe dietary restriction extends the duration of larval development in the nematode worm *C. elegans* as much as ten-fold, without resulting in apparent defects in development [43]. How the timing of individual developmental events is adjusted in response to such changes in the organism-level rate of development is not known.

This question about developmental timing has a parallel in the context of spatial patterning during development. It has been shown that spatial gene expression patterns often scale with organ or embryo size, i.e. with the spatial pattern adjusted in each individual organ or embryo so that the spatial features occurred at the same position relative to its overall size [77–80]. For example, in *Drosophila* embryos gap genes are expressed in bands along the anteroposterior body axis [81, 82]. These bands have highly stereotypical positions relative to the embryo's size, even though this size shows significant variability between individuals [78]. Moreover, embryos of closely related species that vary greatly in size exhibit the same number of bands with similar position relative to the size of the embryo [78]. Here, we examine whether, analogous to scaling of spatial patterns in development, the timing of development exhibits temporal scaling, meaning that, when the organism-level rate of development is changed, the timing of individual events is adjusted so that they still occur at the same time when measured relative to the total duration of development. Such a mechanism would ensure the correct synchrony of developmental events even when organism-level timing is changed in an unpredictable manner by shifts in external conditions.

Due to its invariant cell lineage and highly stereotypical development, *C. elegans* is an ideal model organism to study developmental timing. Its postembryonic development consists of four larval stages (L1-L4) that are separated by a molting event, where a new cuticle is synthesized and the old cuticle shed [32]. After the final L4 molt, animals reach reproductive maturity, marking their transition into adulthood. There is a clear periodic aspect to *C. elegans* development, with molts occurring every 8-10 hours at 25 °C. Moreover, larval stages are accompanied by genome-wide oscillatory expression of a multitude of genes, with peaks occurring once per larval stage [33, 35, 57].

Molecular mechanisms that have been proposed for regulation of developmental timing include oscillators, that encode time in periodic changes in protein level, and 'hourglass' mechanisms, that record time in the steady accumulation or degradation of proteins [83]. Developmental timing has been extensively studied in *C. elegans*, leading to the discovery of heterochronic genes [36, 37]. Heterochronic genes such as *lin-14* and *lin-28* show expression levels that decrease during larval development, suggestive of an hourglass mechanism [84, 85]. Indeed, mutations that perturb the *lin-14* and *lin-28* temporal expression patterns lead to timing defects, with events in one larval stage shifted to an earlier stage or repeated in subsequent stages [86]. At the same time, such mutations have only limited impact on developmental timing on the organism level. In contrast, the heterochronic gene *lin-42* is expressed in an oscillatory manner during development, peaking once every larval stage. In *lin-42* mutants, developmental timing is severely perturbed, with strong animal-to-animal variability in larval stage duration [42]. The body-wide, oscillatory expression dynamics of *lin-42*, together with its impact on larval stage duration, makes *lin-42* an interesting candidate for a global regulator of developmental timing. Intriguingly, *lin-42* is a homolog of *Period*, an important component of the circadian clock in *Drosophila* and higher organisms [87]. Hence, it has been speculated that *lin-42* forms part of an oscillator-based timer that allows cells and organs to read out developmental time [32].

How timing of individual events is impacted by changes in the organism-level rate of development is poorly characterized. Timing of *C. elegans* larval development is often measured at the population level, by examining the developmental stage of animals sampled from age-synchronized populations. This approach has limited time resolution and does not allow measuring timing of multiple events within the same individual. The latter is a particular problem for mutants such as *lin-42*, where developmental synchrony between individual animals is lost. However, the alternative approach of following individual animals was so far performed manually, limiting the number of animals that could be examined. We have recently developed a novel microscopy approach that allows automated imaging of individual *C. elegans* larvae during their entire development and at single-cell resolution [48], making it possible to measure timing of cellular events in many individual larvae. Here, we used this approach to simultaneously measure the timing of three recurring developmental events (oscillatory expression of a molting cycle gene, hypodermal stem cell divisions and cuticle shedding) in individual *C. elegans* larvae, both under changes in environmental conditions (temperature and diet) and in mutant animals, that increased the duration of larval development up to ~ 3-fold.

Our measurements uncovered extensive variability in event timing between individuals, even in isogenic animals under identical environmental conditions. Strikingly, this variability obeyed temporal scaling, meaning that events occurred at the same time when rescaled by the total duration of development in each individual. Moreover, changes in average timing between populations that differ in genotype or environmental conditions could not be explained by a simple change in the overall rate of development of the organism. Instead, we found larval development is divided into distinct epochs, which are sequences of events that, upon variation in conditions or genotype, exhibit changes in timing that are identical, and differ from changes in timing observed for events in other epochs. Yet, this variation in timing between populations also obeys temporal scaling, provided that event times were rescaled by the duration of individual epochs, rather than total duration of development. Surprisingly, this was even the case for a *lin-42* deletion mutant that showed strongly perturbed and highly variable developmental timing, suggesting that while *lin-42* is crucial for setting the duration of larval stages, it is dispensable for controlling event timing relative to each larval stage.

Overall, our results show that the broad variation observed between individuals, environmental conditions and genotypes in the timing of cellular events during *C. elegans* post-embryonic development can be fully captured by the simple concept of temporal scaling, thereby revealing a precise adaptation of cell-level timing to changes in the organism-level rate of development. These observations raise the important question how temporal scaling is implemented by the molecular mechanisms that control timing of larval development.

3.2. RESULTS

To examine how developmental timing is coordinated at the organism-level in developing *C. elegans* larvae, we measured the timing of multiple developmental events that occurred frequently and throughout all of larval development, focusing on seam cell divisions, oscillatory gene expression and ecdysis. Seam cells are hypodermal stem cells that divide asymmetrically once every larval stage, yielding one hypodermal cell and one seam cell (Fig. 3.1A, D) [30]. In addition, the seam cells V1-V4 and V6 undergo an additional symmetric division in the L2 larval stage, doubling their number. Oscillatory gene expression is a pervasive phenomenon in *C. elegans*, with thousands of gene transcripts oscillating during development with a periodicity corresponding to that of the molting cycle [33, 35, 57]. Here, we focused on the oscillatory gene *wrt-2*, a hedgehog-like protein expressed in seam cells, that peaks in expression once every larval stage [33, 48] (Fig. 3.1B, D). Finally, ecdysis is the shedding of the old cuticle at the end of each larval stage (Fig. 3.1C, D). By focusing on these three events, we captured qualitatively different developmental processes, while their repetitive nature allowed us to capture many events in a single experiment.

To accurately measure timing of individual events, we used a novel fluorescence time-lapse microscopy approach to follow the full ~40 h of post-embryonic development of individual *C. elegans* larvae with single-cell resolution [48]. Briefly, embryos were placed inside hydrogel chambers filled with *E. coli* as a food source. These chambers contained sufficient food to sustain development into adulthood, while constraining animals to the field of view of the microscope at each stage. By capturing fluorescence and transmitted light images with fast, 1-10 ms, exposure time, we could image developmental dynamics in individual cells inside moving larvae, without immobilizing animals. To visualize seam cell divisions, we used the strain *heIs63[wrt-2p::H2B::GFP, wrt-2p::PH::GFP]*, where green fluorescent protein (GFP) was targeted specifically to the nucleus and membrane of seam cells [74]. Since divisions of individual seam cells occurred close together in time, we defined the time of each round of divisions as the average time at which V1-V6 cells have divided or started dividing, as determined by formation of the metaphase plate. Because the reporter used to detect seam cell divisions (*heIs63*) produces GFP under control of the *wrt-2* promoter, it enabled simultaneous measurement of oscillatory *wrt-2* expression. Fluorescent images were analyzed automatically using custom-written software to extract the mean fluorescent GFP intensity in seam cell nuclei at every time frame. Finally, the time of expression peaks was extracted from the resulting oscillatory *wrt-2* expression profiles, by fitting their dynamics with a combination of Gaussian functions and a linear offset (Fig. 3.1B, Eq. 3.1 in Methods). Finally, the time of the ecdysis was defined as the time when the shed cuticle was first visible in the transmitted light image (Fig. 3.1C). For full details on data acquisition and analysis, see Methods.

3.2.1. SCALING OF DEVELOPMENTAL TIMING IN INDIVIDUAL ANIMALS

We first quantified timing of seam cell division, *wrt-2* expression peaks and ecdysis under standard conditions: wild-type animals fed *E. coli* OP50 at 23 °C (Fig. 3.1E, F). Individual animals showed strong variability in the total duration of development (~40 h), defined as the time between hatching and L4 ecdysis, with a ~10 h difference observed between the first and last animal to enter adulthood. We observed similar variability in the timing of all measured developmental events (Fig. 3.1F). For some events, such as the second *wrt-2* peak and fourth seam cell division, the magnitude of the variability was larger than the average difference in timing, raising the question how the correct order of events was maintained. Interestingly, this variability in timing was strongly correlated: when we plotted event times t_a and t_b measured in the same animal against each other, for different pairs of events a, b, all data points clustered along a line (Fig. 3.1G). This strong correlation was even present for pairs of events that are widely separated in time, e.g. the L1 seam cell division and the L4 *wrt-2* peak.

A simple argument could explain this observation. As measure of developmental progression, we first defined the phase $\phi_a = \langle t_a^S \rangle / \langle T^S \rangle$, where $\langle t_a^S \rangle$ and $\langle T^S \rangle$ are the population-averaged time of event and duration of development under standard conditions (23 °C), with $\phi = 0$ and 1 corresponding to the start of larval development and adulthood. If we now assumed that for any event a the event time t_a, measured in an individual animal, scales with the total duration of development T for that animal, $t_a = \phi_a \cdot T$, even as the duration T varies significantly between individuals, then the time at which two events a and b occur within same individual is related by $t_b = \frac{\phi_b}{\phi_a} t_a$, independent of total duration of development T in that individual. As a result, measurements for individual animals will be clustered along a line of constant $\frac{t_b}{t_a}$, as observed experimentally. Strikingly, this observation holds for all pairs of events we examined (Fig. S3.1), meaning that if an animal executed its first seam cell division earlier than the rest of the population, it was highly likely to be similarly early in executing all subsequent events for the rest of larval development, thereby ensuring the correct order of events despite the observed variability. We could reproduce these experimental results with a simple stochastic timing model (Fig. S3.2, Eq. 3.2, 3.3), if we assumed that the observed variability in timing was dominated by animal-to-animal variation in the organism-level rate of development, $1/T$, that otherwise remained constant throughout development. Overall, our results show that the measured changes in timing between individuals can be fully explained by simple rescaling with the total duration of development in each individual.

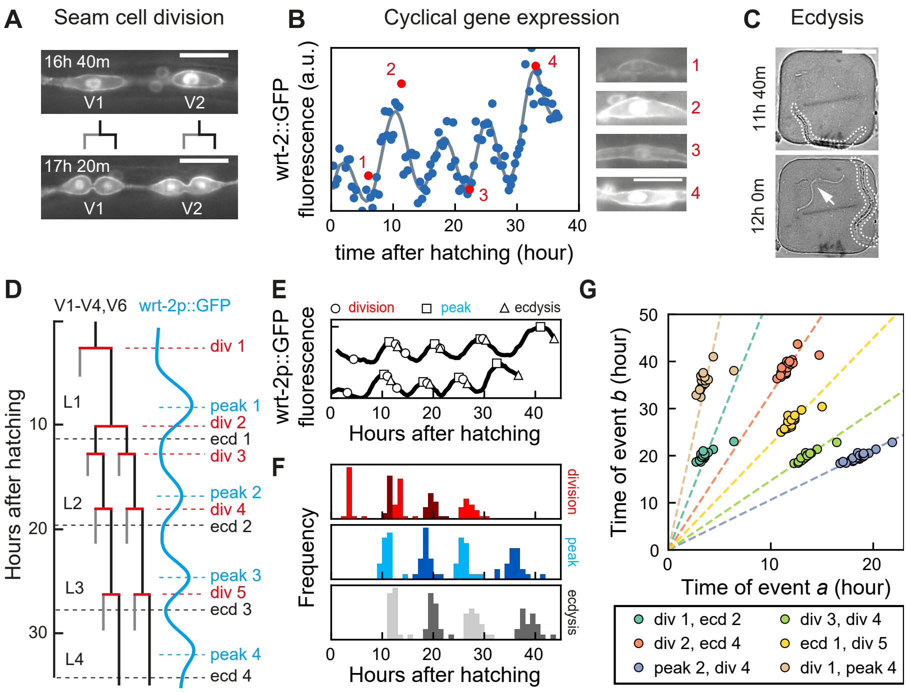

Figure 3.1: Scaling of developmental timing in individual animals. **(A)-(C)** Measuring timing of seam cell division, oscillatory gene expression and ecdysis. **(A)** Seam cells divide once or twice every larval stage giving rise either to hypodermal (grey line) or seam cell (black line) daughters. The timing of V1-V6 seam cell division was determined using the *wrt-2p::GFP::PH; wrt-2p::GFP::H2B* fluorescent reporter (*wrt-2p::GFP*). Scale bar: 15 μm. **(B)** Oscillatory *wrt-2* expression was visualized in seam cells of *wrt-2p::GFP* animals (panels 1-4, showing posterior V3 seam cell). We quantified *wrt-2p::GFP* fluorescence averaged over the V1-V6 seam cells (circles) and fitted the data to Eq. 3.1 (grey line) to determine the time of each *wrt-2* peak. Red circles are the time points in the side panels. Scale bar: 15 μm. **(C)** Time of ecdysis was determined by the appearance of a shed cuticle (arrow) away from the larva (outlined). Scale bar: 100 μm. **(D)** Schematic overview of seam cell division, *wrt-2* peak and ecdysis events during larval development. The V5 seam cell lineage differs by lacking the L2-specific symmetric division. **(E)** Example of variability in developmental timing between two wild-type animals. Markers indicate the timing of seam cell divisions (circles), *wrt-2p::GFP* fluorescence peaks (squares) and ecdyses (triangles). Tracks are shifted along the vertical axis for clarity. **(F)** Distribution of timing of seam cell divisions (red), *wrt-2p::GFP* fluorescence peaks (blue) and ecdyses (grey), measured for standard conditions, wild-type animals fed *E. coli* OP50 diet at 23 °C ($n = 21$). **(G)** Measured times of event pairs a, b for animals in (F). Each marker is an event pair measured in a single animal. Times of event pairs show temporal scaling, i.e. they lie clustered along lines of constant $\frac{t_b}{t_a}$, even as individual event times t_a and t_b show significant variability between individuals. Dashed lines are fits $t_b = s_{a,b} \cdot t_a$ to the data for each event pair.

3.2.2. SCALING OF DEVELOPMENTAL TIMING UPON CHANGES IN TEMPERATURE

Changes in environmental conditions typically increase or decrease the population-averaged duration of development, yet how timing of cell-level events is adjusted to such changes in organism-level timing is an open question. To address this, we first measured event timing in individual animals maintained at different temperatures, as the duration of larval development increases with decreasing temperatures [69]. As expected, we observed that as temperature was reduced from the standard temperature of 23 °C to 19 °C and 15 °C, the duration of larval development increased from 39 ± 2 to 57 ± 1 and 105 ± 2 hours, respectively (Fig. S3.3). Likewise, we found that individual events were delayed more strongly with decreasing temperature (Fig. 3.2A).

To examine the impact of changing temperatures on average event timing, we examined the time evolution of the developmental phase ϕ. Our earlier definition ensured that under standard conditions (23 °C) ϕ increases with constant rate $1/\langle T^S \rangle$ (Fig. 3.2B). If the total duration of development increases or decreases, e.g. due to shifting environmental conditions, $\phi(t)$ will change, so that the same developmental phase ϕ is reached at a different time t compared to standard conditions. When we measured the average time of each seam cell division, *wrt-2p::GFP* peak and ecdysis for 19 °C and 15 °C, we found that, while the phase indeed increased at a lower rate compared to 23 °C, its increase was still linear in time (Fig. 3.2B), meaning that all measured differences in average timing were explained by changes in the organism-level rate of development, $1/\langle T \rangle$.

When we examined events times in individuals, we found similar variability in timing for animals at 19 °C and 15 °C compared to 23 °C. Moreover, times of event pairs still clustered along lines, meaning that temporal scaling with inter-individual variability in the duration of development occurred also for these conditions (Fig. 3.2C). Strikingly, event pairs clustered along the exact same line independent of temperature. This is a manifestation of population-level temporal scaling, i.e. for all three temperatures events occurred at the same relative time, when rescaled with the population-averaged duration of development observed for each temperature, even as development at 15 °C was slowed ~3-fold compared to 23 °C.

We could reproduce these observations with a simple, phenomenological model ('Uniform' model, Fig. 3.3). We assumed that population-averaged changes in timing resulted from a uniformly lowered rate of development, as observed experimentally (Fig. 3.2B, 3.3A), and included both an animal-to-animal variation in this rate, that remained constant throughout development, as well as variability in the phase of each individual event (Eq. 3.3). Stochastic simulations showed that when variability was dominated by the variation in developmental rate, the times of event pairs were positioned along a line, reflecting variability in timing between individuals (Fig. 3.3B-D). Significantly, this line appeared the same as for the corresponding events under standard conditions. To test this for both model and experiments, we defined the deviation of scaling δ as the signed angle between the lines that fit the data for standard and perturbed conditions (Fig. 3.3C), with $\delta > 0$ meaning that the line for perturbed conditions has a higher slope than for standard conditions. Here, we used the difference between angles rather than slopes, as the slope diverges when the first event a occurs close to hatching, $t_a \approx 0$. Model calculations showed that for the 'Uniform' model the deviation $\delta = 0$ for all event pairs (Eqs. 3.6, 3.9), meaning that they indeed lie along the line predicted for standard conditions.

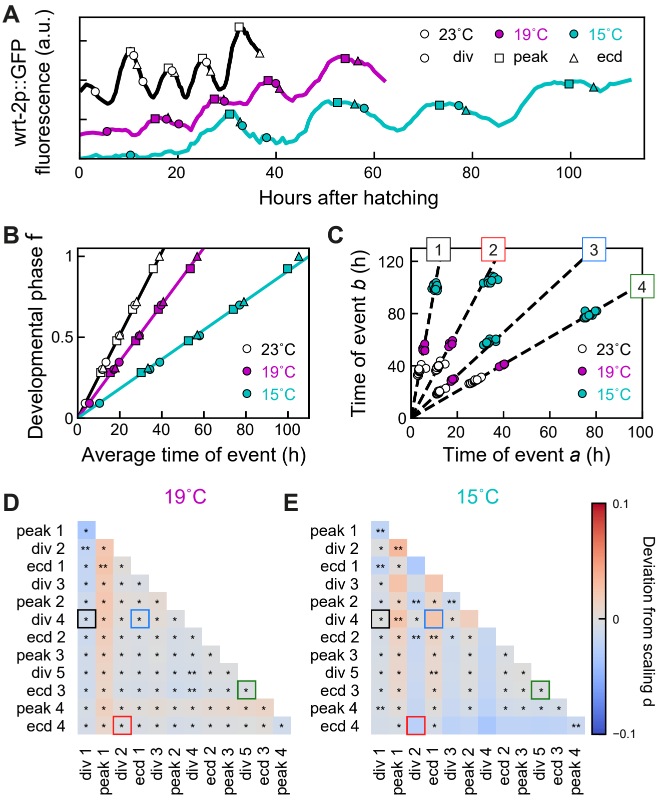

Figure 3.2: Temporal scaling of developmental timing at different temperatures. (A) Examples of developmental timing in individual animals at standard conditions (23 °C, black), 19 °C (magenta) and 15 °C (cyan). Markers indicate seam cell divisions (circles), *wrt-2p::GFP* peaks (squares) and ecdyses (triangles). **(B)** Developmental phase as function of time for different temperatures. Developmental progression is modeled as the evolution of a developmental phase ϕ in time. Each developmental event occurs at a specific phase $\phi_a = \langle t_a^S \rangle / \langle T^S \rangle$, where $\langle t_a^S \rangle$ and $\langle T^S \rangle$ are the population-averaged time of event a and total duration of development under standard conditions. With this definition, the phase for standard conditions (black line) increases linearly with rate $1/\langle T^S \rangle$. Markers indicate the subsequent events as in (A). For 19 °C or 15 °C, the phase increases linearly with the average measured event times, albeit at lower rate compared to 23 °C, with its evolution well fitted by the 'Uniform' model (magenta and cyan lines, defined in Fig. 3.3). **(C)** Measured times for different event pairs: (1) division 1 and 4, (2) division 2 and ecdysis 4, (3) ecdysis 1 and division 4, and (4) division 5 and ecdysis 3. Lines are a linear fit to data for standard conditions (23 °C). For each event pair, data measured at different temperatures cluster along the same line. This means all events occurred at the same time relative to the total duration of development, despite strong variation in this duration both between individuals and conditions. **(D),(E)** Deviation from scaling for all event pairs for development at (D) 19 °C and (E) 15 °C. In addition, stars indicate the probability that data for standard conditions and 19 °C or 15 °C observe the same scaling relation, as assessed by a Kolmogorov-Smirnov (K-S) test, *:N.S., **:$P < 0.01$, and $P < 0.001$ otherwise. For animals at 19 °C, temporal scaling was observed for all event pairs, while some significant deviations were seen at 15 °C. Colored squares correspond to event pairs in (C).

Next, we tested whether this held for our experimental observations. For each event pair a and b measured in the same individual, we calculated the angle $\theta = \arctan \frac{t_a}{t_b}$ (see Methods for details) and the deviation as $\delta = \langle\theta^P\rangle - \langle\theta^S\rangle$, the difference between the average angle for standard (S, 23 °C) and perturbed (P, 19 °C or 15 °C) conditions, with $\delta \approx 0$ indicating that the data for standard and perturbed conditions clustered along the same line. In addition, we also used the two-sample Kolmogorov-Smirnov test to estimate the probability that the θ distributions measured for standard and perturbed conditions were drawn from the same distribution. This analysis showed that most event pairs at 15 °C and 19 °C (Fig. 3.2D,E) lie along the same line as data for 23 °C, i.e. changes in timing between temperatures are fully captured by temporal scaling with duration of development.

3.2.3. BREAKDOWN OF POPULATION-LEVEL SCALING UPON CHANGES IN DIET

To test whether temporal scaling is also observed under qualitatively different changes in environmental conditions, we studied the impact of changes in food uptake and diet on timing of individual events. Total duration of development can be changed by providing animals with other food than *E. coli* OP50 [88–90]. Here, we used two different approaches. To mimic reduced food uptake, we fed the standard diet, *E. coli* OP50, to *eat-2(ad1113)* mutants that exhibit a 5-fold decrease in pharyngeal pumping and hence ingest bacteria at lower rate [91]. In addition, we grew wild-type animals on a diet of *E. coli* HB101, which was reported to have faster larval development [88].

The total duration of development was slightly different in *eat-2* mutants (40±2 h) and wild-type animals on HB101 (38 ± 1 h), compared to standard conditions of wild-type animals on OP50 (39±2 h, Fig. 3.4A, Fig. S3.3). However, we observed more complex changes in timing when we examined the average timing of seam cell divisions, *wrt-2* peaks and ecdyses (Fig. 3.4B). For *eat-2* mutants, the developmental phase increased linearly with time, with a lower rate compared to standard conditions, consistent with the 'Uniform' model. However, for animals fed HB101 the increase of phase in time could not be fit by a single constant rate. Instead, we found that development separated into multiple epochs, sequences of events that differed in how their timing was impacted by changing diet: events in the first epoch (hatching to third seam cell division) occurred with the same timing as under standard conditions, while timing in the second epoch (second *wrt-2* peak to L3 ecdysis) was best fit with the phase increasing at the same rate, but with a ~2 h delay compared to standard conditions. We constructed a phenomenological model analogous to the 'Uniform' model, that incorporated the pause separating both epochs ('Pause' model, Fig. 3.3A). When we performed stochastic simulations of the 'Pause' model (Figs. 3.3B-D, Eqs. 3.3, 3.4), we found that the times of simulated event pairs still clustered along a line, reflecting that animal-to-animal variability still obeyed temporal scaling, but one that differed from the equivalent line for standard conditions, meaning that differences in timing were not fully explained by rescaling with the population-averaged duration of development. Indeed, despite significant variability in timing between individuals, both for *eat-2* mutants and wild-type animals fed HB101, event pairs still clustered along a line (Fig. 3.4C), indicating that event times scaled with inter-individual variability

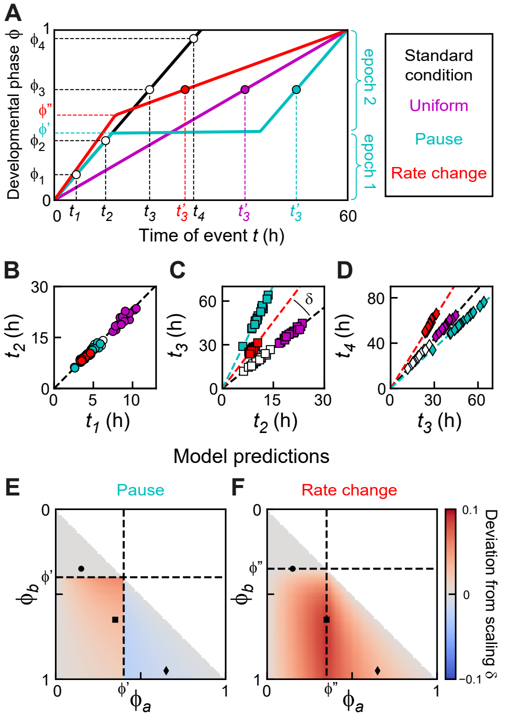

Figure 3.3: Timing models. **(A)** Developmental phase ϕ as function of time for three qualitatively different models that generate the same increase in duration of development, either by a uniform lower rate of development (magenta), a single, discrete pause at ϕ' (cyan) or a single, discrete change in the rate of development at ϕ'' (red) (Eqs. 4-5 in Methods, parameters chosen for clarity). For the 'Pause' and 'Rate change' models, the discontinuity in developmental rate $d\phi/dt$ separates development into two epochs of constant developmental rate, as illustrated for the 'Pause' model. **(B)-(D)** Simulated event times for the different event pairs indicated in (A) (Eq. 3.3). Marker color corresponds to the timing models in (A). For all models, times of event pairs are clustered along a line, i.e. occur at the same time when rescaled by each individual's duration of development. For the 'Uniform' model, times of event pairs lie along the scaling line for standard conditions (dashed line), meaning that they occur at the same time when rescaled by the population-averaged duration of development. However, the other models often deviate from this scaling line. The deviation from scaling δ is defined as the signed angle between these two lines, as indicated in (C). **(E)-(F)** Predicted deviation from scaling δ for different events pairs a and b for the 'Pause' (E) and 'Rate change' (F) model (Eqs. 3.7, 3.8, 3.9), based on experimentally measured parameters (See Methods for parameters). Black markers correspond to the event pairs in (B)-(D). These results show that the timing models in (A) can be distinguished by measuring the deviation from population-level scaling and provide a quantitative prediction for the magnitude of the deviation that can be compared directly with experiments.

in developmental duration. Interestingly, while for *eat-2* mutants these data points were positioned along the same line as standard conditions, in animals fed HB101 we found that for some event pairs most points exhibited small, but systematic deviations from this line (e.g. event pairs 2 and 3 in Fig. 3.4C), as predicted by the 'Pause' model.

To directly compare these deviations between model and experiments, we calculated the deviation from scaling δ for the 'Pause' model, with the three parameters (the rate of development, and phase and duration of the pause) constrained by our experimental measurements (Fig. 3.4B, see Methods for parameter values). Interestingly, the model predicted that these deviations occurred in a specific pattern (Fig. 3.3E): while timing of event pairs that both occurred before the developmental pause matched the line for standard conditions, deviations occurred when at least one event occurred after the pause. Event times clustered along a line with higher slope ($\delta > 0$) when one event occurred before and the other after the pause, with stronger deviations if both events were close to the pause. In contrast, when both events occurred after the pause, event times clustered along lines with lower slope ($\delta < 0$), with deviations stronger when events occurred farther apart in development. We then tested these predictions from the 'Pause' model by calculating δ for all measured event pairs. As predicted, we found a clear difference between *eat-2* mutants on OP50 and wild-type animals on HB101 (Fig. 3.4D,E). Whereas data for *eat-2* mutants largely clustered along the lines predicted by data for standard conditions, the data for animals fed HB101 showed significant deviations. Interestingly, these deviations strongly resembled, both in magnitude and sign, those predicted by the 'Pause' model, with a positive deviation when one event occurs before and the other after the pause, and a negative deviation when both occur after. This quantitative agreement implied that all deviations from scaling were due to the discontinuity in developmental rate that separated the two epochs, and that events occurred at the same time within each epoch when rescaled by the duration of that epoch in each individual.

Overall, these results show that changes in diet (HB101 instead of OP50) impact developmental timing in a manner that is more complex than rescaling with the population -averaged duration of development. However, the model suggests a simple picture that explains the experimental data: the deviations from population-level temporal scaling resulted from the pause at the mid-L2 larval stage found for animals fed HB101, with scaling observed within the two epochs separated by this pause. Moreover, each animal executes this temporal evolution of the developmental phase at an intrinsic speed that varies between individuals, giving rise to inter-individual temporal scaling for all event pairs.

3.2.4. PERTURBED DEVELOPMENTAL TIMING AND GROWTH IN *lin-42* MUTANTS

For wild-type animals on HB101 we observed deviations from temporal scaling even as diet had only minor impact on total duration of development. To seek stronger perturbations of developmental timing and, potentially, temporal scaling, we measured event timing in mutants of the heterochronic gene *lin-42*, for the following reasons. First, *lin-42* plays an important role in molting, with mutants showing longer larval

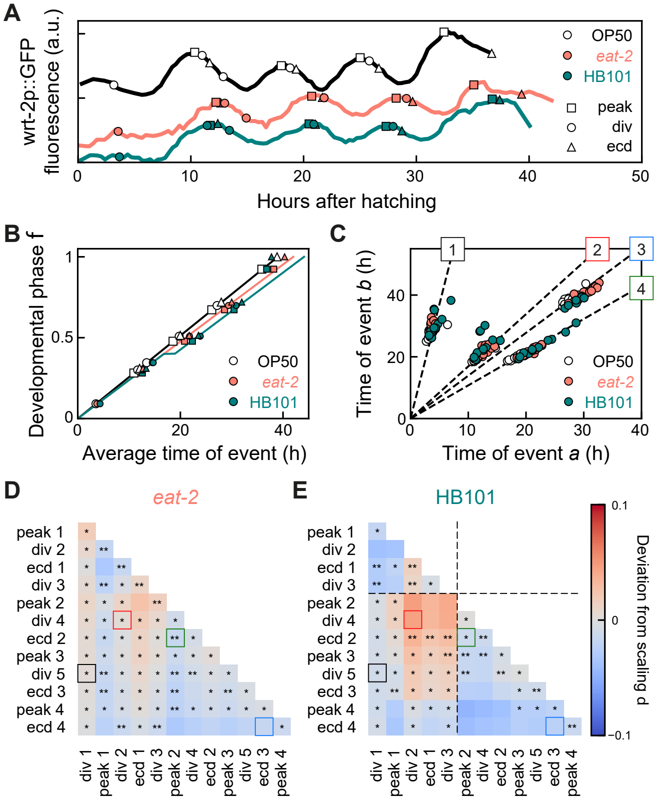

Figure 3.4: Breakdown of temporal scaling for change in diet. (A) Developmental timing in individual animals in standard conditions (black: wild-type, *E. coli* OP50 diet) and two conditions that exhibit slow development: wild-type on *E. coli* HB101 (green) and *eat-2* mutants, that have reduced food uptake, on *E. coli* OP50 (orange). Markers indicate seam cell divisions (circles), *wrt-2p::GFP* peaks (squares) and ecdyses (triangles). **(B)** Developmental phase as function of time. Markers indicate events as in (A). For *eat-2* mutants, the phase evolution is well fitted by the 'Uniform' model (orange line), and for wild-type on HB101 by the 'Pause' model (green line) with a ~ 2 h pause between division 3 and peak 2. **(C)** Measured times for event pairs: (1) division 1 and 5, (2) division 2 and 4, (3) peak 2 and ecdysis 2, and (4) ecdysis 3 and 4. Lines are a fit to data for standard conditions. For (2) and (3), animals on HB101 show systematic deviations from scaling. **(D),(E)** Deviation from scaling for (D) *eat-2* mutants and (E) animals fed HB101. Stars indicate the probability that the data observes the same scaling relation as on standard conditions: *:N.S., **:$P < 0.01$, and $P < 0.001$ otherwise (K-S test). Dashed lines in (E) indicate the time of the pause. While scaling is observed for almost all event pairs in *eat-2* mutants, animals on HB101 exhibit systematic deviations from scaling that match those predicted by the 'Pause' model both in sign and magnitude.

stages, strongly reduced synchrony between individuals in progression through larval stages and frequent developmental arrest, with all these phenotypes increasing in severity as development proceeds [86, 92, 93]. Second, *lin-42* mutants exhibit heterochronic phenotypes in multiple organs [86, 87, 94, 95], indicating a body-wide role for *lin-42*. In addition, *lin-42* is expressed in many cells throughout the body and in a striking oscillatory manner, with LIN-42 protein levels peaking once every larval stage [87]. This, together with the homology of *lin-42* to the circadian clock gene period, has led to the speculation that *lin-42* acts as a global developmental timer [32, 86]. Finally, *lin-42* regulates the expression of many miRNAs, including those involved in timing through the heterochronic pathway and binds to the promoter of many genes [39–41]. Because of this wide-ranging impact on developmental timing and gene expression, *lin-42* appeared a prime candidate also for a core component of a potential scaling mechanism. Hence, we wanted to test whether *lin-42(0)* animals displayed stronger deviations from temporal scaling than observed under changes in diet.

We used the *lin-42(ox461)* allele that deletes the entire *lin-42* locus and shows the strongest perturbation of molting cycle progression [92]. Indeed, we found that postembryonic development at 23 °C was significantly slower in *lin-42(0)* animals, with much stronger variability both in the total duration of development (57 ± 7 h for *lin-42(0)*, compared to 39 ± 2 h for wild-type animals) and the duration of individual larval stages (Fig. S3.3). In addition, *lin-42(0)* animals showed reduced growth, as measured by the increase of body length over time in individual animals (Fig. 3.5A,B). In particular, we observed a fraction of animals that stopped growing completely between the L2 and L4 larval stage, with some reaching body lengths of only 0.3 mm, compared to 0.9 mm for wild-type animals. Surprisingly, all animals that arrested growth appeared to otherwise continue development: they underwent multiple rounds of ecdysis, seam cell divisions and *wrt-2* expression peaks (Fig. 3.5C). Animals frequently skipped the final seam cell division and ecdysis, a heterochronic phenotype observed before, but did so independently of the growth arrest. After molting, *lin-42(0)* animals often remain stuck in their old cuticle, and it was suggested that this interferes with the ability to feed [92]. However, we observed growth arrest also in animals that appear to shed their cuticle normally. Moreover, growth-arrested animals also displayed pharyngeal pumping, suggesting that growth arrest was not simply caused by inability to take up food.

3.2.5. BREAKDOWN OF INTER-INDIVIDUAL AND POPULATION-LEVEL TEMPORAL SCALING IN *lin-42* MUTANTS

When we compared the average timing of each seam cell division, *wrt-2* peak and ecdysis between wild-type and *lin-42(0)* animals at 23 °C (Fig. 3.5D), we found that again development separated into multiple epochs that differed in impact on timing: in the first epoch (hatching to third seam cell division) developmental phase increased at the same rate in *lin-42(0)* and wild-type animals, while in the second epoch (from the second *wrt-2* peak onwards) the phase still increased linearly in *lin-42(0)* mutants but with a strongly decreased rate compared to wild-type animals. When we examined timing in individual animals, we found that variability in timing was

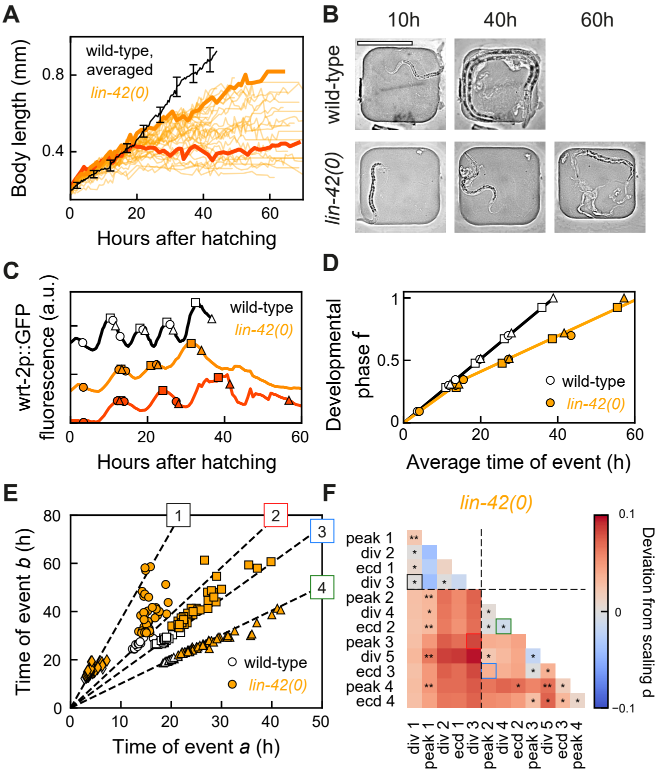

Figure 3.5: Growth arrest and temporal scaling in *lin-42(0)* animals. **(A)** Body length as function of time for standard conditions (black, average for wild-type animals at 23 °C) and *lin-42(0)* animals (orange lines, individual animals). While some *lin-42(0)* animals only exhibited reduced growth, other animals showed complete growth arrest from the mid-L2 stage, ~ 20 h after hatching, capping body length to <0.5 mm. Thick lines highlight one individual with reduced growth (light orange) and one arresting growth (dark orange). Error bars indicate S.E.M. **(B)** Microscopy images of a wild-type (upper panels) and growth-arrested *lin-42(0)* larva (lower panels) at different times after hatching. Scale bar: 200 μm. **(C)** Developmental timing in a wild-type larva (black), and in a slow-growing (light orange) and growth-arrested (dark orange) *lin-42(0)* animal that correspond to the individuals highlighted in (A). Markers indicate seam cell divisions (circles), *wrt-2p::GFP* peaks (squares) and ecdyses (triangles). The growth-arrested animal (dark orange) executed most events that occur after mid-L2, indicating the absence of a developmental arrest. **(D)** Developmental phase as function of time in wild-type (black) and *lin-42(0)* animals (orange). The phase evolution in *lin-42(0)* animals was well fitted with the 'Rate change' model (orange line), occurring at wild-type rate until the mid-L2 stage, and ~2-fold decreased rate for events occurring later. **(E)** Measured times for event pairs: (1) division 1 and 3, (2) division 3 and peak 3, (3) peak 2 and ecdysis 3, and (4) division 4 and ecdysis 2. Lines are a fit to data for standard conditions. Overall, *lin-42(0)* animals show strong variability in timing between individuals, and for event pairs (2) and (3) exhibit clear deviations from scaling. (F) Deviation from scaling for development in *lin-42(0)* mutants. Stars indicate probability that *lin-42(0)* data observes the same scaling relation as wild-type: *:N.S., **:$P < 0.01$, and $P < 0.001$ otherwise (K-S test). Deviations from scaling resemble those predicted by the 'Rate change' model, with dashed lines indicating the measured time of the rate change.

dramatically increased in *lin-42(0)* mutants. Yet, despite this strong variability data points for the majority of event pairs still clustered along a line (Fig. 3.5E, Fig. S3.4). Strikingly, we found that this was not the case for all event pairs: for instance, some animals that were among the first to execute the third seam cell division exhibited an exceptionally late third *wrt-2* peak, resulting in many points away from the line (Fig. 3.5E, event pair 2), indicating a breakdown of inter-individual temporal scaling. The key assumption underlying inter-individual temporal scaling is that the variation in the developmental rate between individuals remains constant throughout larval development. However, in individual *lin-42(0)* animals, the duration of early-larval development was often poorly correlated with the duration of late-larval development, compared to the other genotypes and conditions we examined (Fig. S3.5A-C). Indeed, model simulations showed that this observation was sufficient to explain these deviations from inter-individual scaling (Fig. S3.5D-G).

For event pairs that did cluster along a line, data points often showed systematic deviations from the line predicted by data for standard conditions (wild-type animals at 23 °C) corresponding to a lack of population-level temporal scaling. We used the measured evolution of developmental phase to construct a phenomenological model of timing in *lin-42(0)* mutants ('Rate change' model, Fig. 3.3A, 3.5D). This model reproduced the experimental observation that data for most event pairs clustered along lines, but with systematic deviations from the lines predicted by data for standard conditions (Fig. 3.3B-D). In particular, for the 'Rate change' model these lines always had a larger slope than for standard conditions, i.e. $\delta \geq 0$ (Fig. 3.3F). Indeed, when we calculated δ for all experimentally measured event pairs (Fig. 3.5F) the resulting dependence of δ on the developmental phase strongly resembled the prediction from the 'Rate change' model (Fig. 3.3F): first, the deviation was largest for event pairs with one event occurring prior to the mid-L2 larval stage, when we observed the change in developmental rate, and the other occurring afterwards. Second, in contrast to data for wild-type animals fed HB101, the deviation in *lin-42(0)* mutants was always positive ($\delta > 0$). These results suggested that the breakdown of population-level temporal scaling was largely accounted for by the change in developmental rate at the mid-L2 larval stage that separated the two observed epochs. Finally, compared to the rest of the population, growth-arrested animals did not develop more slowly, and their developmental timing did not exhibit stronger deviations from temporal scaling (Fig. S3.4), suggesting this was largely independent of physical growth.

Overall, *lin-42(0)* mutants exhibited strongly perturbed and variable timing, with larval development separated into two epochs that differed in developmental rate. Surprisingly, given the putative role of *lin-42* as a key regulator of developmental timing, we found that both individual variability and population-level changes in timing were explained by temporal scaling, but only when considering events within the same epoch, i.e. events occurred at the same time when measured relative to the duration of epochs in each individual.

3.3. DISCUSSION

Here, we showed that changes in timing of individual developmental events, under a broad array of conditions that change the total duration of *C. elegans* larval development, are largely explained by temporal scaling, both for variability in timing between individuals and for population-level changes in timing when environmental conditions or genotype are varied.

We found that many of our experimental observations could be reproduced by simple, phenomenological timing models (Fig. 3.3). In these models, the complexity of developmental progression is reduced to the evolution of a developmental phase in time, similar to the use of phase in the analysis of nonlinear oscillators. Animal-to-animal variability arises because each animal proceeds through its phase evolution at an intrinsically different rate, giving rise to the strongly correlated variability we measured for timing of event pairs. When we compared event times between animals of different genotype or raised under different conditions, the resulting changes in timing were not simply explained by the population-level change in total duration of larval development. We found that these deviations from scaling were explained by the subdivision of larval development in distinct epochs, that differ in how the evolution of phase is impacted upon changes in genotype or environmental condition. This result implies that event timing did exhibit temporal scaling, but only when taking into account these epochs: events occur at the same time, independent of genotypes or conditions, when measured relative to the duration of each epoch rather than the total duration of development. While these phenomenological models do not provide a molecular mechanism for temporal scaling, they reveal a remarkably simple organization that unifies the broad variations in timing seen in our experiments.

It is striking that isogenic animals under identical environmental conditions displayed strong variability in developmental timing. This variability was strongly correlated between event pairs, for almost all event pairs, conditions and genotypes examined (Fig. 3.1G, 3.2C, 3.4C, 3.5E). This implies that each individual progresses through development at a constant rate, which however varies from animal to animal, with this variability in overall developmental rate explaining the observed variability in timing. What controls this variation in developmental rate? A recent study found that animal-to-animal variability in timing of the L4 ecdysis, i.e. the transition into adulthood, correlated with age of the mother at fertilization [96], with embryos generated by older mothers developing more rapidly. This was linked to the amount of yolk proteins loaded in each embryo, which increased with the mother's age, suggesting that the rate of larval development is determined by the status of nutrient stores in the embryo. It is surprising, however, that this variation in rate persists throughout development, particularly as larvae depend for growth on feeding rather than internal stores. The only case we observed where the rate of early-larval development was not predictive of the late-larval rate is *lin-42(0)* mutants (Fig. S3.5). This might reflect a role of *lin-42* in maintaining the developmental rate at the embryo-set level, but could also reflect that the severity of the *lin-42(0)* phenotype, as it emerges during larval development, is independent of the early-larval developmental rate.

For some changes in genotype or conditions (changes in temperature, *eat-2* feeding mutants), the rate of development was reduced by a constant factor for all larval development (Figs. 3.2B, 3.4B). In contrast, both for wild-type animals fed HB101 and *lin-42(0)* mutants, we observed a discontinuity in the rate of development that separated larval development into two epochs (Figs. 3.4B, 3.5D). Interestingly, even though the nature of the discontinuity differed, with a pause for animals fed HB101 and a change in rate for *lin-42(0)* mutants, both occurred at the same development stage: the mid-L2 larval stage, between third seam cell division and second *wrt-2* peak. This stage is notable, as it forms an important transition both in terms of development and metabolism. First, under conditions of crowding or food deprivation larvae enter dauer, an alternative developmental state that is highly stress-resistant, and commit to this fate before the mid-L2 larval stage [97, 98]. Interestingly, *lin-42* is involved in dauer commitment, with *lin-42* mutants showing increased dauer formation at 27 °C [99]. Hence, the change in developmental rate at this stage might reflect involvement of the dauer decision-making machinery. However, we prefer another explanation: *C. elegans* larvae also shift their metabolism between the L1 and L2 larval stage, from the glyoxylate cycle to the TCA cycle [100]. The glyoxylate cycle likely allows L1 larvae to use stored lipids as an energy source, potentially rendering their development less dependent on ingestion of food. As a consequence, shifts in diet (from *E. coli* OP50 to HB1010) or inability to ingest or metabolize food in *lin-42(0)* mutants might only impact developmental timing substantially after shifting to the TCA cycle upon entering the L2 larval stage.

Our observations raise the question how temporal scaling is regulated. One attractive mechanism to regulate timing in a manner that is synchronized throughout the body and adapts to changes in rate of development under different conditions, is to couple developmental timing to physical growth. If timing was regulated in such a way that each event occurred at a specific body size, it would explain temporal scaling, as changes in conditions that impact the body's growth rate would naturally lead to concomitant changes in developmental timing. Analogously, cell cycle timing in bacteria and yeast strongly depends on cell size and growth [101–104]. Indeed, progression of *C. elegans* larval development is tightly linked to body size [69], and under dietary conditions that caused slow growth, larval stages lengthened so that molts occurred at their stereotypical body size [43]. Moreover, conditions that do not allow growth, such as starvation, typically lead to developmental arrest at the start of each larval stage [12, 45, 54]. It is therefore an important observation that *lin-42(0)* mutants continued development without physical growth (Fig. 3.4), and with timing of development obeying temporal scaling within each epoch (Fig. 3.5). Continued development after growth arrest in *lin-42(0)* mutants was shown recently for motor neuron, gonad and vulva development [92], but timing was not examined. Our work now extends these observations, indicating that continued development without growth is likely a *lin-42(0)* phenotype with body-wide impact, and specifically invalidates a mechanism where temporal scaling results from coupling developmental timing to physical growth.

Two distinct classes of molecular mechanisms to explain temporal scaling could be envisioned. In the first class, feedback mechanisms or checkpoints actively adjust timing. An example of this class are the size-based checkpoints proposed for single-celled organisms, but invalidated by us as a mechanism for *C. elegans*. A more general example are the feedback mechanisms that actively shape morphogen gradients that underlie spatial scaling in developmental pattern formation. The second class of mechanisms emerged from recent studies examining the dependence of developmental timing in *C. elegans*, fly and frog embryos on temperature [105–108]. They explain temporal scaling as emerging from careful tuning of the molecular processes in the cell. Specifically, Kurtz and Eisen found that timing of fruit fly development scaled uniformly with temperature [107], similar to our observations for *C. elegans* larval development (Fig. 3.2). Intriguingly, in these studies the measured dependence of timing on temperature followed an Arrhenius equation [105–107], which is historically used to describe the temperature dependence of chemical reactions. Temporal scaling arises only if timing of all events follows the same Arrhenius equation, i.e. timing of all events varies by the same factor for a given change in temperature. Because the rates of molecular processes are likely not only controlled by temperature but also by metabolite levels, such thermodynamic mechanisms might also generate temporal scaling upon changes in diet or food uptake, as we observed (Fig. 3.4, 3.5). However, more recent measurements disputed the key assumption that all processes follow the same Arrhenius equation [105, 106], raising the question whether thermodynamic mechanisms by themselves are sufficient to explain temporal scaling, or if additional active feedback or checkpoint mechanisms are still essential.

One of the most enduring mysteries of development is how its timing is regulated. Whereas we have a deep understanding of how spatial patterns arise during development [80], our understanding of how events like cell division, cell movement or gene expression are controlled in time is still very limited. Post-embryonic development poses a particular challenge, as its rate of progression depends strongly on environmental conditions such as food availability. How timing is adapted on the cellular level in response to such organism-level changes is an open question. On the molecular level, developmental timing is thought to be controlled either by oscillators or ‘hourglass’ mechanisms. In *C. elegans*, even though there is now evidence both for hourglass mechanisms [84, 85] and oscillators [32, 35] in regulating timing of larval development, we still do not understand how the exact time at which cell-level events are initiated is determined on the molecular level. Both hourglass and oscillator mechanisms do not exhibit temporal scaling of their decay time or period, respectively, without alterations to their basic mechanism. Hence, our observation of temporal scaling will put strong constraints on possible models that explain developmental timing of *C. elegans* larval development.

We thank Sander van den Heuvel for providing the *wrt-2p::GFP* strain and Ann Rougvie for providing the *lin-42* alleles.

3.4. METHODS

3.4.1. STRAINS AND EXPERIMENTAL CONDITIONS

The following strains were used: *heIs63[Pwrt-2::GFP::PH; Pwrt-2::GFP::H2B; Plin-48:: mCherry]* [74], *eat-2(ad1113)* [91], *lin-42(ox461)* [92]. To monitor *wrt-2::GFP* expression in *eat-2* and *lin-42* mutants, these mutations were crossed into *heIs63*. The *eat-2* genotype was confirmed by measuring the rate of pharyngeal pumping, which is decreased 5-fold compared to wild-type animals [91]. As *lin-42* constitutes a complex genetic locus encoding multiple isoforms, we chose to use the *lin-42(ox461)* allele that deletes the entire locus of *lin-42* [92]. In addition, the *lin-42(ok2385)* allele that deletes the main isoform *lin-42a* and the overlapping exons of *lin-42b*, was analyzed and showed similar phenotypes as *lin-42(ox461)* (data not shown). For maintenance, all strains were cultured at 20 °C on NGM (Nematode growth medium) agar plates seeded with OP50 strain of *E. coli* bacteria, using standard *C. elegans* techniques. For time-lapse experiments, we refer to standard conditions as *wrt2p::GFP* animals fed *E. coli* OP50 at 23 °C. For experiments in perturbed conditions we varied one experimental parameter (*C. elegans* strain, temperature or diet) while keeping the others unchanged. For the diet experiment in Fig. 3.4, *E. coli* HB101 was used instead. In that case, animals were maintained on HB101 for 5-7 generations prior to the experiment.

3.4.2. TIME-LAPSE MICROSCOPY

Custom time-lapse microscopy setup was used to monitor the entire development of individual *C. elegans*. Late-stage embryos were placed inside the $250 \times 250 \times 20\ \mu$m polyacrylamide microchambers (one embryo per chamber) filled with *E. coli* bacteria as food source. Nikon Ti-E inverted microscope with a large chip camera (Hamamatsu sCMOS Orca v2) and a 40X magnification objective (Nikon CFI Plan Fluor 40X, NA=1.3, oil immersion) were used for imaging. Transmission and fluorescence images were acquired with an LED light source (CoolLED pE-100 615 nm) and a 488 nm laser (Coherent OBIS LS 488-100), respectively. Each chamber containing a single animal was imaged every 20-40 minutes during the entire larval development (40-100 hours depending on the genotype and temperature). A stack of 20-30 images in the Z-direction was acquired using short exposure times (1-10 ms), such that the motion of the animal was insignificant. We have previously demonstrated that this technique does not hinder larval growth and development [48].

3.4.3. TEMPERATURE CONTROL

All experiments were performed in a temperature-controlled room with a constant temperature inside the sample of 23 °C. To perform an experiment at different temperature, an additional temperature control system was used. A thermoelectric chiller (Thermotek T257P) was used to cool the custom made objective jacket by circulating an antifreeze fluid (a mixture of water and glycerin) between the chiller and the objective jacket. In order to calibrate the system, a thermocouple temperature sensor measuring 0.025 mm in diameter (RS Pro) was placed inside the sample in contact with the polyacrylamide hydrogel and connected to a digital thermometer (RS Pro). The temperature was then varied on the thermoelectric chiller while the resulting temperature inside the sample was being monitored. In this work, experiments were performed at 23, 19 or 15 °C.

3.4.4. IMAGE ANALYSIS

Time-lapse image stacks were processed with custom Python software in order to obtain the precise timing of ecdysis events, seam cell divisions, and peaks in oscillatory *wrt-2* expression. For every animal, the times of hatching and ecdysis events were annotated based on visual inspection of transmitted light images. Hatching was defined as the time larvae first appears out of the egg shell, while ecdysis events were defined as the first appearance of the shed cuticle in the chamber (Fig. 3.1C). Times of seam cell divisions were annotated based on visual inspection of the *wrt-2p::GFP* fluorescence signal in the nucleus and the membrane of seam cells. Divisions of V1-V6 seam cells occur close together in time. We therefore defined the time of each round of divisions as the average time V1-V6 cells had divided or had started dividing, as determined by the formation of the metaphase plate. We only analyzed seam cells located on the side of the body closest to the objective. To determine the time of peaks in oscillatory *wrt-2* expression, we first obtained *wrt-2* expression profiles as a function of time for individual animals. For this, in every time frame we automatically segmented the region encompassing seam cells using a Watershed algorithm and calculated the average fluorescence intensity inside this region. Finally, to find the time of each peak (μ_i), we fitted the obtained oscillatory profiles with a combination of Gaussian functions and a linear offset using non-linear least-squares minimization (Fig. 3.1B):

$$f(x,m,b,A_i,\mu_i,\sigma_i) = mx + b + \sum_{i=1}^{n}\left[\frac{A_i}{\sigma_i\sqrt{2\pi}}e^{\left[-\frac{(x-\mu_i)^2}{2\sigma_i^2}\right]}\right] \tag{3.1}$$

where n is the number of peaks, A_i, μ_i and σ are the amplitude, center and width of peak. Finally, we fitted the experimentally measured times for pairs of events a and b to a line function of the form $t_b = s_{a,b} \cdot t_a$ using non-linear least-squares minimization (Fig. 3.1G), using the Linear Model from the lmfit package in Python. To measure the animal's body length as a function of time (Fig. 3.5A), we manually annotated ~10 points along the anterior-posterior body axis and performed spline interpolation. Body length was defined as the length of the resulting spline curve.

3.4.5. TIMING MODELS AND SIMULATIONS

We model the progression of development as the evolution of a developmental phase ϕ, that increases from $\phi = 0$ (start of larval development at hatching) to $\phi = 1$ (entry into adulthood at the L4 ecdysis). The exact assignment of a phase to a particular developmental event is arbitrary. Here, we define the phase so that for standard conditions (wild-type animals at 23 °C) the phase increases linearly with time, $\frac{d\phi}{dt}$ =const, and $\phi = 1$ at time $t = T$, where T is the total duration of development at standard conditions. As a result, for standard conditions we use the following definition for the developmental phase of event a:

$$\phi_a = \frac{t_a}{T} \tag{3.2}$$

For other conditions or genotypes, the time evolution $\phi(t)$ of the developmental phase has a different form. As a result, the time of event a, occurring at a developmental phase ϕ_a is given by $t_a = f(\phi_a)$, where f is a monotonically increasing function that is specific for each condition or genotype. Expressions for $f(\phi)$ are discussed further below. To incorporate animal-to-animal variability, we assumed two different sources of variability. First, there is an intrinsic variability in the stage ϕ_a at which each event occurs, that is uncorrelated between different events occurring within the same animal. Second, we assumed variability in the total duration of development, T. This corresponds to an animal-to-animal variability in the global rate of development that impacts each event occurring within the same animal equally. Then, the event time $t_{a,i}$ for event a in animal i is given by:

$$t_{a,i} = \frac{f(\phi_a + \eta_{\phi,i})}{T}\left(T + \eta_{T,i}\right) \tag{3.3}$$

where T and ϕ_a correspond to the population average values, while η_T and η_ϕ are Gaussian noise sources with standard deviation σ_T and σ_ϕ, respectively. The function $f(\phi)$ changes for differing environmental conditions or mutants that perturb the duration of development. In particular, we considered three different models, the 'Uniform', 'Pause', and 'Rate change' models (Fig. 3.3A). For the 'Uniform' model, event times are given by Eq. 3.2, but now with an increased duration of development T'. For the 'Pause' model, developmental occurs at the same rate as for standard conditions, but with a pause at developmental phase ϕ' that results in a total duration of development $T' = (1+\kappa)T$, resulting in:

$$t_a = \begin{cases} T\phi_a & \phi_a < \phi' \\ T(\kappa + \phi_a) & \phi_a \geq \phi' \end{cases} \tag{3.4}$$

Finally, for the 'Rate change' the developmental rate differs between events occurring prior to a developmental phase ϕ and events occurring afterwards, resulting in:

$$t_a = \begin{cases} T_1\phi_a & \phi_a < \phi'' \\ (T_1 - T_2)\phi'' + T_2\phi_a & \phi_a \geq \phi'' \end{cases} \tag{3.5}$$

where $1/T_1$ and $1/T_2$ correspond to the two developmental rates and the total duration of development is given by $T' = T_1\phi'' + T_2(1-\phi'')$.

3.4.6. CALCULATION OF DEVIATION FROM SCALING FOR TIMING MODELS

For the 'Uniform', 'Pause' and 'Rate change' model, we calculate the deviation from scaling as follows. First, we use that fact that for events a and b that occur in the same animal, the total duration of development, T' , has the same value, to express t_b as function of t_a. For the 'Uniform' model, this yields:

$$t_b = \frac{\phi_b}{\phi_a} t_a \tag{3.6}$$

meaning that that event pairs lie along the same line as measured for individuals under standard conditions, and that the changes in timing can be fully captured by a simple rescaling of event times with the duration of development T' under non-standard conditions. In contrast, for the 'Pause' model, this yields:

$$t_b = \begin{cases} \frac{\phi_b}{\phi_a} t_a & t_a, t_b < t^* \\ \frac{\kappa+\phi_b}{\phi_a} t_a & t_a < t^*, t_b > t^* \\ \frac{\kappa+\phi_b}{\kappa+\phi_a} t_a & t_a, t_b > t^* \end{cases} \tag{3.7}$$

Here, pairs of time points for events a and b only lie along the same line as those for standard conditions when both events occur before the time of the delay, $t^* = T\phi'$. Otherwise, the slope of the line is different from wild-type conditions and depends explicitly on the delay parameter κ. Finally, for 'Rate change' model, corresponding to the *lin-42(ox461)* mutant, we have:

$$t_b = \begin{cases} \frac{\phi_b}{\phi_a} t_a & t_a, t_b < t^* \\ \left(\frac{\phi''}{\phi_a} + \frac{T_2}{T_1}\frac{\phi_b-\phi''}{\phi_a}\right) t_a & t_a < t^*, t_b > t^* \\ \frac{T_1\phi''+T_2(\phi_b-\phi'')}{T_1\phi''+T_2(\phi_a-\phi'')} t_a & t_a, t_b > t^* \end{cases} \tag{3.8}$$

where $t^* = T_1\phi''$. Apart from the case when $t_a, t_b < t^*$, this expression depends explicitly on the parameters ϕ'' and T_2 and does not lie along the same line as event pairs for standard conditions. Finally, we calculate the deviation from scaling as:

$$\delta_{ab} = \arctan\left(s_{ab}^S\right) - \arctan\left(s_{ab}^P\right) \tag{3.9}$$

where $t_b = s_{ab} \cdot t_a$, with the slope s_{ab} given by Eqs. 3.7-3.9, and S and P denote standard and perturbed conditions, respectively.

3.4.7. MODEL PARAMETERS

For the model results in Fig. 3.3A-D, we used the following parameters, chosen to emphasize and clarify the differences between models. For the 'Standard condition' model: $T = 30$ h. For the 'Uniform' model: $T' = 60$ h. For the 'Pause' model: $\kappa = 1$ and $\phi' = 0.4$, resulting in a total duration of development of $T' = 60$ h. For the 'Rate Change' model: $T_1 = 25$ h, $T_2 = 95$ h and $\phi'' = 0.5$, also resulting in $T' = 60$ h. For the stochastic simulations in Fig. 3.3C-D: $\sigma_T = 5$ h and $\sigma_\phi = 7 \cdot 10^{-3}$. For Figs. 3.2, 3.3E,F, 3.4 and 3.5, we used model parameters that were fitted to the experimental data. In Fig. 3.2, we used the following fitted parameter values: $T^{23°C} = 39$ h, $T^{19°C} = 57$ h, and $T^{15°C} = 110$ h. In Fig. 3.4 and Fig. 3.3E, we used the following fitted parameter values: $T^{eat-1} = 42$ h, $T^{HB101} = 42$ h, $\kappa_{HB101} = 5 \cdot 10^{-2}$ and $\phi'_{HB101} = 0.4$. In Fig. 3.5 and Fig. 3.3F, we used the following fitted parameters: $T_1^{lin-42} = 45$ h, $T_2^{lin-42} = 70$

h and $\phi''_{lin-42} = 0.35$. The parameters for HB101 and *lin-42* were used to make the quantitative predictions in Fig. 3.3E,F using Eqs. 3.7 and 3.8.

3.4.8. CALCULATING THE DEVIATION FROM SCALING FOR EXPERIMENTAL DATA

We used the following procedure to assess whether the timing of event pairs a and b under perturbed conditions P deviate from the scaling relationship found for their timing under standard conditions S. For each animal i with measured event timing $t_{a,i}$ and $t_{b,i}$, we calculate $\theta_i = \arctan \frac{t_{a,i}}{t_{b,i}}$. First, we calculate the average deviation δ from scaling as $\delta = \langle\theta_i^P\rangle - \langle\theta_i^S\rangle$. However, in particular for event pairs with small average event times $\langle t_{a,i}\rangle$ and $\langle t_{b,i}\rangle$, values of θ_i can vary substantially, leading to non-zero deviation δ for the typical number of animals analyzed for these experiments. Hence, we also estimate the probability that the two series θ_i^P and θ_i^S are sampled from the same distribution, using the two-sample Kolmogorov-Smirnov test (ks_2samp from the scipy.stats package in Python). We reported the P value, with high P meaning that the distributions of the two samples are likely the same, and, hence, obey the same temporal scaling relationship.

3.5. SUPPLEMENTARY FIGURES

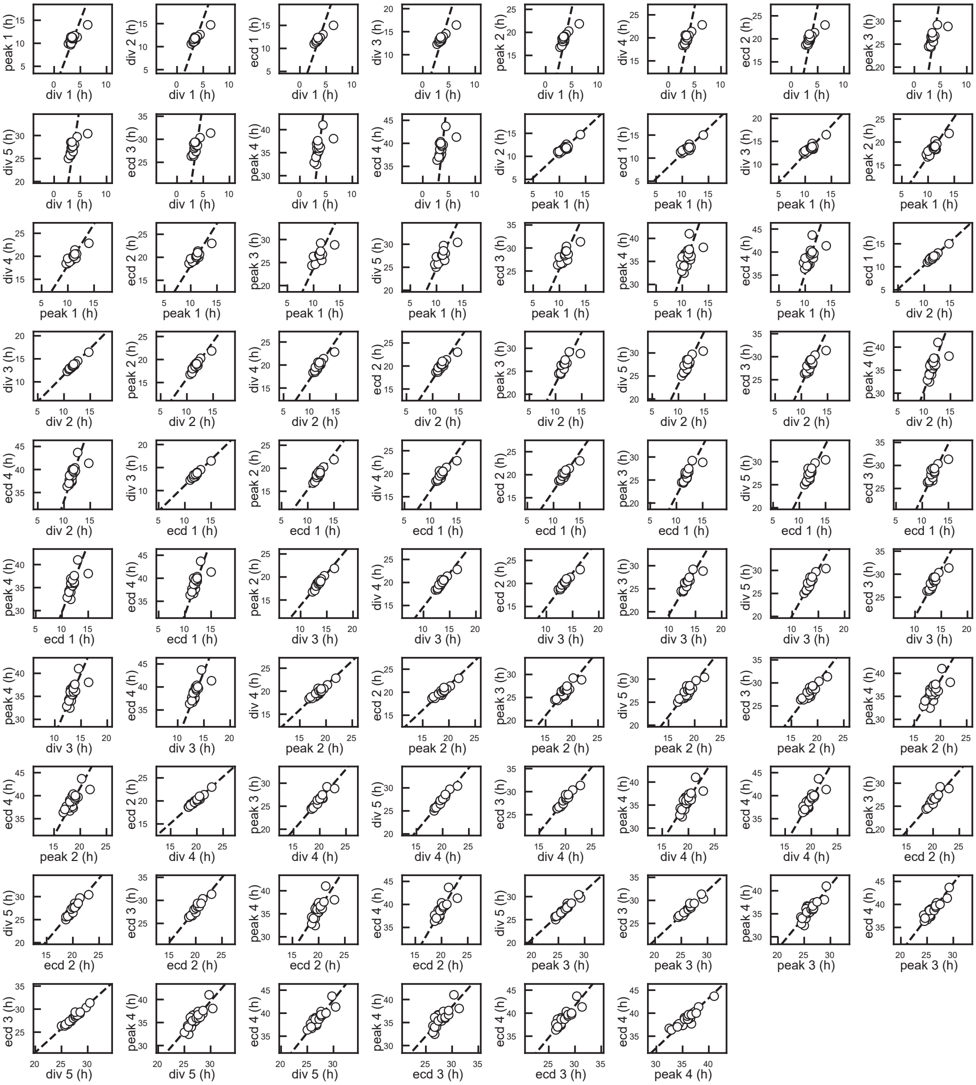

Figure S3.1: Temporal scaling in animal-to-animal variability of timing. Measured times for all measured event pairs a, b in wild-type animals, on an *E. coli* OP50 diet at 23 °C. Markers correspond to times measured in a single animal. Dashed lines are fits of the form $t_b = s_{a,b} \cdot t_a$.

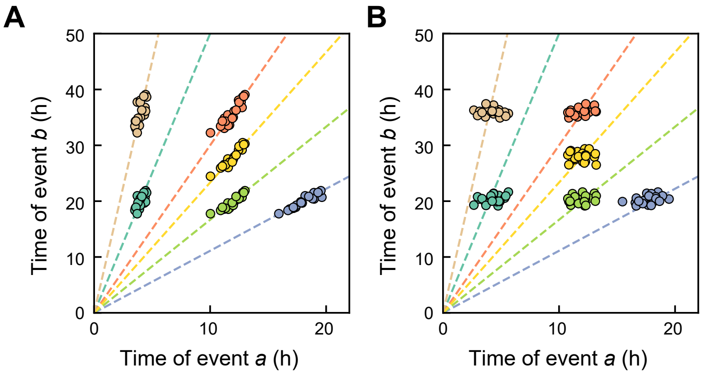

Figure S3.2: Stochastic timing model. **(A)** Simulated times of event pairs a, b in the stochastic timing model (Eqs. 3.2 and 3.3 in Methods). Simulation parameters were chosen to resemble the experimental data in Fig. 3.1E. Times were generated for six events that occur at developmental phases ϕ=0.1, 0.3, 0.45, 0.5, 0.7 and 0.9, that are chosen so that the plotted event pairs occur at similar times as those in Fig. 3.1G. The average duration of development was $T = 40$ h. For the noise sources, we used standard deviations $\sigma_T = 3$ h and $\sigma_\phi = 7 \cdot 10^{-3}$, meaning that common variability in the rate of development, $1/T$, is stronger than variability in timing of each individual event. The simulated data closely resembles the experimental data in Fig. 3.1G, with times for event pairs a, b scattered along lines of $t_b = \frac{\phi_b}{\phi_a} t_a$ (dashed lines). **(B)** Same simulation as in (A), but now with standard deviations $\sigma_T = 0.1$ h and $\sigma_\phi = 2 \cdot 10^{-2}$, meaning that variability in the timing of individual events is stronger than that in the global rate of development. As a consequence, times for event pairs no longer cluster along lines of $t_b = \frac{\phi_b}{\phi_a} t_a$ (dashed lines)

Genotype	Temperature	Diet
wild-type	15 °C	OP50
wild-type	19 °C	OP50
wild-type	23 °C	OP50
wild-type	23 °C	HB101
eat-2(ad1113)	23 °C	OP50
lin-42(ok2385)	23 °C	OP50

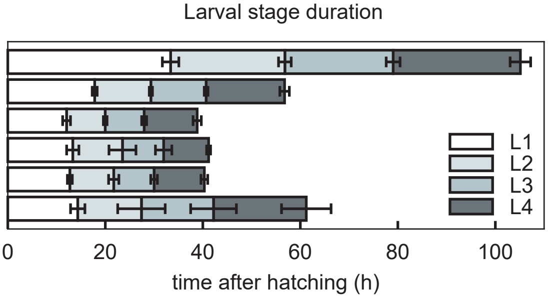

Figure S3.3: Overview of genotypes, conditions and duration of larval stages. Average duration of larval stages L1-L4 for the different genotypes and environmental conditions used. Wild-type refers to animals carrying only the *wrt-2p::GFP* reporter, which exhibit timing of larval stages similar to animals without this reporter. Strains with genotype different than wild-type also carry the *wrt-2p::GFP* reporter. OP50 and HB101 refer to different *E. coli* bacterial strains used as food source. The standard condition used as benchmark to compare event timing against is outlined in grey. For larval stage duration, error bars indicate S.D. and for each condition $n > 7$, except for *lin-42(0)* mutants, where only a few animals complete the L4 stage ($n = 4$).

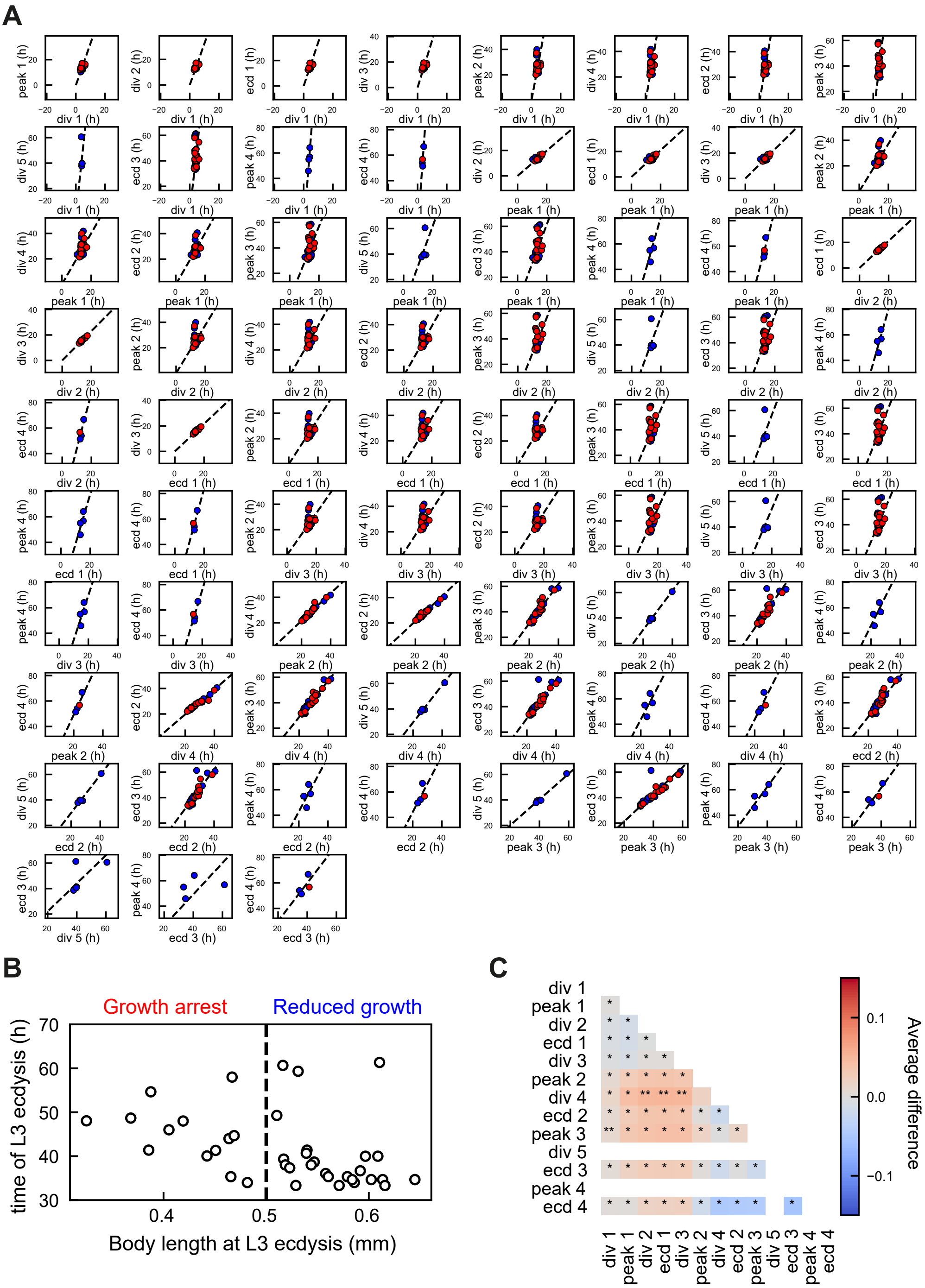
A
div 1 (h)
peak 1 (h)
div 2 (h)
ecd 1 (h)
div 3 (h)
peak 2 (h)
div 4 (h)
ecd 2 (h)
peak 3 (h)
div 5 (h)
ecd 3 (h)
peak 4 (h)
ecd 4 (h)
B
Growth arrest
Reduced growth
time of L3 ecdysis (h)
70
60
50
40
30
0.4
0.5
0.6
Body length at L3 ecdysis (mm)
C
div 1
peak 1
div 2
ecd 1
div 3
peak 2
div 4
ecd 2
peak 3
div 5
ecd 3
peak 4
ecd 4
0.1
0.0
−0.1
Average difference

Figure S3.4 *(previous page)*: Dependence of deviation from temporal scaling on lin-42(0) growth arrest phenotype. (A) Measured times for all event pairs measured in at least $n \geq 4$ animals. Some event pairs found during wild-type L4 larval stage development do not appear as they are executed only rarely in *lin-42(0)* animals. Lines are a linear fit to the data points. Markers are colored according to growth phenotype, as defined in panel (B). The deviation from scaling does not differ strongly between growth-arrested animals (red) and animals with reduced growth (blue). **(B)** Length at L3 ecdysis compared to time of L3 ecdysis in *lin-42(0)* animals. Based on this, we separated the population in growth-arrested animals (length <0.5 mm at L3 ecdysis) and animals with reduced growth (as compared to wild-type animals). Growth-arrested animals developed more slowly than animals with reduced growth, but a small number of animals with reduced growth also displayed very slow development (L3 ecdysis later than 50 h after hatching). We scored the growth phenotype based on L3 characteristics, because most animals skip the L4 larval stage. **(C)** Difference in scaling between growth-arrested (GA) and reduce-growth (RG) animals. Color indicates the difference $\langle\theta^{GA}\rangle\langle\theta^{RG}\rangle$ between the two populations, where, for each event pair a and b measured in an individual animal, the angle $\theta = \arctan \frac{t_a}{} t_b$. Stars indicate the probability that the distribution of θ is the same for growth-arrested and reduced-growth animals: *:N.S., **:$P < 0.01$, and $P < 0.001$ otherwise (K-S test). Overall, no significant differences in scaling were observed between growth-arrested and reduced-growth animals, indicating that growth-arrested animals do not display stronger breakdown of scaling. Empty squares reflect event pairs for which at least one of the two events did not occur in either growth-arrested or reduced-growth animals.

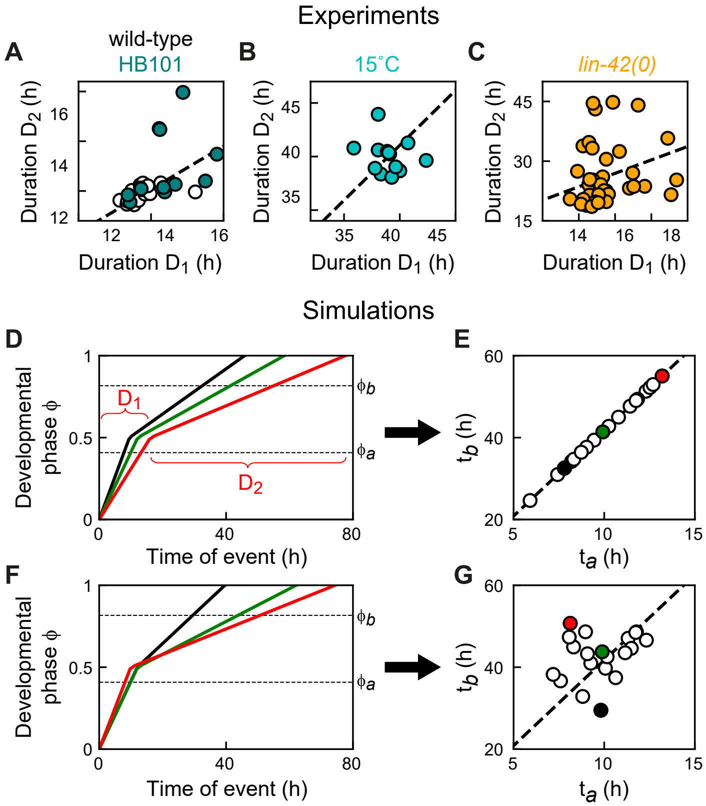

Figure S3.5: Breakdown of inter-individual scaling. (A),(B),(C) Experimentally measured correlation between the developmental duration D_1 and D_2 of development before and after the change in developmental rate, for development under standard conditions (A, wild-type at 23°C), animals fed HB101 (A), at 15°C (B) and in *lin-42(0)* mutants (C). The duration D_1 is defined at the time from hatching to the third seam cell division, while D_2 is given by the time from the third seam cell division to the third ecdysis. For D_2, we do not include the time from the third to fourth ecdysis, as this last part of larval development is often skipped in *lin-42* mutants. The correlation between D_1 and D_2 is much weaker in *lin-42* mutants. **(D),(E)** Inter-individual variability in the 'Rate change' model. In this model, all individuals go through the same evolution of developmental phase ϕ but at a rate that differs between individuals (D). Hence, variability in the duration D_1 and D_2 of development before and after the change in developmental rate is strongly correlated within the same individual. As a consequence, times of events t_a and t_b, occurring at phase ϕ_a and ϕ_b, are clustered tightly along a line, indicating temporal scaling (E). The colored markers in (E) correspond to the individuals whose phase evolution is shown in (D). Model is given by Eqs. 3.3 and 3.5 in Methods, with $T_1 = 25$ h, $T_2 = 95$ h, $\phi'' = 0.5$, $\sigma_\phi = 7 \cdot 10^{-3}$ and $\sigma_T = 15$ h. Dashed line is Eq. 3.8. **(F),(G)** Breakdown of inter-individual scaling, when variability in durations D_1 and D_2 is not correlated within the same individual. As a result, individual animals show strong deviations from temporal scaling. Model is given by Eqs. 3.3 and 3.5, but T_1 and T_2 vary independently within the same individual, with $\sigma_{T_1} = 3$ h and $\sigma_{T_2} = 15$ h. This model result indicates that the lack of correlation between durations D_1 and D_2 observed in *lin-42(0)* mutants can explain the lack of inter-individual scaling seen in *lin-42(0)* mutants when comparing timing of events occurring before and after the change in developmental rate in Fig. 3.5E.

4

STRESS DISCRIMINATION BY BODY-WIDE, STOCHASTIC DAF-16/FOXO NUCLEAR TRANSLOCATION PULSES

Living organisms employ diverse strategies in order to cope with external stresses that compromise their survival. In C. elegans, the insulin/insulin-like growth factor-1 (IIS) pathway induces the expression of protective genes in response to a broad range of stresses, primarily mediated by the transcription factor DAF-16/FOXO. According to the current paradigm, DAF-16 translocates from the cytoplasm to the nucleus upon stress to induce gene expression, and rapidly exits the nucleus upon return to favorable conditions. In this picture, the amount of nuclear DAF-16 is thought to be proportional to the level of stress. Yet, how gene expression regulated by the IIS pathway can be tailored to different types of stress is challenging to explain in the current model. Here we used time-lapse microscopy to follow DAF-16 localization dynamics in individual C. elegans larvae subject to different stress types and magnitudes. Surprisingly, in contrast to the current model, we observed stochastic pulses of nuclear translocation, with DAF-16 shuttling between the nucleus and the cytoplasm under a constant level of stress. These pulses exhibited striking synchronization between intestinal cells, suggesting the presence of long-range communication. For all the stresses studied – starvation, osmotic and heat stress – the fraction of time that DAF-16 remained in the nucleus increased with the stress magnitude, and each stress type was associated with clearly distinguishable DAF-16 pulse dynamics, suggesting that it might encode both the magnitude and the type of stress. Finally, we also observed pulsatile dynamics of the DAF-16 homolog FOXO3a in mammalian cells at low nutrient levels that activate insulin signaling. Overall, our findings suggest that DAF-16/FOXO translocation pulses are a general feature of insulin signaling that might be crucial for its ability to differentiate between and mount the correct response to many different types of stress.

4.1. INTRODUCTION

Living organisms often encounter environmental conditions that are unfavorable for growth and reproduction. Lack of nutrients, extreme temperatures, hypertonic stress, UV radiation and other stresses require appropriate cellular responses to ensure the survival of an individual organism and the entire species. Stress response requires the activation of dedicated signalling pathways which lead, among other modifications, to changes in the expression of a variety of genes that help an organism maintain cellular integrity and proteostasis [109, 110].

An important example of such a signaling pathway is the insulin/insulin-like growth factor-1 signalling (IIS) pathway (Fig. 4.1A). IIS is a fundamental pathway widely conserved across animals species, from ascidians to humans [111]. In *C. elegans*, IIS regulates resistance to starvation, heat stress, osmotic stress [112] and pathogens [113], among other stresses [47]. In addition to stress response, it is involved in longevity, metabolism and development [47]. How this remarkable versatility is accomplished remains an interesting open question. At the heart of the pathway lies the transmembrane insulin receptor DAF-2, which transmits information on nutrient availability and other environmental conditions into the cell [114]. Under conditions of optimal growth, DAF-2 is activated by the binding of insulin-like peptides (ILPs), which are produced and secreted in multiple tissues, predominantly in the head neurons and the intestine [115–117]. Once activated, DAF-2 initiates a cascade of phosphorylation events, eventually leading to phosphorylation of AKT-1 and AKT-2, two homologs of AKT serine-threonine kinase, which in turn phosphorylate DAF-16, a homolog of the forkhead box-O (FOXO) transcription factor and the primary output of the IIS pathway [118–120]. DAF-16 phosphorylation results in its association with 14-3-3 proteins in the cytoplasm, which mask the nuclear localization signal on DAF-16, leading to cytoplasmic sequestration and inactivation [121]. A broad range of external stresses, such as starvation, oxidative and heat stress, downregulates insulin signalling, causing DAF-16 to translocate to the nucleus [120, 122], where it activates the expression of the stress response genes by binding to the specific sequence on their promoters called the DAF-16 binding element (DBE) [123]. Interestingly, it has been shown that different sets of genes are expressed upon different stresses, e.g. starvation and osmotic stress [124].

This versatility is particularly striking within the current paradigm of DAF-16 activity, which assumes deterministic subcellular localization of DAF-16 depending on the presence or absence of stress. Thus, DAF-16 is localized in the cytoplasm under normal physiological and environmental conditions, translocates to the nucleus upon stress, and rapidly shuttles back to the cytoplasm when the animal is relieved from the stress [122]. How DAF-16 can induce differential gene expression within such deterministic model is an interesting and important open question.

It is known that additional inputs regulate DAF-16 activity in parallel to IIS, such as host-cell factor homolog HCF-1 [125] and beta-catenin BAR-1, a member of Wnt signaling pathway [126]. Potentially, the combined inputs from the IIS and other DAF-16 regulators might transmit information on stress type. However, this still raises the question how this information is converted into stress-specific gene expression by DAF-16. A possible solution is that DAF-16 activates gene expression in combination with other transcription factors. Indeed, it was shown that genes controlled by DAF-16 contain an additional binding site, termed DAF-16 associated element (DAE), that is bound by the zinc finger transcription factor PQM-1 to co-regulate gene expression together with DAF-16 [127]. Moreover, five isoforms of DAF-16 have been identified, which have overlapping yet non-redundant functions and could thus encode more information about the stress [128]. At the same time, there are indications that the regulation of DAF-16 localization might be more complex than currently envisioned. In particular, studies of DAF-16 subcellular localization at the population level typically report the fraction of animals with nuclear or cytoplasmic DAF-16 [129]. Even at high levels of stress, DAF-16 is found localized to the cytoplasm in some animals, but the origin of such heterogeneity is unclear. One possibility is that stress response is indeed deterministic, but only a fraction of animals exhibits it. Alternatively, the stress response in individual animals might be more dynamic than currently thought.

Here, we used time-lapse microscopy to follow the subcellular localization dynamics of DAF-16 in single *C. elegans* animals. In contrast to the current paradigm, we show that DAF-16/FOXO transcription factor undergoes pulsatile dynamics under a constant level of environmental stress, repeatedly translocating between the nucleus and the cytoplasm. Surprisingly, even though individual pulses are highly stochastic, they display remarkable synchrony between different cells in the body. Moreover, we show that different types and magnitudes of stress give rise to clearly distinguishable patterns of DAF-16 translocation dynamics. Overall, our results indicate that pulsatile DAF-16 dynamics provides the versatility necessary to induce stress-specific gene expression at the appropriate level.

4.2. RESULTS

4.2.1. DAF-16 EXHIBITS STOCHASTIC NUCLEAR TRANSLOCATION PULSES UPON STARVATION STRESS

To visualize DAF-16 protein dynamics, we used a transgenic line expressing a functional DAF-16::GFP fusion protein, which has been extensively used in the past to study daf-16 expression and subcellular localization [122]. To quantify dynamics in single cells in multiple animals over time, we developed an automated image analysis framework. As the intestine is thought to be one of the main sites of DAF-16 activity [130], we crossed the *daf-16::GFP* with the *elt-7p::H1-wCherry* line, in which the histone-wCherry protein fusion localizes specifically to the nuclei of intestinal cells (Fig. 4.1C, Fig. S4.1A). Imaging DAF-16::GFP and the intestinal marker allowed us to simultaneously determine nuclei boundaries with high precision and quantify DAF-16 concentration inside and outside the nucleus (Fig. S4.1B, see Methods). As a measure of DAF-16 subcellular localization we used the ratio $R = \frac{I_n}{I_c}$ of the average GFP fluorescence intensity in the nucleus (I_n) to that in the cytoplasm (I_c) of individual intestinal cells.

To investigate DAF-16 protein dynamics in response to stress, we studied the L1 arrest in *C. elegans* larvae, a developmental arrest upon external stresses, such as starvation, that is under control of the IIS [46]. Specifically, we let L1 larvae hatch from bleached eggs, to remove any bacteria that might act as a source of food, inside mi-

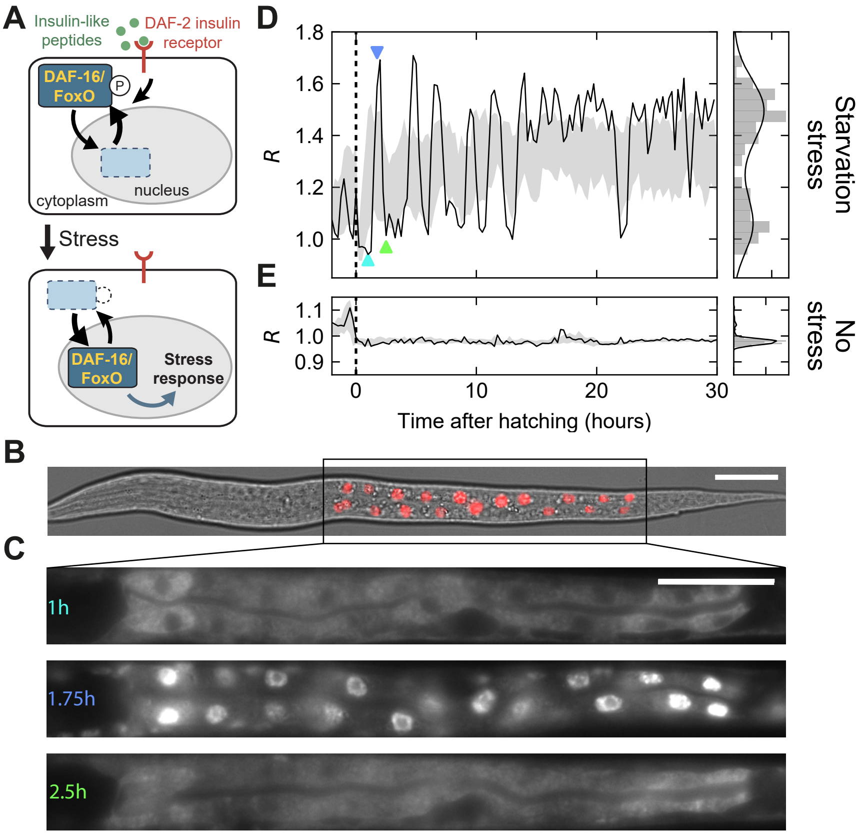

Figure 4.1: DAF-16 undergoes pulsatile dynamics under starvation stress. **(A)** Cartoon representation of the Insulin/insulin-like growth factor-1 signaling (IIS) pathway (see Introduction). **(B)** Transmitted light image of a *C. elegans* L1 larva, overlaid with the fluorescence image of H1-wCherry, localized in intestinal cells (red). Scale bar is 20 μm. **(C)** Fluorescence images of DAF-16::GFP in the intestinal cells of the starved L1 larva at different times after hatching show alternating nuclear and cytoplasmic DAF-16 localization. Scale bar is 20 μm. Images in panels B and C were computationally straightened for visualization (see Chapter 2). **(D, E)** DAF-16::GFP subcellular localization calculated as the ratio $R = I_n/I_c$ of the mean GFP fluorescence intensity in the nucleus (I_n) to that in the cytoplasm (I_c) of intestinal cells, averaged over all cells in (D) L1 larva subject to starvation stress (hatched in liquid media in the absence of food) and (E) L1 larva grown in abundance of *E. coli* bacteria, i.e. without stress (control). Arrowheads in (D) correspond to images in panel (C). Time resolution is 15 minutes. Black lines in both panels correspond to single larvae, while gray bands show average $R\pm$ SD across animals in that condition, $n = 17$ (D) and $n = 25$ (E). Right panels show probability density P_d of R in a single animal. R values close to 1 indicate cytoplasmic DAF-16, while higher values indicate nuclear DAF-16. Overall, these results show that DAF-16 shuttles between the nucleus and the cytoplasm in a pulsatile fashion in L1 larvae subject to constant starvation stress, while it is continuously localized to the cytoplasm in the absence of stress. DAF-16 translocations were also observed in the absence of the nuclear marker H1-wCherry (data not shown).

crochambers filled with liquid media lacking nutrients (see Methods). We found that in animals that hatched in complete absence of nutrients, DAF-16 localization was initially cytoplasmic and quickly translocated to the nucleus, as expected. Strikingly, DAF-16 soon moved back to the cytoplasm in all cells, and continued to shuttle between the nucleus and the cytoplasm in a pulsatile fashion, in stark contrast with current models [122] (Fig. 4.1B, C). Translocation took place in remarkable synchrony between all intestinal cells, at least at a 15-minute time resolution (Fig. S4.1C). Visual inspection suggested that these pulses were also synchronized with many other cells throughout the body that also expressed DAF-16 ((Fig. S4.2)). Given this synchrony, we decided to simplify further analysis by averaging the signal from all intestinal cells in order to obtain a single DAF-16 localization trajectory per animal ($R(t)$, Fig. 4.1D). Notably, even though DAF-16 translocation dynamics exhibited clear variation between individuals, the observed patterns of DAF-16 translocations did show characteristics, with regular short pulses in the first ~ 10 hours after the onset of stress, which afterwards become gradually longer, as apparent when averaging across individual animals (Fig. 4.1D). It is important to note that, for each animal, hatching and, consequently, the onset of stress, took place at a different absolute time within an experiment, but traces are shown aligned by time of hatching. Therefore, the observed similarity in pulsatile dynamics between animals is not an artifact arising from instrumental or environmental fluctuations, but rather suggests an inherent stress response pattern, conserved among individuals.

Additional observations confirmed that DAF-16 pulsatile dynamics originated from the stress response that is mediated by the insulin signaling pathway. First, consistent with established knowledge [122], we found that DAF-16 was almost exclusively localized to the cytoplasm in the absence of stress (*ad libitum* feeding on *E. coli* bacteria at 20 °C), as seen in the constant low value of DAF-16 nuclear ratio $R(t)$ during the 30 hours of imaging (Fig. 4.1E). Of note, we always observed a DAF-16 nuclear pulse prior to hatching, in both unstressed and stressed animals (Fig. 4.1D, E). Second, upstream disruptions in the insulin signaling pathway strongly modified DAF-16 pulse dynamics. In animals carrying a *daf-2(e1368)* mutation that affects the conformation of the extracellular domain and thus partially impairs the proper activation of the DAF-2 insulin receptor [114, 131], DAF-16 was almost exclusively localized to the nucleus under starvation stress (Fig. 4.2). Occasionally, DAF-16 translocated to the cytoplasm for short (~ 1 hour) periods (Fig. 4.2A, Fig. S4.3A-C). In the presence of food, we observed a slightly elevated DAF-16 nuclear ratio $R(t)$ in *daf-2(e1368)* animals, when compared to wild-type, indicative of a higher amount of DAF-16 inside the nucleus (Fig. S4.3D). Interestingly, a stronger allele *daf-2(e1370)*, which disrupts the receptor's kinase activity [114, 131], resulted in an even stronger DAF-16 activation, both under starvation (Fig. S4.3E-G) and in the presence of food (Fig. S4.3H): animals exhibited a higher DAF-16 nuclear level $R(t)$ as compared to the *daf-2(e1368)* mutation, and did not display sporadic translocations to the cytoplasm. Overall, these data support the notion that DAF-16 pulsing is an inherent property of the insulin signaling pathway and is modulated by DAF-2 activity. Recently, multiple transcription factors were found to perform pulsatile regulation in unicellular organisms and isolated cells, repeatedly translocating between the nucleus and cytoplasm under a constant level of

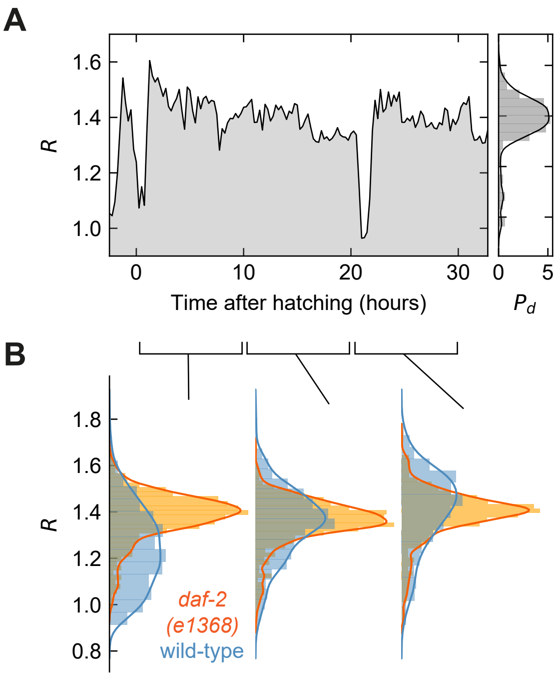

Figure 4.2: DAF-16 pulsatile dynamics is modulated by the activity of insulin receptor daf-2. **(A)** DAF-16 localization trajectory $R(t)$ in a single *daf-2(e1368)* larva subject to starvation stress (left panel) and the corresponding probability density of R (right panel). $R < 1$ indicates cytoplasmic DAF-16, while $R > 1$ indicates nuclear DAF-16. Here, DAF-16 is localized to the nucleus for most of the time, but occasionally translocates to the cytoplasm. **(B)** Probability density P_d of DAF-16 subcellular localization R for wild-type (blue, $n = 17$), and *daf-2(e1368)* animals (orange, $n = 22$), computed from different time intervals (0-10, 10-20 and 20-30 hours after the onset of starvation stress). The peak of the P_d distribution shifts towards higher R values as time progresses in wild-type animals, indicating that nuclear pulses become longer (Fig. 4.1D). In contrast, the P_d distribution remains centered at high R values in *daf-2(e1368)* animals, indicating an almost constant nuclear DAF-16 localization from the start. Overall, these results show that DAF-16 pulsatile dynamics occurs as a result of insulin signaling and is modulated by DAF-2 activity.

stimulus [132–138]. Yet this is, to our knowledge, the first time that pulsatile activation of a transcription factor is observed inside a multicellular organism.

4.2.2. DAF-16 DYNAMICS CHANGES DEPENDING ON THE TYPE OF STRESS

Transcription factors are often involved in the activation of multiple gene expression programs that serve very different functions. Particularly, DAF-16 mediates the response to various stresses that require the upregulation of different sets of target genes [124]. How a single transcription factor, DAF-16, can induce the correct set of target genes based on extracellular signals remains an intriguing question. A potential advantage of pulsatile transcription factor regulation is that more information can be transmitted via the frequency, duration and/or amplitude of pulses, compared to a more deterministic regulation, where the nuclear localization of a transcription factor remains constant under a constant stress level [138]. In other words, complex patterns, possible in a pulsatile system, could allow the mapping of a variety of upstream signals to different gene expression programs. This model predicts that different stresses would give rise to different DAF-16 pulsatile dynamics.

To test whether DAF-16 dynamics changes depending on the type of stress, we exposed DAF-16::GFP animals to different unfavorable environmental conditions that are known to induce L1 arrest in *C. elegans* larvae [54]. In addition to starvation, we followed DAF-16 dynamics upon induction of heat and osmotic stress by exposing animals to either extreme temperature or salt concentration, respectively. For osmotic stress, late embryos were placed inside the microchambers pre-incubated in 300 mM NaCl solution (see Methods). To induce heat stress, animals were first allowed to hatch at 20 °C, followed by a sudden shift to 32 °C in the newly hatched L1 larvae. For both types of stress, animals were given *ad libitum* food, in contrast to the starvation experiments. Osmotic stress, similar to starvation, resulted in DAF-16 shuttling between the nucleus and the cytoplasm in repeated pulses. However, in response to osmotic stress, DAF-16 pulses appeared less regular, compared to pulses that occurred during starvation (Fig. 4.3B, Fig. S4.5). This notion was further confirmed by autocorrelation analysis of individual traces for both starvation and osmotic stress. For most animals subject to starvation stress the autocorrelation displayed evenly-spaced peaks, consistent with a periodic signal with a period of 2.2 ± 0.3 hours (Fig. 4.3D, Fig. S4.6). In spite of the variability in DAF-16 dynamics between individual animals (see Section 4.2.4), these peaks were still visible after averaging the auto-correlation functions from all animals (Fig. 4.3E), indicating that pulsing in different animals was synchronized to the onset of stress and occurred at a conserved frequency, at least in the first ~ 6 hours of stress exposure. Interestingly, starvation stress at higher (25 °C) or lower (15 °C) temperature displayed similar pulsatile patterns, but with faster or slower period, respectively (Fig. S4.6F). This is consistent with how the speed of larval development depends on temperature (see Chapter 2) and might reflect the notion that diffusion and reaction kinetics in cells are accelerated at higher temperatures. Overall, these data indicate that pulsing period and phase are remarkably conserved across individual animals under constant starvation stress. In contrast, the autocorrelation analysis for osmotic stress did not reveal a strong, consistent periodicity. Indeed, averaging the autocorrelation functions from

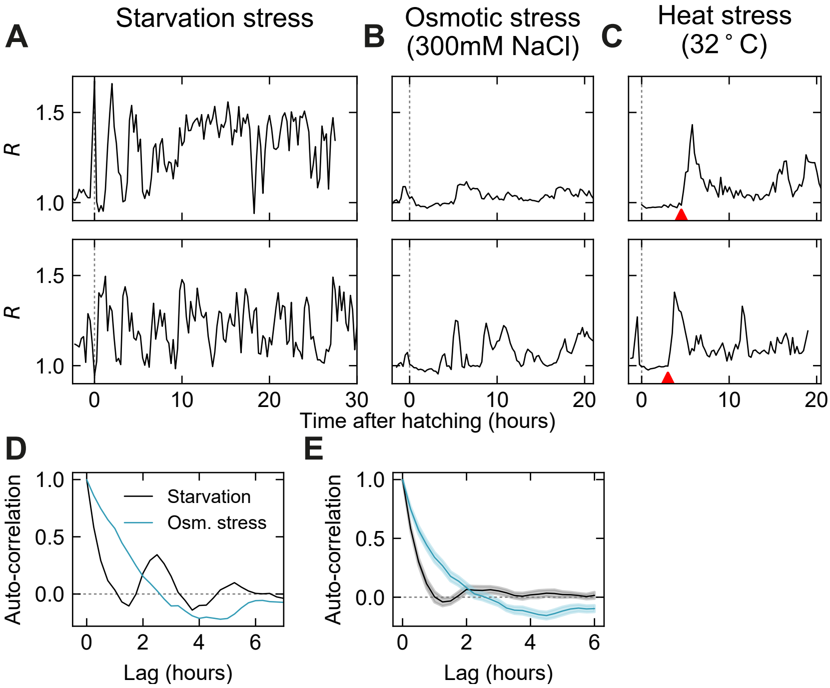

Figure 4.3: DAF-16 pulsatile dynamics changes depending on the type of stress. **(A-C)** DAF-16::GFP localization trajectories $R(t)$ in larvae subject to **(A)** starvation stress, **(B)** osmotic stress (300 mM NaCl) and **(C)** heat stress (32 °C). Upper and lower panels are different individuals. Time is relative to hatching, which also corresponds to the onset of starvation and possibly osmotic stress (see text). Red arrowheads in (C) mark the onset of heat stress. Temperature was 20 °C in all cases, except after the onset of heat stress in (C). $R < 1$ indicate cytoplasmic DAF-16, while $R > 1$ indicate nuclear DAF-16. While starvation and osmotic stress both gave rise to nuclear pulses, these appeared more regular at starvation than for osmotic stress. Heat stress resulted in an immediate DAF-16 translocation into the nucleus, followed by a decrease of R to a lower baseline level of nuclear localization. **(D)** Auto-correlation function of $R(t)$ for single animals under starvation (black) or osmotic stress (blue), shown in upper panels in (A) and (B), respectively. In an animal subject to starvation, auto-correlation displayed evenly-spaced peaks, consistent with a periodic signal with a period of 2.2 ± 0.3 hours (Fig. S4.6F). In case of osmotic stress, auto-correlation decayed slowly and did not display peaks, indicating a more random character of DAF-16 pulses. **(E)** Average auto-correlation functions of DAF-16 localization trajectories from a population of animals subject to starvation (black, $n = 17$) or osmotic shock (blue, $n = 16$, 300 mM NaCl). For starvation, peaks were still visible after averaging the auto-correlation functions from all animals, indicating conserved pulse frequency and phase.

all the animals under osmotic stress further confirms that there was no conserved period (Fig. 4.3E). Upon the induction of heat stress, we observed a rapid translocation of DAF-16 into the nucleus, as seen in the sharp increase in the DAF-16 nuclear ratio $R(t)$, followed by a relaxation to a slightly lower nuclear level (Fig. 4.3C, Fig. S4.4). After that, we observed occasional peaks in nuclear DAF-16. However, they occurred relative to the new baseline and the R value never returned to its pre-stress level, indicating continuous presence of DAF-16 in the nucleus. This was in stark contrast to the starvation and osmotic stress, where all of the DAF-16 protein appeared to be exported back to the cytoplasm in between the pulses of nuclear localization (Fig. 4.3A, B).

In summary, DAF-16 translocation patterns differ depending on the type of stress. While starvation and osmotic stress both resulted in pulsatile dynamics, pulses appeared regular at starvation stress, but not at osmotic stress. In contrast to starvation and osmotic stress, heat stress lead to a single high-amplitude DAF-16 pulse, followed by a decrease to a lower nuclear level. Overall, these results indicate that pulsatile dynamics in itself provides sufficient information to discriminate different stresses using a single transcription factor.

4.2.3. DAF-16 DYNAMICS CHANGES WITH THE MAGNITUDE OF STRESS

We have shown here that DAF-16 localization dynamics is stress-specific. In the wild, *C. elegans* often encounters a wide range of temperatures and salt concentrations and hence should also be able to cope with varying magnitudes of stress [109]. It is therefore important that the stress response is adjusted to the level of stress experienced by the animal. Potentially, this could be achieved through modulation of the transcription factor localization dynamics. To test this hypothesis, we exposed individual animals to different levels of stress and searched for changes in DAF-16 localization patterns.

First, we varied nutrient availability, by filling the chambers with low-concentration bacterial dilutions, and observed that DAF-16 remained cytoplasmic while bacteria were available, even if scarce. However, once animals had eaten virtually all the food inside the microchambers (~ 2 hours after hatching) DAF-16 started again to translocate between the nucleus and the cytoplasm in the pulsatile manner (Fig. S4.7). This observation suggests that *C. elegans* can sense very small amounts of bacteria and may only mount a starvation stress response upon complete nutrient deprivation. Dynamics of DAF-16 localization could be different when animals are subject to a constant, low level of available food for a prolonged period of time. However, such a condition is challenging to impose using our microchamber approach. Next, we exposed animals to different degrees of osmotic stress, by increasing the salt concentration from 200-400 mM NaCl, as these concentrations were previously shown to induce stress response [139, 140]. This resulted in an increase in the time DAF-16 spent in the nucleus without a strong impact on the amplitude of nuclear DAF-16 pulses (Fig. 4.4A-C). At 200 mM NaCl, DAF-16 was predominantly localized to the cytoplasm with a few occasional pulses of nuclear localization. The pulse duration (for details on quantification, see Methods) increased with salt concentration from 1.1 ± 0.8 hours at 200 mM to 2.5 ± 2.4 hours at 300 mM NaCl, turning into almost con-

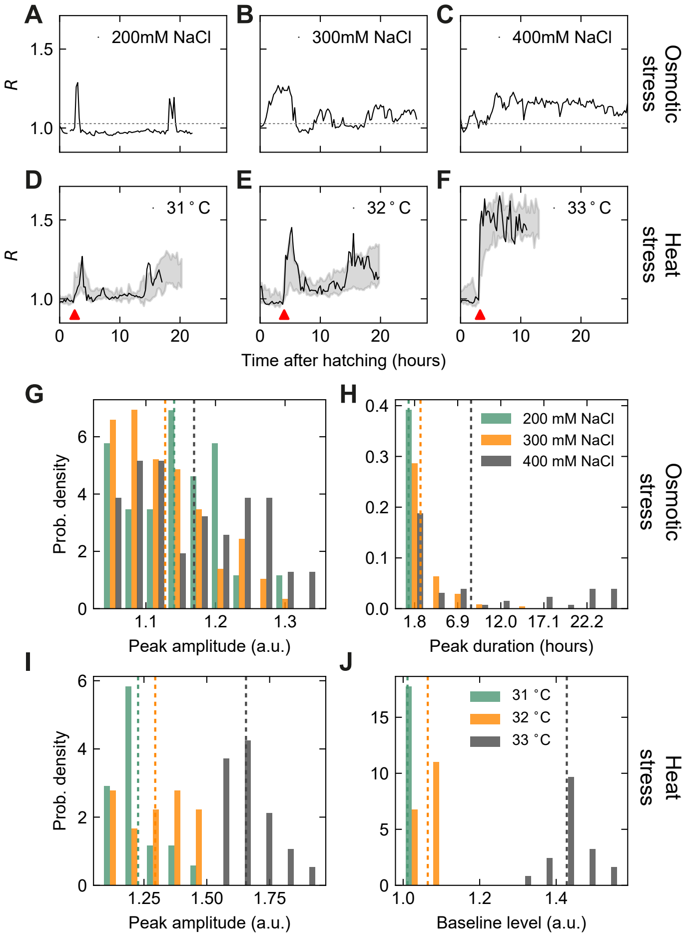

Figure 4.4: DAF-16 pulsatile dynamics changes with the magnitude of stress. **(A-F)** DAF-16::GFP localization trajectories $R(t)$ in different larvae subject to either osmotic stress at **(A)** 200 mM NaCl, **(B)** 300 mM NaCl and **(C)** 400 mM NaCl, or to heat stress of **(D)** 31 °C, **(E)** 32 °C and **(F)** 33 °C. $R < 1$ indicate cytoplasmic DAF-16, while $R > 1$ indicate nuclear DAF-16. Dashed lines in (A-C) indicate the threshold used to separate the pulses of nuclear DAF-16, calculated as the baseline R without stress multiplied by a fixed factor of 1.05 (see Methods for details). Red arrowheads in (D-F) represent the time at which temperature is shifted from 20 °C to the corresponding temperature. Gray bands show average R across animals in that condition ± SD, aligned to the onset of heat stress. $n_{31} = 20$, $n_{32} = 21$, $n_{33} = 22$. **(G-H)** Quantitative analysis of DAF-16 pulses in animals subject to osmotic stress. Duration **(G)** and amplitude **(H)** of DAF-16 pulses were obtained by thresholding R as described above. The amplitude was defined as the maximum value of a pulse. $n_{200} = 22$, $n_{300} = 18$, $n_{400} = 21$. These data show that the pulse duration, but not pulse amplitude, increased with salt concentration. **(I-J)** Quantitative analysis of the shape of DAF-16 localization trajectory in animals subject to heat stress. Amplitude of the peak was calculated as the maximum value during the first 2.5 hours after the temperature shift **(I)** and the subsequent baseline was calculated as the average among the lowest 10% R values at any time after heat shock **(J)**. These results indicate that both the height of the initial peak and the subsequent baseline value increased with temperature.

stant nuclear localization at 400 mM NaCl (8.5 ± 9.0 hours, Fig. 4.4H). In particular for 400 mM NaCl, some experiments ended before the end of the pulse, and, hence, these numbers represent a lower limit for the actual pulse duration. Pulse amplitude, in contrast, did not significantly increase with salt concentration (1.14 ± 0.06, 1.13 ± 0.07 and 1.17 ± 0.08, respectively, Fig. 4.4G). It is important to note that the onset of osmotic stress may not occur at hatching. Even though the eggshell is impermeable to small molecules such as NaCl [141], larval movement is also known to soften the shell around 1 hour prior to hatching [75]. This change in the mechanical properties of the eggshell could thus be accompanied by an increase in permeability. In fact, at high salt concentrations we observed that a fraction of embryos (3/18 at 300 and 10/32 at 400 mM NaCl) did not hatch normally, but rather stopped the active motion that typically occurs in late embryos prior to hatching [142]. In these animals, cessation of embryonic motility was interpreted as hatching for analysis. Overall, changes in the magnitude of osmotic stress translated into changes in the duration of DAF-16 pulses and not their amplitude.

Finally, we exposed different animals in the early L1 larval stage to 31-33 °C, as described in section 4.2.2. Immediately after the shift from 20 °C to the corresponding temperature, DAF-16 translocated into the nucleus (Fig. 4.4D-F), which was then rapidly followed by a decrease of the DAF-16 nuclear ratio $R(t)$ to a new baseline. Both the height of the initial peak (1.2 ± 0.1, 1.3 ± 0.1 and 1.6 ± 0.1 at 31, 32 and 33 °C, respectively) and the subsequent baseline value (1.01 ± 0.01, 1.1 ± 0.2 and 1.43 ± 0.06) increased with temperature (Fig. 4.4I, J). At 31 and 32 °C, nuclear DAF-16 started increasing again after ~ 12 hours of heat exposure (Fig. 4.4D, E). Due to fast deterioration of the microchamber hydrogels at 33 °C, we could only image the animals for ~ 10 hours. During that time, in contrast to lower temperatures, there was no drop in nuclear DAF-16, suggesting that exposure to 33 °C requires a sustained and strong stress response (Fig. 4.4F). These observations show that the amount of DAF-16 proteins in the nucleus upon the heat shock increases with the applied temperature.

Together, these results indicate that DAF-16 dynamics might not only encode the information about the stress type, but also about its magnitude. Interestingly, the adjustment to higher levels of stress were achieved differently for osmotic and heat stress, highlighting the versatility of pulsatile dynamics to process different signals.

4.2.4. VARIABILITY IN DAF-16 DYNAMICS

DAF-16 dynamics showed variability among individual animals subject to identical conditions, in particular in the number of DAF-16 peaks, their duration and the times at which they occurred. To better characterize the inter-individual variability in DAF-16 localization dynamics at different stresses, we first binarized DAF-16 localization into cytoplasmic or nuclear (Fig. 4.5A-F), and calculated φ_N, the fraction of time DAF-16 has spent in the nucleus since the onset of stress (Fig. 4.5G-I, see Methods). For each individual, the value of φ_N at a particular time reflects its DAF-16 pulse dynamics history up until that time.

For starvation stress, all φ_N traces started at or rapidly dropped to zero, as after hatching DAF-16 was typically localized in the cytoplasm. Right after, φ_N increased for all traces as pulses initiated, although following variable paths, and finally they

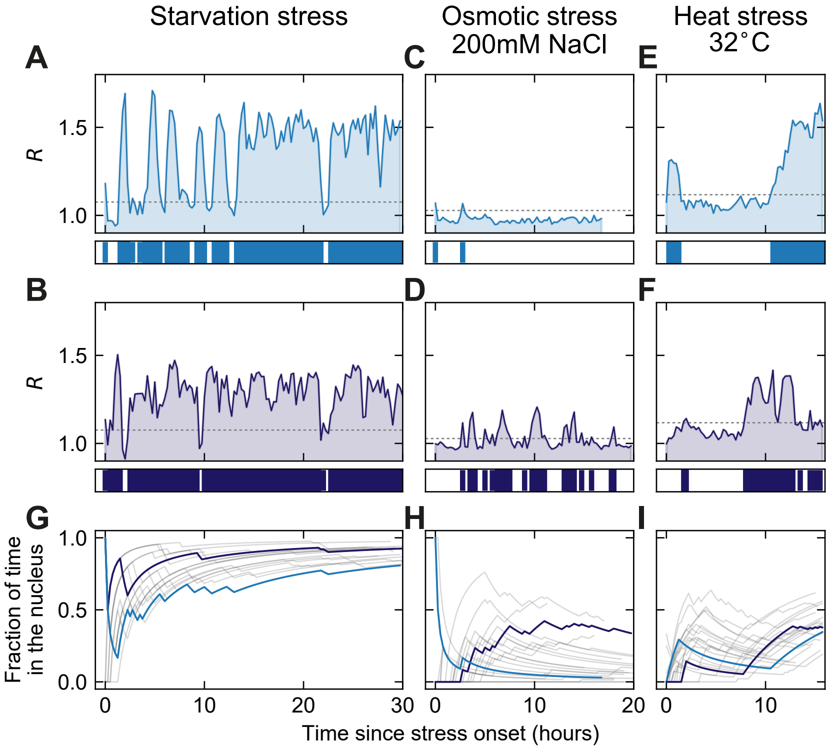

Figure 4.5: Variability in the dynamics of DAF-16 nuclear translocations. DAF-16::GFP subcellular localization in individual larvae subject to **(A, B)** starvation stress, **(C, D)** osmotic stress (200 mM NaCl) and **(E, F)** heat stress (32 °C). DAF-16 localization was classified as cytoplasmic or nuclear using a set R threshold (dashed line, see Methods), and localization traces were converted into binary sequences (bottom panels). **(G-I)** Fraction of time DAF-16::GFP spent in the nucleus (see Methods) as a function of time for **(G)** $n = 17$ larvae subject to starvation stress, **(H)** $n = 22$ larvae subject to osmotic stress (200 mM NaCl) and **(I)** $n = 21$ larvae subject to heat stress (32 °C). The highlighted lines in panels (G-I) correspond to animals in (A, B), (C, D) and (E, F), respectively. These data show significant variability in DAF-16 localization pattern among animals subject to identical stress conditions.

converged towards $\varphi_N = 1$ after ~ 20 hours, when long nuclear plateaus dominate DAF-16 localization after prolonged exposure to stress (Fig. 4.5A, B, G).

Osmotic stress also displayed inter-individual variability. At 200 mM NaCl, DAF-16 was continuously localized to the cytoplasm in some animals, while others exhibited multiple nuclear pulses (Fig. 4.5C, D). In contrast to starvation, φ_N traces followed very different paths and did not steadily approach 1, even after prolonged exposure to osmotic stress, reflecting the lack of long nuclear plateaus in pulsatile dynamics (Fig. 4.5H). For heat stress, DAF-16 dynamics followed a general and consistent pattern, which is most apparent from the data averaged over all animals (gray band in Fig. 4.4D-F), with a high nuclear peak right after stress, followed by a decrease to a new baseline and late nuclear translocations (Fig. 4.5E, F). Animal-to-animal variability was most pronounced in the duration of the first peak and in the onset of the late nuclear translocation (> 12 hours, Fig. 4.5I). Overall, there was significant variability in DAF-16 localization pattern among animals subject to identical stress conditions.

4.2.5. DAF-16 TRANSLOCATIONS OCCUR IN ANTERIOR-TO-POSTERIOR ORDER IN INTESTINAL CELLS

DAF-16 nuclear translocations appear highly synchronized between intestinal cells at a 15-minute imaging interval (Fig. S4.1C). Potentially, such synchronization could be established by an extracellular signal. If such signals are produced by a single cell or a group of cells with a specific location inside the body, we would expect that some cells sense and process the signal before others, potentially resulting in systematic differences in DAF-16 activation times between individual cells. Such differences were not visible at the time resolution that allowed for imaging of DAF-16 pulse dynamics for many hours. We therefore wondered whether temporal differences in DAF-16 translocations between cells would emerge when imaged at higher time resolution.

We performed high-speed imaging at 30-second time resolution, annotated the identity of all intestinal cells (Fig. 4.6A) and quantified their individual DAF-16 nuclear ratio $R(t)$ at every time point during starvation stress (Fig. 4.6B). At this increased time resolution, we could clearly observe the gradual translocation of DAF-16 in and out of the nucleus, a process which took around 20 minutes. DAF-16 translocations were still highly coordinated among cells, but the $R(t)$ trajectories now appeared slightly shifted in time for different cells (Fig. 4.6B). To examine whether there was systematic delay between cells, we performed cross-correlation analysis of the DAF-16 trajectories between each pair of cells (Fig. 4.6C). We then determined the lag time τ, corresponding to the maximum of the cross-correlation curves, as a measure of the delay between the two cells. This was close to zero for neighboring cells (i.e. no delay), for instance between cells Int2D and Int2V (Fig. 4.6C). In contrast, the peak shifted to higher lag times for increasingly distant cells (Fig. 4.6C). To verify that shifts in the curves indicate actual delays in the DAF-16 localization signal between cells, we calculated their uncertainty using a model-independent Monte Carlo simulation (see Methods, Fig. S4.8). For instance, the signal from the Int2V cell seemed to precede that from all other intestinal cells, i.e. all cross-correlation curves peaked at a time larger than zero. However, the observed shift in the cross-correlation curve was not statistically significant for its immediate neighbours, Int2D and Int3V, as the

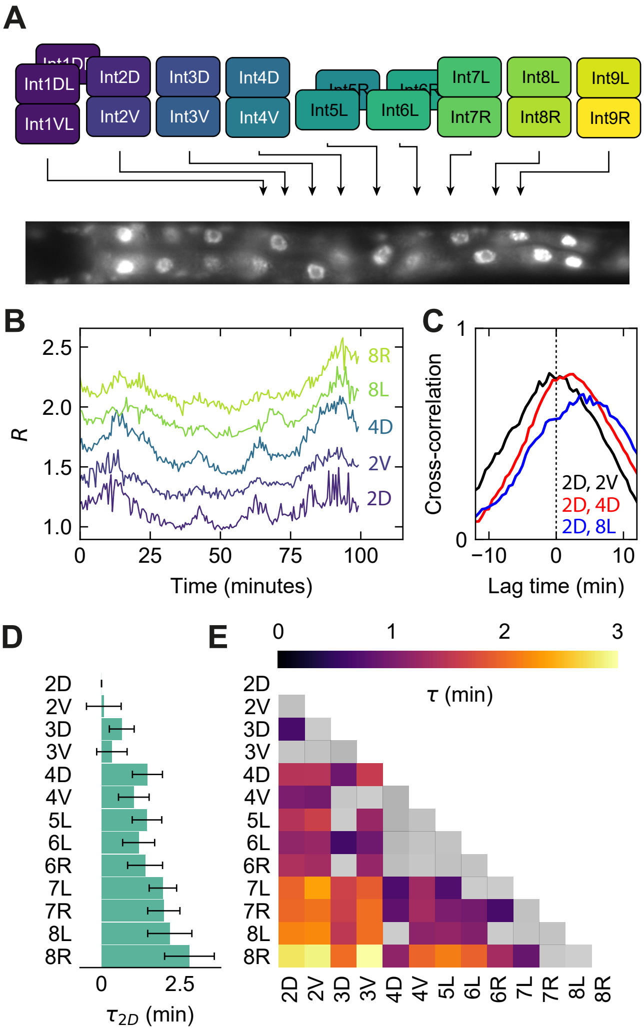

Figure 4.6: High time resolution imaging and cross-correlation analysis reveals sequential DAF-16 dynamics in intestinal cells. **(A)** Intestinal cells in the starved L1 larva with corresponding names (H1-wCherry). Scale bar is 15 μm. **(B)** DAF-16::GFP localization trajectories R of individual intestinal cells in one L1 animal subject to starvation stress, imaged at 30-second time resolution. Individual tracks are shifted along the y-axis for clarity. Possible delays between cells are not immediately obvious from visual inspection. **(C)** Cross-correlation of DAF-16 localization trajectories from different pairs of cells also shown in (B). The lag time τ between each cell-pair is reflected in a shift of the cross-correlation peak, which here increases for cells that are located further apart along the body. **(D)** Delay τ between Int2D and all other intestinal cells. Error bars are estimated as the 95% confidence interval of the peak centroid distributions obtained from Monte-Carlo simulations (see Methods). Data is averaged across $n = 5$ animals. **(E)** Heatmap showing the delay τ between all pairs of intestinal cells, averaged across $n = 5$ animals. Gray squares indicate that the delay is not significantly different from 0 ($\tau = 0$ lies within the error bar). Overall, the trend indicates that delays in the DAF-16 translocation signal increase with the distance between the cells, and suggests that the stress response might be synchronized throughout the body with an anterior-posterior propagating extracellular signal.

98% confidence interval (represented by the error bars) included the value zero (Fig. 4.6D). Therefore, DAF-16 translocation seemed to occur without delay (at least within less than 30 seconds difference) for these cells. The overall trend observed when computing all cell-pair delays is an increasing delay in DAF-16 translocation for cells further away from the head. In other words, DAF-16 translocations seem to occur in an anterior-to-posterior wave in intestinal cells, where anterior cells are the first to display the pulse and subsequent cells follow within a few minutes in spatial order (Fig. 4.6E). Notably, the time scale of the delay in DAF-16 translocation between cells is ~ 5-10 times faster than the translocation process itself. Overall, these results are consistent with an extracellular signal that travels from the anterior part of the body to synchronize DAF-16 localization dynamics in intestinal cells.

4.2.6. DAF-16 DYNAMICS EXHIBITS PULSATILE DYNAMICS IN AN ENDOGENOUSLY TAGGED STRAIN

Experiments shown in previous sections were performed on animals that carry the integrated *zIs356* transgene and likely overexpress DAF-16 above the physiological level. Moreover, the *zIs356* transgene only tags the DAF-16a/b isoforms, and not the DAF-16d/f. While this work was in progress, we in parallel constructed an endogenous translational fluorescent reporter, DAF-16::wrmScarlet, and an additional single-copy strain (DAF-16::mNeonGreen) became available [143]. In these strains, DAF-16 protein is present at a lower, physiological level, and all DAF-16 isoforms are tagged.

For the DAF-16:mNeonGreen strain, we observed clear DAF-16 pulses in hypodermal cells of L1 larvae subject to starvation (Fig. 4.7B). Pulses were less obvious in intestinal cells under this condition (Fig. 4.7A), but clearly visible in unhatched embryos subject to osmotic stress (400 mM, Fig. S4.9). For the DAF16::wrmScarlet, in contrast, we did not observe pulses in the L1 larvae subject to starvation stress. Instead, DAF-16 slowly accumulated in the nuclei of intestinal cells and did not translocate back to the cytoplasm, at least during the course of our experiment (~ 10 hours, data not shown). Nevertheless, pulses were observed in older animals (approximately L3-L4 larval stage) upon late food depletion (Fig. S4.10A), similar to the *zIs356* strain (Fig. 4.1). Interestingly, in the DAF-16::wrmScarlet strain, the delay in DAF-16 nuclear translocation between anterior and posterior cells was more pronounced and clearly visible in static images (Fig. S4.10B). Overall, the fact that we observe DAF-16 nuclear shuttling in single-copy strains further confirms that pulsatile dynamics is a real physiological phenomenon.

4.2.7. FOXO3A UNDERGOES PULSATILE DYNAMICS IN HUMAN CELLS

We showed here that DAF-16 undergoes pulsatile dynamics in *C. elegans* under starvation stress. DAF-16 belongs to the FOXO family of transcription factors, which is widely conserved across animal kingdom [111]. While *daf-16* is the only FOXO gene in *C. elegans* [118], it has four homologs in humans (FOXO1, FOXO3a, FOXO4 and FOXO6), which are involved in a wide range of age-related disorders, such as Alzheimer's disease, cancer and diabetes, among others [144]. Moreover, FOXO3a has

A

Focus on intestinal cells

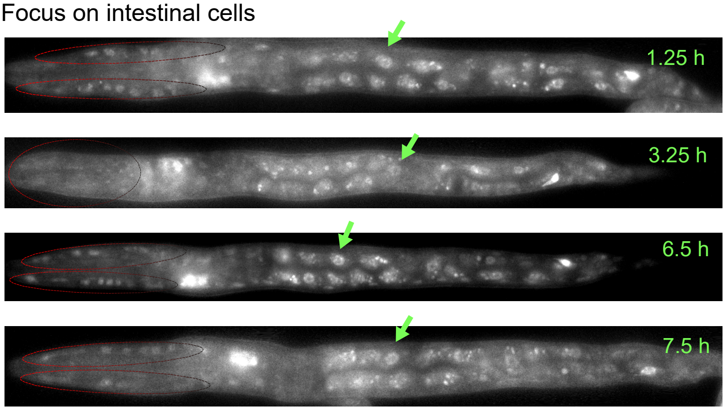

B

Focus on hypodermal cells

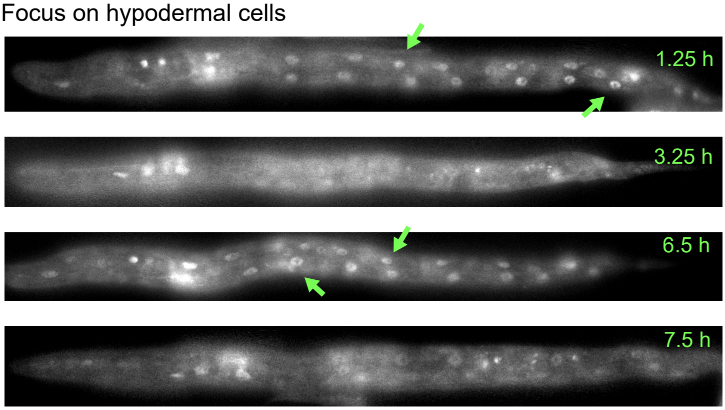

Figure 4.7: DAF-16 pulsatile dynamics in an endogenously tagged strain. Fluorescent images of DAF-16::mNeonGreen (endogenously tagged) strain focusing on **(A)** intestinal cells and **(B)** hypodermal cells in L1 larva subject to starvation. Time from hatching. DAF-16 is mostly localized to the nucleus (first and third panels) and to the cytoplasm (second and fourth panels). DAF-16 pulsing can also be observed in the head neurons (highlighted by red circles in A).

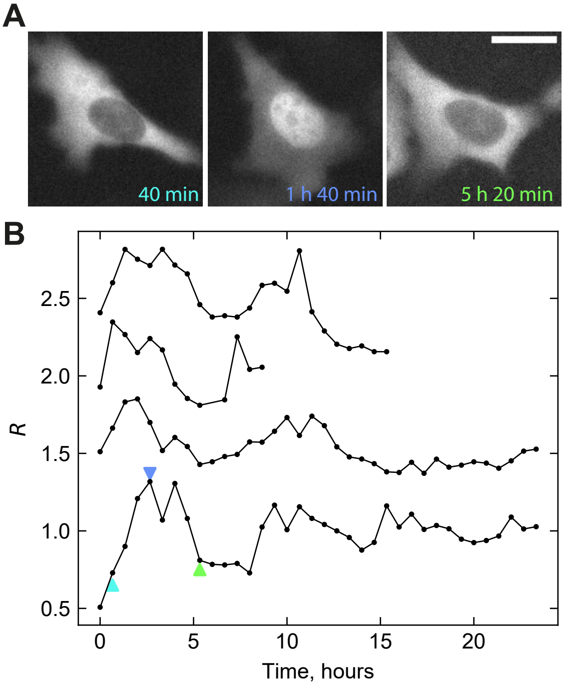

Figure 4.8: FOXO3A undergoes pulsatile dynamics in human bone osteosarcoma U2OS cells. **(A)** Fluorescence images of FOXO3A::GFP in a human bone osteosarcoma U2OS cell at 0% FBS, at different times since the start of experiment, corresponding to the arrowheads in panel B (lowest trace). Scale bar is 25 μm. **(B)** FOXO3A::GFP subcellular localization calculated as the ratio R of average fluorescence intensity in the nuclei to that of the cytoplasm of U2OS cells. Traces correspond to different individual cells and the lowest trace corresponds to the cell shown in panel A. For visualization, the 3 upper traces were shifted by 0.5, 1 and 1.5 in R, respectively.

been associated with extended lifespan in humans [144]. It is thus an intriguing question, whether pulsatile dynamics is specific to *C. elegans* or rather a general feature of insulin signaling.

To answer this question, we transfected human osteosarcoma U2OS cell line with a plasmid carrying FOXO3A::GFP. *In vitro* cell culture is usually supplemented with 10% fetal bovine serum (FBS) that provides cells with growth factors and nutrients necessary for growth and proliferation. To induce starvation stress, we placed U2OS cells in 0% FBS media and followed FOXO3A::GFP subcellular localization for ~ 20 hours. Strikingly, we indeed observed that in most cells FOXO3A translocated between the nucleus and cytoplasm in repeated pulses (Fig. 4.8). These pulses occurred at a much slower pace than in *C. elegans*, with a ~ 5 – 10-hour period. Overall, our results indicate that pulsatile regulation by FOXO transcription factors might be a general feature of the insulin signaling pathway.

4.3. DISCUSSION

In the current model of the IIS pathway, DAF-16 is thought to translocate to the nucleus upon stress and remain there until the stress has passed [122]. Here, in contrast, we have shown that DAF-16 undergoes pulsatile dynamics, shuttling between the cytoplasm and the nuclei of intestinal cells in a coordinated manner, in newly-hatched *C. elegans* larvae subject to constant levels of environmental stress (Fig. 4.1C-D). These pulses occurred as a result of different stresses and depended on the upstream activity of the insulin receptor DAF-2, suggesting that pulsatile dynamics is an intrinsic feature of the animal's stress response (Fig. 4.1E, Fig. 4.2).

Pulsatile dynamics is currently emerging as a widespread mechanism of transcription factor regulation in various systems [138]. Common general elements behind pulse generation have been identified, such as non-linearity, noise and feedback control [138]. Non-linearity implies that a small change in the upstream pathway, impacting the signaling state of the cell, would lead to a sudden switch in the subcellular localization of a transcription factor, e.g. sudden translocation of DAF-16 into the nucleus. The second common prerequisite of pulsatile dynamics - feedback control - ensures that the transcription factor eventually moves back to the cytoplasm, by activating factors that interfere with the upstream pathway. We envision two qualitatively different mechanisms by which this can occur. First, such factors could act in a purely intracellular manner, for instance by influencing the activity of the proteins, such as AKT-1/2, that control DAF-16 phosphorylation and, thus, DAF-16 localization. Alternatively, such factors could be secreted outside of the cell. Here, interesting candidates would be the insulin-like peptides (ILPs), which impact DAF-16 phosphorylation and nuclear translocation through the DAF-2 receptor. In this mechanism, nuclear DAF-16 induces expression of ILPs, which are later secreted out of the cell and bind to the DAF-2 receptor, thereby causing phosphorylation of DAF-16 and its cytoplasmic retention. In line with this notion, DAF-16 has been shown to induce expression of different ILPs [116, 145].

In addition, we have shown here that DAF-16 translocation dynamics differs depending on the type and the magnitude of the applied stress (Figs. 4.3 and 4.4). How these differences in translocation dynamics arise remains to be discovered. One attractive possibility is that the vast repertoire of ILPs provides the flexibility needed to encode diverse upstream conditions into distinguishable patterns of DAF-16 translocation dynamics. Indeed, *C. elegans* has at least 40 different ILPs that either stimulate or antagonize insulin signaling, by binding to the sole insulin receptor DAF-2 [115, 146]. The ILP family has a complex spatiotemporal expression pattern and is likely to exhibit complicated patterns of redundancy, where groups of ILPs function together to initiate an appropriate response under different environmental conditions [117]. One could speculate that the differences in DAF-16 localization dynamics at different stresses reflect DAF-2 activity modulation by the binding of different combinations of ILPs. For instance, it has been shown that the ILPs *daf-28*, *ins-6* and *ins-1* encode different sensory cues to promote two distinct developmental switches, namely entry into (*ins-1*) and exit from (*daf-28* and *ins-6*) dauer arrest [147]. At the same time, other signaling pathways could function in parallel to the IIS to impact DAF-16 phosphorylation [148].

Why cells would engage in such diverse transcription factor dynamics in response to different stresses is another open question. An attractive possibility is that different DAF-16 translocation patterns encode information about the type and magnitude of stress, and are then decoded to activate tailored downstream gene expression programs. Indeed, this phenomenon, termed dynamic multiplexing, has been observed in several biological systems [138]. Examples include the transcription factors NF-κB in mammalian cells and Msn2 in yeast, both of which exhibit pulsatile dynamics that depend on the input signal. Differential gene expression is achieved through the different binding properties and activation kinetics of the target promoters, which are typically classified as those that need a persistent transcription factor activation and those that do not [133, 135, 149–151]. Similar mechanisms could be involved in the IIS pathway in *C. elegans*. In the future, simultaneously monitoring the dynamics of DAF-16 pulses and the expression of its direct target genes could provide insight into how the observed differences in DAF-16 translocation dynamics between different types and magnitudes of stress are converted into differential gene expression.

A common feature of DAF-16 dynamics for all stresses examined here was significant variability in pulse duration and frequency for individual animals subject to identical environmental conditions (Fig. 4.5). Such variability is likely to be propagated and amplified downstream, to the expression of DAF-16 target genes. Interestingly, it was previously shown that exposure to transient heat stress causes a large variation in stress response among the isogenic *C. elegans* population, measured by the induction of chaperone *hsp-16.2*, a known stress-response gene [152, 153]. Indeed, a stronger response correlated with increased subsequent longevity and stress resistance, but reduced progeny, reflecting a trade-off between survival of stress and proliferation [153]. Moreover, the amount of time DAF-16 remained in the nucleus after exposure to transient heat stress varied among individuals and correlated with the increased chaperone induction. It is thus a compelling idea that inter-individual variability in DAF-16 dynamics at constant levels of stress, observed in our work, would likewise serve to diversify the stress response within the population, thereby increasing survival chances [153]. As a species that lives in an unpredictable, rapidly changing environment, *C. elegans* might employ such bet-hedging strategies to ensure the flexibility and adaptability of its species. Such strategy would be particularly advantageous when dealing with transient stresses. For example, when encountering a region with high osmolarity, it might not always be advantageous to mount a strong and costly stress response, as the stress might pass quickly. While our observations likely indicate actual animal-to-animal variability, one should also consider possible effects of environmental variations, such as temperature or salt gradients inside the sample, which were not taken into account here.

DAF-16 pulsing is highly synchronized between different cells in the body, although for intestinal cells an anterior-posterior switching order emerged when examined at high time resolution (Fig. 4.6). One could envision two different models to explain the observed sequential nuclear translocations. A first model would involve the periodic emission of an extracellular signal by pacemaker cells at the anterior region of the body – e.g. neurons. This pulsatile signal would propagate through the body and be sensed by intestinal cells in spatial order to induce a switch in DAF-16 subcellular localization (pacemaker model). Alternatively, cells could generate DAF-16 pulses autonomously, secreting in the process signalling molecules that diffuse and synchronize DAF-16 dynamics in neighbouring cells. Both of these models rely on the presence of a diffusible signal, and again ILPs are interesting candidates, as they are known to be secreted both by head neurons and intestinal cells [115–117]. In the first model, anterior pacemaker cells, e.g. neurons, would emit ILPs in a pulsatile fashion, orchestrating all intestinal cells, while in the local synchronization model, ILPs would be secreted by an intestinal cell upon DAF-16 activation, and sensed by their neighbours. To explore these possible scenarios, it would be interesting to perturb ILP secretion in certain cells, e.g. head neurons. If these cells act as pacemakers, such perturbation would alter the DAF-16 oscillations in other cells.

Importantly, most of the experiments in this study were performed on transgenic animals that likely have multiple copies of the *daf-16* gene and hence overexpress DAF-16 above the physiological level. Moreover, the *zIs356* transgene only tags the DAF-16a/b isoforms, while leaving out DAF-16d/f, which could thus provide an incomplete picture on DAF-16 dynamics. However, the fact that we also observed DAF-16 pulses in the single-copy strains suggests that pulses are a true, general feature of DAF-16 dynamics. These preliminary results form the basis for further investigation.

Finally, in addition to *C. elegans*, we have also observed pulsatile dynamics in FOXO3A, a human ortholog of DAF-16, in starving human osteosarcoma cells (Fig. 4.8). These findings suggest that, rather than being a phenomenon specific to *C. elegans*, pulses are a general feature of the insulin signaling pathway. In the future, it will be important to establish both whether pulsatile dynamics occurs in DAF-16/FOXO orthologs in other systems and whether pulsatile translocation dynamics of transcription factors is a general phenomenon that is more widespread in *C. elegans*.

I would like to thank M. Olmedo for constructing the DAF-16::wrmScarlet strain and performing genetic crosses, M. Sánchez-Romero for the FOXO3A experiments in human cells, and B. Demirbas for performing the DAF-16::mNeonGreen experiments, as well as for his contribution to the cross-correlation analysis.

4.4. METHODS

4.4.1. *C. elegans* EXPERIMENTAL METHODS

STRAINS

To study DAF-16 protein dynamics, we used the existing transgenic line *zIs356*[*Pdaf-16::daf-16a/b-gfp; rol-6*] IV, which expresses a functional DAF-16::GFP fusion protein. To easily detect positions of all intestinal nuclei, we crossed it into the *stIs10131*[*elt-7p::H1-wCherry + unc-119(+)*] strain that expresses a histone-wCherry protein fusion that localizes specifically to the nuclei of intestinal cells. This strain was used in most experiments presented in this Chapter. To study how pulsatile dynamics is modulated by the DAF-2 insulin receptor, we crossed *zIs356*[*Pdaf-16::daf-16a/b-gfp; rol-6*] IV; *stIs10131*[*elt-7p::H1-wCherry + unc-119(+)*] strain into *daf-2(e1368)* or *daf-2(e1370)* strains. Both *e1368* and *e1370* are hypomorphic alleles, but *e1368* contains a substitution of a single amino acid in the ligand-binding domain, while *e1370* (the stronger allele), on the other hand, has a substitution in the kinase domain of the insulin receptor [114]. For DAF-16 single-copy experiments (Section 3.2.6.), we used two endogenous translational fluorescent reporter lines,
daf-16(ot853[daf-16::mNeonGreen::AID])[143] and *uos5[DAF-16::wrmScarlet]*. The construction of the latter, as well as all the crosses were performed by our collaborators, in the lab of María Olmedo (Sevilla).

SAMPLE PREPARATION

Polyacrylamide hydrogels with a micro-chamber array were prepared as described in Chapter 2. For osmotic stress experiments, hydrogels were stored in 200, 300 or 400 mM NaCl solutions for at least one week prior to the experiment. For all experiments except starvation stress, microchambers were filled with *E. coli* bacteria and one *C. elegans* embryo was placed in each chamber, as described in Chapter 2. For starvation experiments, eggs were isolated by bleaching to remove the bacteria and placed one by one inside different microchambers filled with liquid M9 media. For dietary restriction experiments, OP50 bacteria was grown overnight in LB medium and diluted prior to the experiment to achieve a low cell density (4.32×10^8 cells/ml).

TIME-LAPSE MICROSCOPY

To achieve high-throughput analysis of DAF-16 fluorescence in intestinal cells, we performed simultaneous 2-color imaging of DAF-16::GFP and H1::mCherry, a protein fusion that localizes specifically to the nuclei of intestinal cells and thus constitutes a good nuclear marker. Z-stacks with ~ 9 images were collected every 15-minutes for most experiments. Cell synchronization experiments were performed with a 30 second time resolution.

The temperature control system (see Chapter 2) was used to maintain a constant temperature of 20 °C inside the sample. For the heat stress experiments, animals were allowed to hatch at 20 °C, followed by a sudden temperature increase to 31, 32 or 33 °C. It should be noted that there is substantial background autofluorescence from the bacterial lawn, which contributes to the differences in peak amplitude between starvation (no bacteria) and osmotic or heat stress (with bacteria) experiments. Therefore, the absolute values of the peak amplitudes cannot be directly compared.

4.4.2. SEGMENTATION OF INTESTINAL CELLS

Custom Python software was used to calculate DAF-16::GFP fluorescence intensity in the nucleus and cytoplasm of intestinal cells.

We processed the H1-wCherry signal (marker for intestinal nuclei) in order to obtain precise boundaries of cells nuclei. First, at each time point, the z-stack was reduced to the maximum intensity projection, and the worm was segmented from the background using the Otsu method. To speed up computation time, the projected image was cropped to a rectangular region encompassing only the worm, thus removing most background areas. Next, the edges of individual nuclei were detected from the image gradient, which was calculated using the Sobel filter. Finally, a watershed segmentation algorithm was applied to the image gradient to isolate and label the nuclei and to generate a binary mask (see Fig. S4.1B). For each individual nucleus, the focal plane with the maximum average fluorescence intensity was selected as the optimal focal plane.

To obtain the mask for the cytoplasmic region, the nuclear mask was first expanded by dilation and subsequently subtracted from the expanded mask, resulting in a narrow ring surrounding the nucleus (cytoplasmic mask, see Fig. S4.1B). Finally, for each cell the average fluorescence intensity inside the nuclear and cytoplasmic masks was evaluated at the optimal focal plane. To analyze DAF-16::GFP in each cell independently (Fig. 4.6B, Fig. S4.1C), segmented cells were manually annotated. All timelapse movies were carefully inspected by eye and showed no disagreement with DAF-16 localization trajectories obtained by automatic quantification.

4.4.3. DATA ANALYSIS

QUANTIFICATION OF DAF-16 LOCALIZATION AND CONVERSION TO BINARY SEQUENCES

DAF-16::GFP subcellular localization was quantified as the ratio R of average fluorescence intensity in the nucleus to that in the cytoplasm of intestinal cells. Since DAF-16 localization trajectories appeared almost identical in all intestinal cells at a 15-minute time resolution (Fig. S4.1C), they were averaged for the ease of analysis, unless otherwise stated.

To perform quantitative analysis of pulsatile dynamics, we first needed to discriminate nuclear from cytoplasmic localization of DAF-16. Cytoplasmic localization was assigned from the average baseline in $R(t)$ trajectories. Due to high autofluorescence of *E. coli* bacteria in the microchambers, we cannot directly compare DAF-16::GFP signal in animals grown with and without bacteria, and hence a different baseline was computed for each case. For starvation stress (Fig. 4.5A, B), cytoplasmic level $\overline{R}_{\text{starv}}$ was defined as the mean value of the lowest 10 percentile values in $R(t)$ trajectories after hatching, averaged over animals grown in the absence of food at 20 °C. For osmotic stress experiments (Fig. 4.5C, D), the cytoplasmic level $\overline{R}_{\text{osm}}$ was defined as the mean value of $R(t)$ trajectories after hatching, averaged over all animals in the control condition (20 °C *ad libitum* food in the absence of stress). For heat stress (Fig.

4.5E, F), the cytoplasmic level $\overline{R}_{\text{temp}}$ was instead calculated using the new baseline after the onset of stress (as described in the next section). Next, thresholds R^*_{starv}, R^*_{osm} and R^*_{temp} were obtained by multiplying the baseline values $\overline{R}_{\text{starv}}$, $\overline{R}_{\text{osm}}$ and $\overline{R}_{\text{temp}}$ respectively by a fixed factor of 1.05. Finally, values above the corresponding threshold were classified as nuclear localization, thus generating a binary sequence of nuclear to cytoplasmic localization from $R(t)$ trajectories (Fig. 4.5A-F, lower panels).

ANALYSIS OF PULSE CHARACTERISTICS

DAF-16 pulses under osmotic stress were characterized by their duration and amplitude (Fig. 4.4G, H). For each pulse, duration was defined as the time the $R(t)$ value was uninterruptedly above the threshold R^*_{osm}. Pulse amplitude was defined as the maximum $R(t)$ value within the pulse. To limit artifacts, only pulses that lasted longer than a single time-point were taken into account.

The amplitude of the initial nuclear peak upon heat stress (Fig. 4.4I) was characterized by finding the maximum $R(t)$ value within 3 hours after the onset of heat stress. The subsequent baseline (Fig. 4.4J) was calculated as the average value of the lowest 50th percentile values in $R(t)$ trajectories within 3 hours after the onset of heat stress.

AUTOCORRELATION ANALYSIS

Pulse periodicity was assessed with auto-correlation analysis. We compared each trace with itself after introducing a varying lag time. For each lag time we calculated the Pearson correlation coefficient and obtained the curves shown in Fig. 4.3D and Fig. S4.6. We next fitted the curves to the function:

$$Ae^{-\tau/\lambda}\sin\left(\frac{\tau}{2\pi T}+\phi\right)+B+C\tau+D\tau^2+E\tau^3$$

Which includes an exponential term to account for damping, a polynomial term to account for shifts and drifts in the signal, and an oscillatory term that provides the period of oscillations. Only the periods from traces whose characteristics were clearly oscillatory and whose fit was visibly successful were considered for calculating the pulsing periodicity (Fig. S4.6), while all the curves were used to compute the averaged auto-correlation function (Fig. 4.3E).

VARIABILITY ANALYSIS (FRACTION OF TIME SPENT IN THE NUCLEUS)

To better characterize the inter-individual variability in DAF-16 localization dynamics at different stresses, we calculated ϕ_N, the fraction of time DAF-16 has spent in the nucleus since the onset of stress. First, DAF-16 localization was classified as cytoplasmic or nuclear using a set $R(t)$ threshold (Fig. 4.5A-F, dashed line), and localization traces were converted into binary sequences (Fig. 4.5A-F, bottom panels). After any period of time ΔT, the total amount of time spent in the nucleus T_N is the sum of all time points $(t_{N,i})$ for which DAF-16 localization was classified as nuclear, i.e. $T_N = \sum_{i=0}^{\Delta T} t_{N,i}$. The fraction of time spent in the nucleus ϕ_N (Fig. 4.5G-I) was hence computed as T_N divided by ΔT. For each time point, the value of ϕ_N is then a measure of the past history (how much time has DAF-16 spent in the nucleus up to that time point).

MODEL-INDEPENDENT MONTE CARLO SIMULATION FOR DETERMINING INTERCELL LAG TIME UNCERTAINTIES

To detect potential cell-to-cell delays in DAF-16 translocation dynamics, we computed cell-pair cross-correlations and quantified the lag time as the position of the distribution maximum (Fig. 4.6C)[154]. The peak position is subject to uncertainties due to the propagation of measurement error, intrinsic cellular noise, and a finite sampling rate. Large uncertainties in the peak position challenge the fact that any observed lag is 'real', i.e. whether a non-zero lag is statistically significant. Uncertainties in the cross-correlation lag times were calculated using a model-independent Monte Carlo simulation [155]. First, a random set of N points was selected from the original time series data (also consisting of N points per measurement), regardless of whether any point was previously chosen. Points that were selected multiple times were then adjusted so that they are only included once, reducing the final size of the set. The temporal order of the sampled points was retained by re-ordering them after the random selection. The set was generated for the time series of two different cells, i.e. the same time points were selected for both signals, which were then cross-correlated (Fig. S4.8A). Values above $0.8 \cdot r_{\max}$ (where $r$max is the maximum value of the cross-correlation curve) were used to calculate the centroid of the peak [155]. This procedure was iterated 1000 times, and a histogram of centroid lag times was constructed (Fig. S4.8B). The mean of the distribution was used as the delay between any given pair of cells, and the 95% confidence interval (corresponding to two standard deviations in a normal distribution) as its error. If the confidence interval for any given cell-pair lag time included the value zero, the DAF-16 dynamics delay between the cells was considered not significant.
As a control, again N data points were randomly extracted from the time series, but not temporally re-ordered, and signals were cross-correlated (Fig. S4.8C). The peak position histogram after 1000 iterations displayed a sharp peak at zero (Fig. S4.8D), which confirms that the observed delays are not an artifact from the data.

4.4.4. HUMAN CELLS EXPERIMENTAL METHODS

All experiments with human cells were performed by our collaborator, María Antonia Sánchez-Romero from the University of Sevilla.

CONSTRUCTION OF GFP-FOXO3A PLASMID

A human FOXO3a cDNA was cloned into pEGFP-C1 (Clontech Laboratories) to generate the GFP-FOXO3A plasmid.

HUMAN EPITHELIAL CELLS USED IN THIS STUDY

U20S human epithelial cells (H2B-RFP7 Hygroo-1, a gift from Dr. Israel Salguero, a member of Dr. Steve Jackson's laboratory) were grown in in Dulbecco's modified

Eagle medium (DMEM) supplemented with 10% fetal calf serum (FBS) and 2 mM L-glutamine (Sigma-Aldrich). Cells were maintained in a 5% CO_2 humidified atmosphere at 37 °C. U20S cells were transiently transfected with GFP-FOXO3a expression plasmid.

TRANSIENT TRANSFECTION OF HUMAN EPITHELIAL CELLS

U2OS cells were transfected by electroporation using the GFP-FOXO3a expression plasmid. Briefly, approximately 107 cells were trypsinized, washed with cold PBS, and then resuspended in 200 μl of DMEM supplemented with 15 mM HEPES pH 7.4. 6 μg of plasmid DNA was mixed with H_2O and NaCl (final concentration of 200 mM) in 50 μl of final volume, and added to the cell suspension. The cell–DNA mixture was then incubated on ice for 10 min and electroporated using a Gene Pulser Xcell (BioRad) at a setting of 950 μF, 720 Σ and 240 V in 0.4-cm transfection cuvettes. Cells were incubated on ice for an additional 10 min, diluted 1:20 in DMEM supplemented with 10% FBS, and seeded into μ-slide 8 well plates (Ibidi). Transfected human cells were incubated at 37 °C with 5% CO_2. After 24 hours of incubation, cells were washed twice with phosphate buffered saline (PBS) to eliminate debris of cells, and incubated in fresh DMEM medium without red phenol and supplemented with 2 mM L-glutamine (Sigma-Aldrich).

ASSAY IN U20S EPITHELIAL CELLS

Transfected U2OS epithelial cells were seeded in 8-well plates (Ibidi) the day before the assay. 24 hours after electroporation transfections, cells were washed twice with PBS and incubated in a fresh medium without phenol red and supplemented with 2 mM glutamine (Sigma-Aldrich). Different amount of FBS were added to the fresh medium when the effect of FBS was analyzed. After 15 minutes, 8-well plates containing epithelial cells expressing GFP-FOXO3a were placed in a fluorescence microscope equipped with an incubation system and images were captured.

FLUORESCENCE MICROSCOPY

Images were captured with a Zeiss Apotome fluorescence microscope equipped with a 10x Plan Apochromat objective and an incubation system that covers every requirement in the cultivation and observation of living cells (37 °C; 5% CO_2). Pictures were taken at different times using an Axiocam 506 camera, and the images were analyzed using ImageJ software (Wayne Rasband, Research Services Branch, National Institute of Mental Health, MD, USA).

4.5. SUPPLEMENTARY FIGURES

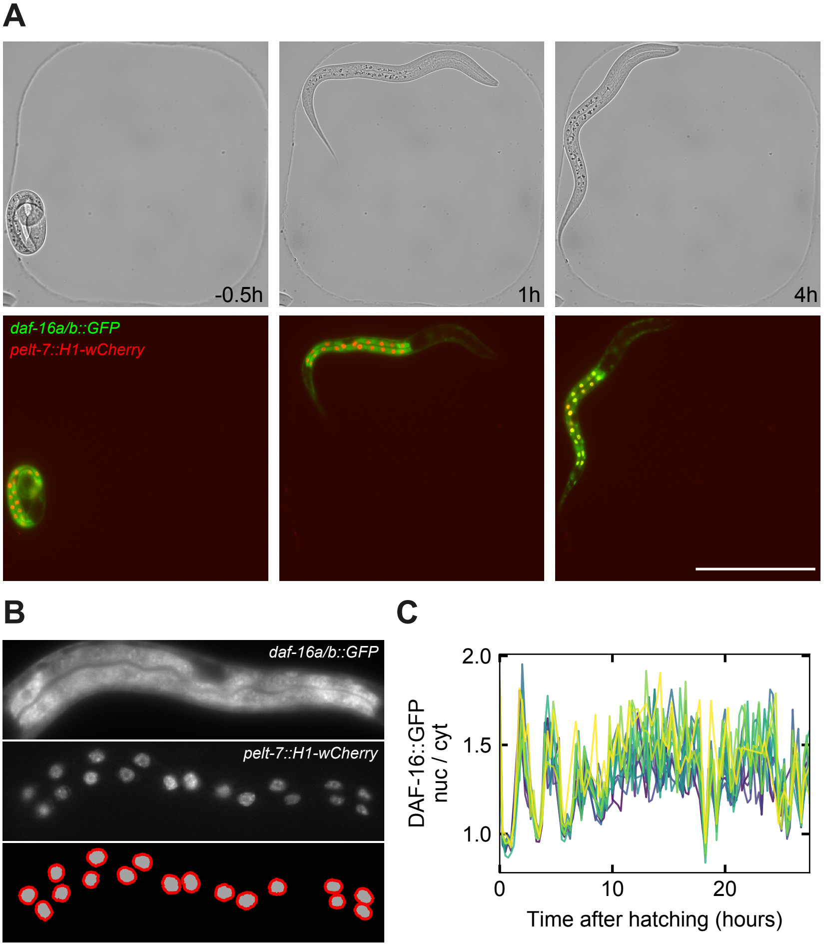

Figure S4.1: Automated quantification of DAF-16 pulse dynamics. **(A)** Single animal constrained in a microchamber without food. Scale bar is 100 μm, time is relative to hatching, **(B)** Fluorescence images of DAF-16::GFP (top panel) and intestinal marker H1-wCherry (middle panel) in the intestinal cells of L1 larva. Bottom panel shows the binary mask of the nuclei (gray) and cytoplasm (red) of the intestinal cells, **(C)** DAF-16::GFP subcellular localization calculated as the ratio of average fluorescence intensity in the nuclei and the cytoplasm of individual intestinal cells.

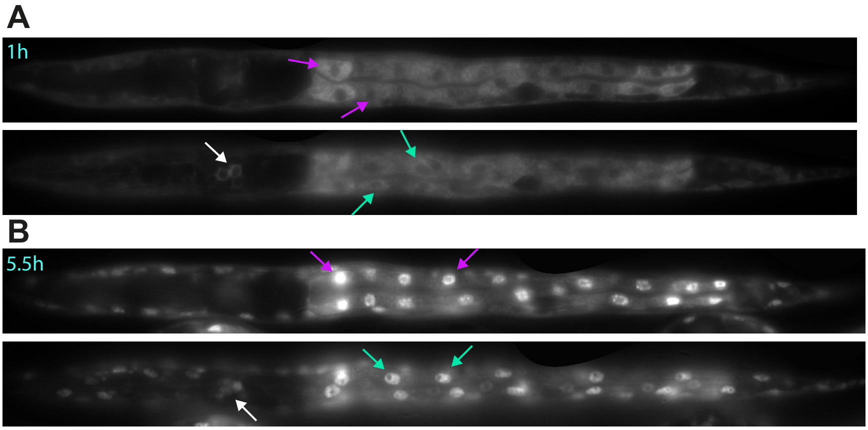

Figure S4.2: Fluorescent images of DAF-16::GFP in L1 larva subject to starvation at **(A)** 1 h and **(B)** 5.5 h after hatching. Upper and lower panels are different focal planes. Arrows mark some intestinal cells (magenta), hypodermal cells (cyan) and head neurons (white). DAF-16 is localized to the cytoplasm (A) and to the nucleus (B) in all cells, which shows that pulsing is synchronized between different types of cells along the animal body. Images correspond to the same animal as in Fig. 4.1B-E.

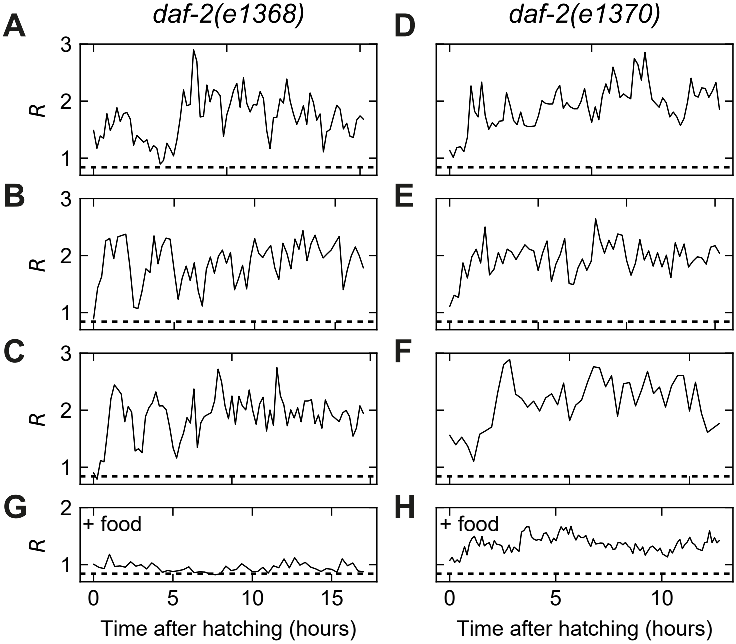

Figure S4.3: DAF-16 pulsatile dynamics in different daf-2 alleles. DAF-16 localization trajectories $R(t)$ in the intestinal cells of single *daf-2(e1368)* or *daf-2(e1370)* larvae. *daf-2(e1368)* mutation affects the conformation of the extracellular domain of the insulin receptor and partially impairs its proper activation, while *daf-2(e1370)* disrupts receptor's kinase activity. **(A-C)** In *daf-2(e1368)* animals subject to starvation stress, one or two DAF-16 nuclear pulses are observed in the first ~ 5 hours after hatching, followed by nearly constant nuclear localization. **(D-F)** *daf-2(e1370)* animals subject to starvation stress exhibit constant nuclear DAF-16 localization. **(G)** In the presence of food (i.e. no stress), DAF-16 nuclear concentration in *daf-2(e1368)* animals is marginally higher than in wild-type (dashed line). **(H)** In contrast, *daf-2(e1370)* animals exhibit clear nuclear localization. Overall, these data show that *daf-2(e1370)* mutation results in stronger DAF-16 activation, compared to *daf-2(e1368)*, both under starvation and in the presence of food. The traces correspond to the average signal in the Int1 cells and were analyzed manually.

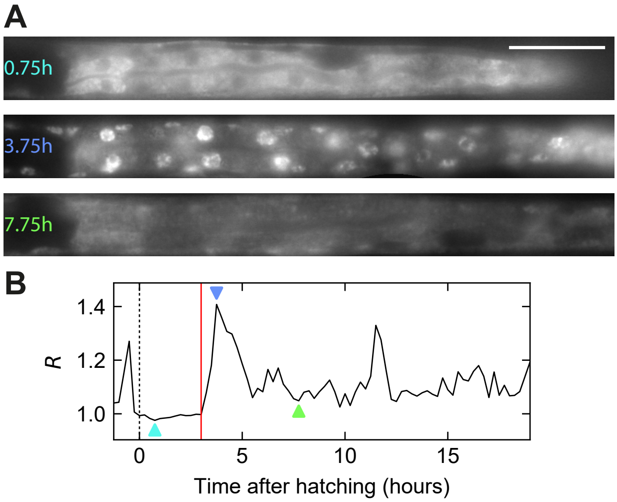

Figure S4.4: DAF-16 dynamics under heat stress. (A) Fluorescence images of DAF-16::GFP in the intestinal cells of L1 larva before and after the onset of heat stress (32 °C), corresponding to the arrowheads in panel (B). Scale bar is 20 μm. Images were computationally straightened (details in Chapter 2). **(B)** DAF-16::GFP localization trajectory R in larva grown in abundance of *E. coli* bacteria at 20 °C, followed by a shift in temperature to 32 °C (red line).

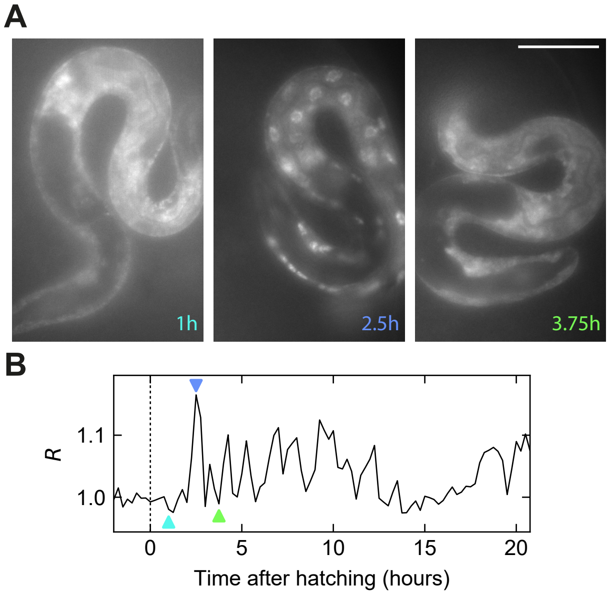

Figure S4.5: DAF-16 dynamics under osmotic stress. (A) Fluorescence images of DAF-16::GFP in the intestinal cells of L1 larva subject to osmotic stress (300 mM NaCl), corresponding to the arrowheads in panel (B). Scale bar is 20 μm. **(B)** DAF-16::GFP localization trajectory R in larva grown in abundance of *E. coli* bacteria at 20 °C, in the micro-chambers that were stored in 300 mM NaCl solution prior to the experiment.

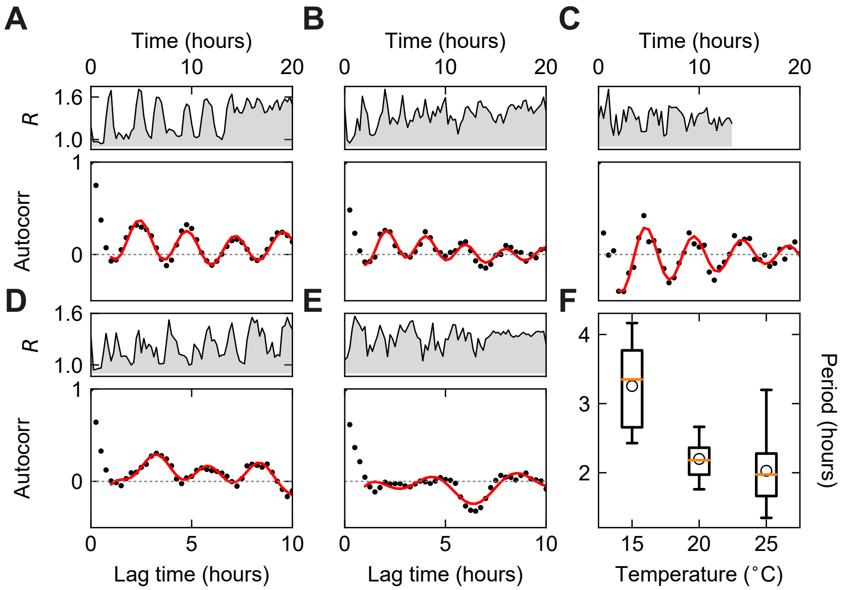

Figure S4.6: Quantification of the period of DAF-16 pulses during starvation. (A-E) DAF-16::GFP localization trajectories *R* (upper panels) and the corresponding auto-correlation functions (lower panels). Red line is a fit to the data (see Methods). Only periods from fits that showed clear oscillations were considered (9/17). For example, panel E was discarded as the auto-correlation does not display clear oscillations. (*F*) Period of DAF-16::GFP oscillations during starvation stress at 15, 20 and 25 °C. Period decreases with temperature and is 3.3 ± 0.6, 2.2 ± 0.3, 2.0 ± 0.5 hours, respectively ($n_{15} = 9$, $n_{20} = 9$, $n_{25} = 13$).

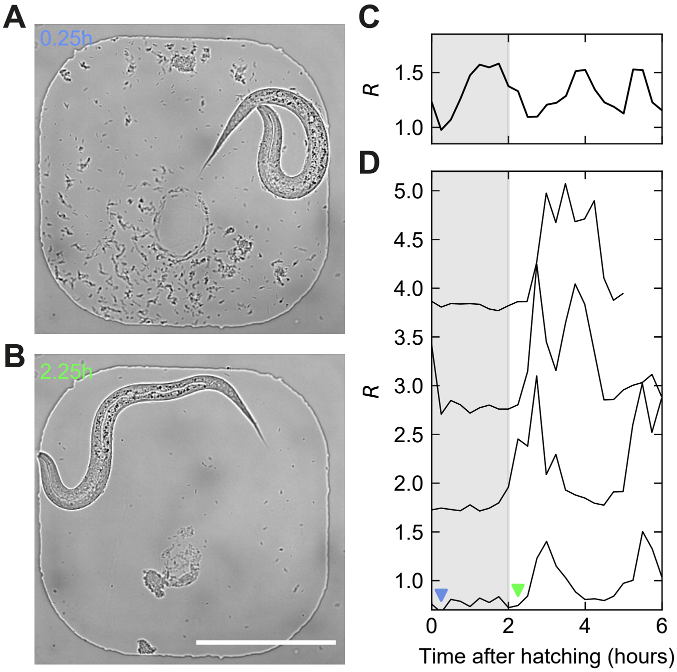

Figure S4.7: DAF-16 pulses only occur under complete lack of food. **(A, B)** Transmitted light images of L1 larva grown at low *E. coli* concentration (4.32×10^8 cells/ml) at 20 °C, immediately after hatching **(A)** and 2 hours after hatching **(B)**. Scale bar is 100 μm. **(C)** DAF-16::GFP localization trajectory R in L1 larva grown in the absence of *E. coli* bacteria at 20 °C (prepared by bleaching, see Methods). The first nuclear pulse occurs within minutes after hatching (see also Fig. 4.1D). **(D)** DAF-16::GFP localization trajectories R in four different L1 larvae grown at low *E. coli* concentration (4.3×10^8 cells/ml) at 20 °C. The first nuclear pulse takes place after 2 hours, once there is almost no food available in the chamber. Arrowheads correspond to images in (A) and (B). For visualization, traces were shifted by 0, 1, 2 and 3 in R, respectively.

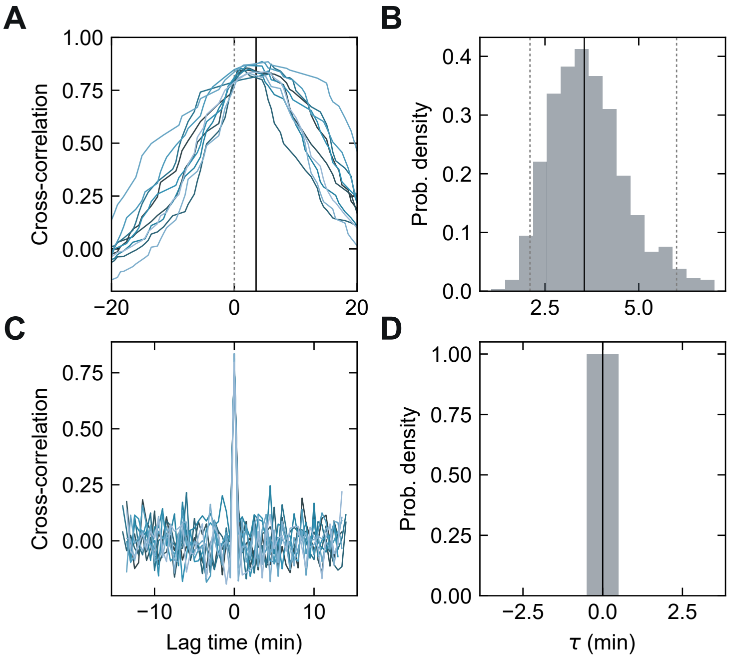

Figure S4.8: Uncertainty estimation of delay between cells using Monte Carlo simulations. **(A)** Cross-correlations of DAF-16 localization trajectories between Int2V and Int8R cells. The 10 different curves are generated from 10 different subsets randomly sampled from a single worm using Monte Carlo simulations. The average peak position or delay (τ, solid black line) clearly differs from 0 (dashed gray line). **(B)** Distribution of peak positions or delays for 1000 cross-correlation random subsets. **(C)** Cross-correlations of scrambled DAF-16 localization trajectories (see Methods), between Int2V and Int8R. **(D)** Distribution of peak positions or delays for 1000 cross-correlation subsets of scrambled trajectories. For the scrambled data there is no delay, which indicates that the delay observed between cells with unshuffled data is not an artifact.

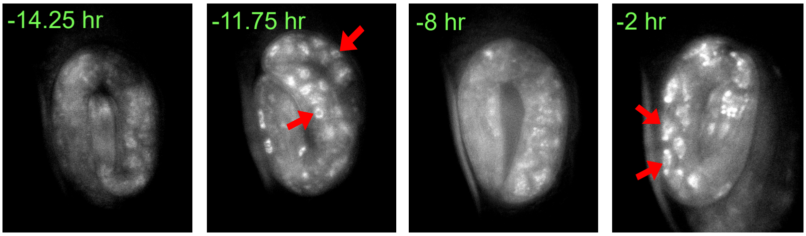

A

Focus on intestinal cells

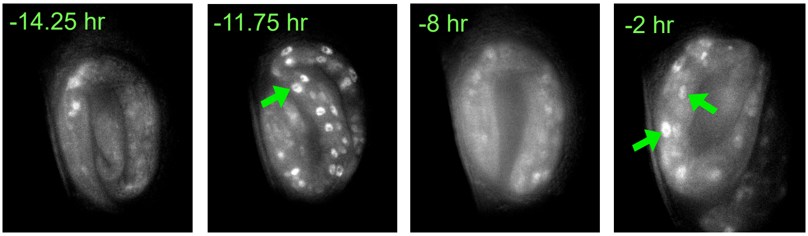

B

Focus on hypodermal cells

Figure S4.9: DAF-16 pulsatile dynamics in an endogenously tagged strain. Fluorescent images of DAF-16::mNeonGreen (endogenously tagged) strain focusing on **(A)** intestinal cells and **(B)** hypodermal cells in an embryo subject to osmotic stress (400 mM NaCl). Time from hatching. DAF-16 is mostly localized to the cytoplasm (first and third panels) and to the nucleus (second and fourth panels).

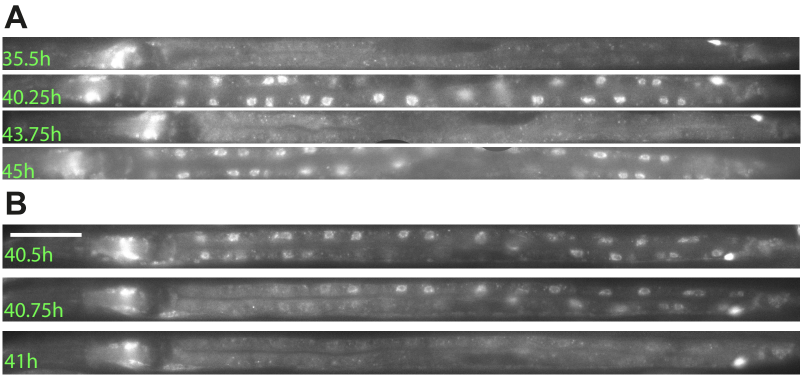

Figure S4.10: DAF-16::wScarlet pulsatile dynamics in the single-copy strain. Fluorescence images show DAF-16::wrmScarlet subcellular localization in the intestinal cells of L3 larva, grown in the small 190 × 190 × 10 μm microchambers filled with *E. coli* bacteria. **(A)** Pulsing of DAF-16::wrmScarlet is observed when food becomes scarce and the growing larvae becomes visibly compressed inside the small microchamber. **(B)** Transition from nuclear to cytoplasmic DAF-16::wrmScarlet localization reveals order in intestinal cells (at 40.75 hours DAF-16::wrmScarlet is still localized to the nucleus in posterior, but not in anterior cells). Scale bar is 50 μm.

BIBLIOGRAPHY

[1] J. C. Dunlap, *Molecular bases for circadian clocks,* Cell **96**, 271 (1999).

[2] R. S. Edgar, E. W. Green, Y. Zhao, G. Van Ooijen, M. Olmedo, X. Qin, Y. Xu, M. Pan, U. K. Valekunja, K. A. Feeney, *et al.*, *Peroxiredoxins are conserved markers of circadian rhythms,* Nature **485**, 459 (2012).

[3] M. Ebisuya and J. Briscoe, *What does time mean in development?* Development **145** (2018).

[4] O. Pourquié, *The segmentation clock: converting embryonic time into spatial pattern,* Science **301**, 328 (2003).

[5] C. Gomez, E. M. Özbudak, J. Wunderlich, D. Baumann, J. Lewis, and O. Pourquié, *Control of segment number in vertebrate embryos,* Nature **454**, 335 (2008).

[6] Y. Tanaka, J. Yoshimura, C. Simon, J. R. Cooley, and K.-i. Tainaka, *Allee effect in the selection for prime-numbered cycles in periodical cicadas,* Proceedings of the National Academy of Sciences **106**, 8975 (2009).

[7] M. R. Palmert and P. A. Boepple, *Variation in the timing of puberty: clinical spectrum and genetic investigation,* The Journal of Clinical Endocrinology & Metabolism **86**, 2364 (2001).

[8] A.-S. Parent, G. Rasier, A. Gerard, S. Heger, C. Roth, C. Mastronardi, H. Jung, S. R. Ojeda, and J.-P. Bourguignon, *Early onset of puberty: tracking genetic and environmental factors,* Hormone Research in Paediatrics **64**, 41 (2005).

[9] L. H. Hartwell and T. A. Weinert, *Checkpoints: controls that ensure the order of cell cycle events,* Science **246**, 629 (1989).

[10] K. F. Rewitz, N. Yamanaka, and M. B. O'Connor, *Developmental checkpoints and feedback circuits time insect maturation,* in *Current topics in developmental biology,* Vol. 103 (Elsevier, 2013) pp. 1–33.

[11] B. A. Kinney, A. Al Anber, R. H. Row, Y.-J. Tseng, M. D. Weidmann, H. Knaut, and B. L. Martin, *Sox2 and canonical wnt signaling interact to activate a developmental checkpoint coordinating morphogenesis with mesoderm fate acquisition,* Cell reports **33**, 108311 (2020).

[12] A. J. Schindler, L. R. Baugh, and D. R. Sherwood, *Identification of late larval stage developmental checkpoints in caenorhabditis elegans regulated by insulin/igf and steroid hormone signaling pathways,* PLoS Genet **10**, e1004426 (2014).

[13] M. M. Albarqi, J. D. Stoltzfus, A. A. Pilgrim, T. J. Nolan, Z. Wang, S. A. Kliewer, D. J. Mangelsdorf, and J. B. Lok, *Regulation of life cycle checkpoints and developmental activation of infective larvae in strongyloides stercoralis by dafachronic acid,* PLoS pathogens **12**, e1005358 (2016).

[14] T. Yamada, K.-i. Hironaka, O. Habara, Y. Morishita, and T. Nishimura, *A developmental checkpoint directs metabolic remodelling as a strategy against starvation in drosophila,* Nature Metabolism **2**, 1096 (2020).

[15] L. Lopez-Molina, S. Mongrand, and N.-H. Chua, *A postgermination developmental arrest checkpoint is mediated by abscisic acid and requires the abi5 transcription factor in arabidopsis,* Proceedings of the National Academy of Sciences **98**, 4782 (2001).

[16] A. A. Teleman, *Molecular mechanisms of metabolic regulation by insulin in drosophila,* Biochemical Journal **425**, 13 (2010).

[17] J. M. Raser and E. K. O'shea, *Noise in gene expression: origins, consequences, and control,* Science **309**, 2010 (2005).

[18] A. Eldar and M. B. Elowitz, *Functional roles for noise in genetic circuits,* Nature **467**, 167 (2010).

[19] E. Korobkova, T. Emonet, J. M. Vilar, T. S. Shimizu, and P. Cluzel, *From molecular noise to behavioural variability in a single bacterium,* Nature **428**, 574 (2004).

[20] L. Cai, C. K. Dalal, and M. B. Elowitz, *Frequency-modulated nuclear localization bursts coordinate gene regulation,* Nature **455**, 485 (2008).

[21] S. Brenner, *The genetics of caenorhabditis elegans,* Genetics **77**, 71 (1974).

[22] O. Hobert, *Behavioral plasticity in c. elegans: paradigms, circuits, genes,* Journal of neurobiology **54**, 203 (2003).

[23] A. D. Chalmers, P. Whitley, A. Noatynska, and M. Gotta, *Cell polarity and asymmetric cell division: the c. elegans early embryo,* Essays in biochemistry **53**, 1 (2012).

[24] H. A. Tissenbaum, *Using c. elegans for aging research,* Invertebrate reproduction & development **59**, 59 (2015).

[25] H. M. Ellis, H. R. Horvitz, *et al.*, *Genetic control of programmed cell death in the nematode c. elegans,* Cell **44**, 817 (1986).

[26] R. C. Lee, R. L. Feinbaum, and V. Ambros, *The c. elegans heterochronic gene lin-4 encodes small rnas with antisense complementarity to lin-14,* cell **75**, 843 (1993).

[27] A. Fire, S. Xu, M. K. Montgomery, S. A. Kostas, S. E. Driver, and C. C. Mello, *Potent and specific genetic interference by double-stranded rna in caenorhabditis elegans,* nature **391**, 806 (1998).

[28] C. elegans Sequencing Consortium*, *Genome sequence of the nematode c. elegans: a platform for investigating biology,* Science **282**, 2012 (1998).

[29] T. Kaletta and M. O. Hengartner, *Finding function in novel targets: C. elegans as a model organism,* Nature reviews Drug discovery **5**, 387 (2006).

[30] J. E. Sulston and H. R. Horvitz, *Post-embryonic cell lineages of the nematode, caenorhabditis elegans,* Developmental biology **56**, 110 (1977).

[31] J. Kimble and D. Hirsh, *The postembryonic cell lineages of the hermaphrodite and male gonads in caenorhabditis elegans,* Developmental biology **70**, 396 (1979).

[32] G. C. Monsalve and A. R. Frand, *Toward a unified model of developmental timing: A "molting" approach,* in *Worm*, Vol. 1 (Taylor & Francis, 2012) pp. 221–230.

[33] G.-J. Hendriks, D. Gaidatzis, F. Aeschimann, and H. Großhans, *Extensive oscillatory gene expression during C. elegans larval development,* Molecular cell **53**, 380 (2014).

[34] D. hyun Kim, D. Grün, and A. van Oudenaarden, *Dampening of expression oscillations by synchronous regulation of a microrna and its target,* Nature genetics **45**, 1337 (2013).

[35] M. W. Meeuse, Y. P. Hauser, L. J. Morales Moya, G.-J. Hendriks, J. Eglinger, G. Bogaarts, C. Tsiairis, and H. Großhans, *Developmental function and state transitions of a gene expression oscillator in caenorhabditis elegans,* Molecular systems biology **16**, e9498 (2020).

[36] A. E. Rougvie, *Control of developmental timing in animals,* Nature Reviews Genetics **2**, 690 (2001).

[37] E. G. Moss, *Heterochronic genes and the nature of developmental time,* Current Biology **17**, R425 (2007).

[38] A. E. Rougvie and E. G. Moss, *Developmental transitions in C. elegans larval stages,* in *Current topics in developmental biology*, Vol. 105 (Elsevier, 2013) pp. 153–180.

[39] K. A. McCulloch and A. E. Rougvie, *Caenorhabditis elegans period homolog lin-42 regulates the timing of heterochronic mirna expression,* Proceedings of the National Academy of Sciences **111**, 15450 (2014).

[40] P. M. Van Wynsberghe, E. F. Finnegan, T. Stark, E. P. Angelus, K. E. Homan, G. W. Yeo, and A. E. Pasquinelli, *The period protein homolog lin-42 negatively regulates microrna biogenesis in C. elegans,* Developmental biology **390**, 126 (2014).

[41] R. Perales, D. M. King, C. Aguirre-Chen, and C. M. Hammell, *Lin-42, the Caenorhabditis elegans period homolog, negatively regulates microrna transcription,* PLoS genetics **10** (2014).

[42] G. C. Monsalve, C. Van Buskirk, and A. R. Frand, *Lin-42/period controls cyclical and developmental progression of C. elegans molts,* Current Biology **21**, 2033 (2011).

[43] S. Uppaluri and C. P. Brangwynne, *A size threshold governs Caenorhabditis elegans developmental progression,* Proceedings of the Royal Society B: Biological Sciences **282**, 20151283 (2015).

[44] R. C. Cassada and R. L. Russell, *The dauerlarva, a post-embryonic developmental variant of the nematode caenorhabditis elegans,* Developmental biology **46**, 326 (1975).

[45] P. J. Hu, *Dauer,* in *WormBook: The Online Review of C. elegans Biology [Internet]* (WormBook, 2018).

[46] L. R. Baugh and P. W. Sternberg, *Daf-16/foxo regulates transcription of cki-1/cip/kip and repression of lin-4 during C. elegans l1 arrest,* Current Biology **16**, 780 (2006).

[47] C. T. Murphy and P. J. Hu, *Insulin/insulin-like growth factor signaling in C. elegans,* in *WormBook: The Online Review of C. elegans Biology* (WormBook, 2018).

[48] N. Gritti, S. Kienle, O. Filina, and J. S. Van Zon, *Long-term time-lapse microscopy of C. elegans post-embryonic development,* Nature communications **7**, 1 (2016).

[49] P. J. Keller, A. D. Schmidt, A. Santella, K. Khairy, Z. Bao, J. Wittbrodt, and E. H. Stelzer, *Fast, high-contrast imaging of animal development with scanned light sheet–based structured-illumination microscopy,* Nature methods **7**, 637 (2010).

[50] J. E. Sulston, E. Schierenberg, J. G. White, J. N. Thomson, *et al.*, *The embryonic cell lineage of the nematode caenorhabditis elegans,* Developmental biology **100**, 64 (1983).

[51] Z. Bao, J. I. Murray, T. Boyle, S. L. Ooi, M. J. Sandel, and R. H. Waterston, *Automated cell lineage tracing in caenorhabditis elegans,* proceedings of the National Academy of Sciences **103**, 2707 (2006).

[52] Y. Wu, A. Ghitani, R. Christensen, A. Santella, Z. Du, G. Rondeau, Z. Bao, D. Colón-Ramos, and H. Shroff, *Inverted selective plane illumination microscopy (ispim) enables coupled cell identity lineaging and neurodevelopmental imaging in caenorhabditis elegans,* Proceedings of the National Academy of Sciences **108**, 17708 (2011).

[53] N. Fielenbach and A. Antebi, *C. elegans dauer formation and the molecular basis of plasticity,* Genes & development **22**, 2149 (2008).

[54] L. R. Baugh, *To grow or not to grow: nutritional control of development during caenorhabditis elegans l1 arrest,* Genetics **194**, 539 (2013).

[55] E. Watson and A. J. Walhout, *Caenorhabditis elegans metabolic gene regulatory networks govern the cellular economy,* Trends in Endocrinology & Metabolism **25**, 502 (2014).

[56] Y. Chai, W. Li, G. Feng, Y. Yang, X. Wang, and G. Ou, *Live imaging of cellular dynamics during caenorhabditis elegans postembryonic development,* Nature protocols **7**, 2090 (2012).

[57] E. Kim, L. Sun, C. V. Gabel, and C. Fang-Yen, *Long-term imaging of caenorhabditis elegans using nanoparticle-mediated immobilization,* PloS one **8**, e53419 (2013).

[58] S. X. Guo, F. Bourgeois, T. Chokshi, N. J. Durr, M. A. Hilliard, N. Chronis, and A. Ben-Yakar, *Femtosecond laser nanoaxotomy lab-on-a-chip for in vivo nerve regeneration studies,* Nature methods **5**, 531 (2008).

[59] S. E. Hulme, S. S. Shevkoplyas, J. Apfeld, W. Fontana, and G. M. Whitesides, *A microfabricated array of clamps for immobilizing and imaging c. elegans,* Lab on a Chip **7**, 1515 (2007).

[60] C. B. Rohde, F. Zeng, R. Gonzalez-Rubio, M. Angel, and M. F. Yanik, *Microfluidic system for on-chip high-throughput whole-animal sorting and screening at subcellular resolution,* Proceedings of the National Academy of Sciences **104**, 13891 (2007).

[61] R. B. Kopito and E. Levine, *Durable spatiotemporal surveillance of caenorhabditis elegans response to environmental cues,* Lab on a Chip **14**, 764 (2014).

[62] K. Chung, M. M. Crane, and H. Lu, *Automated on-chip rapid microscopy, phenotyping and sorting of c. elegans,* Nature methods **5**, 637 (2008).

[63] T. V. Chokshi, A. Ben-Yakar, and N. Chronis, *Co 2 and compressive immobilization of c. elegans on-chip,* Lab on a Chip **9**, 151 (2009).

[64] H. Hwang, J. Krajniak, Y. Matsunaga, G. M. Benian, and H. Lu, *On-demand optical immobilization of caenorhabditis elegans for high-resolution imaging and microinjection,* Lab on a Chip **14**, 3498 (2014).

[65] Z. Pincus, T. Smith-Vikos, and F. J. Slack, *Microrna predictors of longevity in caenorhabditis elegans,* PLoS Genet **7**, e1002306 (2011).

[66] C.-C. J. Yu, D. M. Raizen, and C. Fang-Yen, *Multi-well imaging of development and behavior in caenorhabditis elegans,* Journal of neuroscience methods **223**, 35 (2014).

[67] H. Bringmann, *Agarose hydrogel microcompartments for imaging sleep-and wake-like behavior and nervous system development in caenorhabditis elegans larvae,* Journal of neuroscience methods **201**, 78 (2011).

[68] P. Nghe, S. Boulineau, S. Gude, P. Recouvreux, J. S. van Zon, and S. J. Tans, *Microfabricated polyacrylamide devices for the controlled culture of growing cells and developing organisms,* PloS one **8**, e75537 (2013).

[69] L. Byerly, R. Cassada, and R. Russell, *The life cycle of the nematode caenorhabditis elegans: I. wild-type growth and reproduction,* Developmental biology **51**, 23 (1976).

[70] H. R. Horvitz and J. E. Sulston, *Isolation and genetic characterization of cell-lineage mutants of the nematode caenorhabditis elegans,* Genetics **96**, 435 (1980).

[71] R. M. Terns, P. Kroll-Conner, J. Zhu, S. Chung, and J. H. Rothman, *A deficiency screen for zygotic loci required for establishment and patterning of the epidermis in caenorhabditis elegans,* Genetics **146**, 185 (1997).

[72] A. R. Frand, S. Russel, and G. Ruvkun, *Functional genomic analysis of C. elegans molting,* PLoS biology **3** (2005).

[73] G. Aspöck, H. Kagoshima, G. Niklaus, and T. R. Bürglin, *Caenorhabditis elegans has scores of hedgehogrelated genes: sequence and expression analysis,* Genome Research **9**, 909 (1999).

[74] M. Wildwater, N. Sander, G. de Vreede, and S. van den Heuvel, *Cell shape and wnt signaling redundantly control the division axis of C. elegans epithelial stem cells,* Development **138**, 4375 (2011).

[75] R. Singh and J. Sulston, *Some observations on moulting in caenorhabditis elegans,* Nematologica **24**, 63 (1978).

[76] R. Kamath, M. Martinez-Campos, P. Zipperlen, A. Fraser, and J. Ahringer, *Effectiveness of specific rna-mediated interference through ingested double-stranded rna in c. elegans,* Genome Biol **2** (2001).

[77] D. Ben-Zvi, B.-Z. Shilo, A. Fainsod, and N. Barkai, *Scaling of the bmp activation gradient in xenopus embryos,* Nature **453**, 1205 (2008).

[78] T. Gregor, W. Bialek, R. R. D. R. Van Steveninck, D. W. Tank, and E. F. Wieschaus, *Diffusion and scaling during early embryonic pattern formation,* Proceedings of the National Academy of Sciences **102**, 18403 (2005).

[79] B. Houchmandzadeh, E. Wieschaus, and S. Leibler, *Establishment of developmental precision and proportions in the early drosophila embryo,* Nature **415**, 798 (2002).

[80] D. M. Umulis and H. G. Othmer, *Mechanisms of scaling in pattern formation,* Development **140**, 4830 (2013).

[81] W. Driever and C. Nüsslein-Volhard, *A gradient of bicoid protein in drosophila embryos,* Cell **54**, 83 (1988).

[82] W. Driever and C. N sslein Volhard, *The bicoid protein determines position in the drosophila embryo in a concentration-dependent manner,* Cell **54**, 95 (1988).

[83] L. Rensing, U. Meyer-Grahle, and P. Ruoff, *Biological timing and the clock metaphor: oscillatory and hourglass mechanisms,* Chronobiology international **18**, 329 (2001).

[84] E. G. Moss, R. C. Lee, and V. Ambros, *The cold shock domain protein lin-28 controls developmental timing in c. elegans and is regulated by the lin-4 rna,* Cell **88**, 637 (1997).

[85] G. Ruvkun and J. Giusto, *The caenorhabditis elegans heterochronic gene lin-14 encodes a nuclear protein that forms a temporal developmental switch,* Nature **338**, 313 (1989).

[86] V. Ambros and H. R. Horvitz, *Heterochronic mutants of the nematode Caenorhabditis elegans,* Science **226**, 409 (1984).

[87] M. Jeon, H. F. Gardner, E. A. Miller, J. Deshler, and A. E. Rougvie, *Similarity of the C. elegans developmental timing protein lin-42 to circadian rhythm proteins,* Science **286**, 1141 (1999).

[88] L. Avery and B. B. Shtonda, *Food transport in the c. elegans pharynx,* Journal of Experimental Biology **206**, 2441 (2003).

[89] L. T. MacNeil, E. Watson, H. E. Arda, L. J. Zhu, and A. J. Walhout, *Diet-induced developmental acceleration independent of tor and insulin in c. elegans,* Cell **153**, 240 (2013).

[90] A. A. Soukas, E. A. Kane, C. E. Carr, J. A. Melo, and G. Ruvkun, *Rictor/torc2 regulates fat metabolism, feeding, growth, and life span in caenorhabditis elegans,* Genes & development **23**, 496 (2009).

[91] D. M. Raizen, R. Lee, and L. Avery, *Interacting genes required for pharyngeal excitation by motor neuron mc in caenorhabditis elegans.* Genetics **141**, 1365 (1995).

[92] T. L. Edelman, K. A. McCulloch, A. Barr, C. Frøkjær-Jensen, E. M. Jorgensen, and A. E. Rougvie, *Analysis of a lin-42/period null allele implicates all three isoforms in regulation of Caenorhabditis elegans molting and developmental timing,* G3: Genes, Genomes, Genetics **6**, 4077 (2016).

[93] M. Olmedo, M. Geibel, M. Artal-Sanz, and M. Merrow, *A high-throughput method for the analysis of larval developmental phenotypes in caenorhabditis elegans,* Genetics **201**, 443 (2015).

[94] J. E. Abrahante, E. A. Miller, and A. E. Rougvie, *Identification of heterochronic mutants in caenorhabditis elegans: temporal misexpression of a collagen:: green fluorescent protein fusion gene,* Genetics **149**, 1335 (1998).

[95] J. M. Tennessen, H. F. Gardner, M. L. Volk, and A. E. Rougvie, *Novel heterochronic functions of the caenorhabditis elegans period-related protein lin-42,* Developmental biology **289**, 30 (2006).

[96] M. F. Perez, M. Francesconi, C. Hidalgo-Carcedo, and B. Lehner, *Maternal age generates phenotypic variation in caenorhabditis elegans,* Nature **552**, 106 (2017).

[97] J. W. Golden and D. L. Riddle, *The caenorhabditis elegans dauer larva: developmental effects of pheromone, food, and temperature,* Developmental biology **102**, 368 (1984).

[98] O. N. Schaedel, B. Gerisch, A. Antebi, and P. W. Sternberg, *Hormonal signal amplification mediates environmental conditions during development and controls an irreversible commitment to adulthood,* PLoS Biol **10**, e1001306 (2012).

[99] J. M. Tennessen, K. J. Opperman, and A. E. Rougvie, *The c. elegans developmental timing protein lin-42 regulates diapause in response to environmental cues,* Development **137**, 3501 (2010).

[100] W. G. Wadsworth and D. L. Riddle, *Developmental regulation of energy metabolism in caenorhabditis elegans,* Developmental biology **132**, 167 (1989).

[101] S. Cooper and C. E. Helmstetter, *Chromosome replication and the division cycle of escherichia coli br,* Journal of molecular biology **31**, 519 (1968).

[102] G. Johnston, J. Pringle, and L. H. Hartwell, *Coordination of growth with cell division in the yeast saccharomyces cerevisiae,* Experimental cell research **105**, 79 (1977).

[103] J. Mitchison and J. Creanor, *Further measurements of dna synthesis and enzyme potential during cell cycle of fission yeast schizosaccharomyces pombe,* Experimental cell research **69**, 244 (1971).

[104] L. Robert, *Size sensors in bacteria, cell cycle control, and size control,* Frontiers in microbiology **6**, 515 (2015).

[105] M. L. Begasse, M. Leaver, F. Vazquez, S. W. Grill, and A. A. Hyman, *Temperature dependence of cell division timing accounts for a shift in the thermal limits of c. elegans and c. briggsae,* Cell reports **10**, 647 (2015).

[106] J. Crapse, N. Pappireddi, M. Gupta, S. Y. Shvartsman, E. Wieschaus, and M. Wühr, *Evaluating the simple arrhenius equation for the temperature dependence of complex developmental processes,* BioRxiv (2020).

[107] S. G. Kuntz and M. B. Eisen, *Drosophila embryogenesis scales uniformly across temperature in developmentally diverse species,* PLoS Genet **10**, e1004293 (2014).

[108] J. Chong, C. Amourda, and T. E. Saunders, *Temporal development of drosophila embryos is highly robust across a wide temperature range,* Journal of The Royal Society Interface **15**, 20180304 (2018).

[109] M. Rodriguez, L. B. Snoek, M. De Bono, and J. E. Kammenga, *Worms under stress: C. elegans stress response and its relevance to complex human disease and aging,* Trends in Genetics **29**, 367 (2013).

[110] E. De Nadal, G. Ammerer, and F. Posas, *Controlling gene expression in response to stress,* Nature Reviews Genetics **12**, 833 (2011).

[111] J. P. González, O. C. Farnés, A. T. R. Vasconcelos, and A. G. Pérez, *Conservation of key members in the course of the evolution of the insulin signaling pathway,* Biosystems **95**, 7 (2009).

[112] S. T. Lamitina and K. Strange, *Transcriptional targets of daf-16 insulin signaling pathway protect C. elegans from extreme hypertonic stress,* American Journal of Physiology-Cell Physiology **288**, C467 (2005).

[113] C.-G. Zou, Q. Tu, J. Niu, X.-L. Ji, and K.-Q. Zhang, *The daf-16/foxo transcription factor functions as a regulator of epidermal innate immunity,* PLoS pathogens **9** (2013).

[114] K. D. Kimura, H. A. Tissenbaum, Y. Liu, and G. Ruvkun, *daf-2, an insulin receptor-like gene that regulates longevity and diapause in Caenorhabditis elegans,* Science **277**, 942 (1997).

[115] S. B. Pierce, M. Costa, R. Wisotzkey, S. Devadhar, S. A. Homburger, A. R. Buchman, K. C. Ferguson, J. Heller, D. M. Platt, A. A. Pasquinelli, *et al.*, *Regulation of daf-2 receptor signaling by human insulin and ins-1, a member of the unusually large and diverse C. elegans insulin gene family,* Genes & development **15**, 672 (2001).

[116] C. T. Murphy, S.-J. Lee, and C. Kenyon, *Tissue entrainment by feedback regulation of insulin gene expression in the endoderm of Caenorhabditis elegans,* Proceedings of the National Academy of Sciences **104**, 19046 (2007).

[117] A. D. Ritter, Y. Shen, J. F. Bass, S. Jeyaraj, B. Deplancke, A. Mukhopadhyay, J. Xu, M. Driscoll, H. A. Tissenbaum, and A. J. Walhout, *Complex expression dynamics and robustness in C. elegans insulin networks,* Genome research **23**, 954 (2013).

[118] K. Lin, J. B. Dorman, A. Rodan, and C. Kenyon, *daf-16: An hnf-3/forkhead family member that can function to double the life-span of Caenorhabditis elegans,* Science **278**, 1319 (1997).

[119] S. Ogg, S. Paradis, S. Gottlieb, G. I. Patterson, L. Lee, H. A. Tissenbaum, and G. Ruvkun, *The fork head transcription factor daf-16 transduces insulin-like metabolic and longevity signals in C. elegans,* Nature **389**, 994 (1997).

[120] K. Lin, H. Hsin, N. Libina, and C. Kenyon, *Regulation of the Caenorhabditis elegans longevity protein daf-16 by insulin/igf-1 and germline signaling,* Nature genetics **28**, 139 (2001).

[121] C. M. Cahill, G. Tzivion, N. Nasrin, S. Ogg, J. Dore, G. Ruvkun, and M. Alexander-Bridges, *Phosphatidylinositol 3-kinase signaling inhibits daf-16 dna binding and function via 14-3-3-dependent and 14-3-3-independent pathways,* Journal of Biological Chemistry **276**, 13402 (2001).

[122] S. T. Henderson and T. E. Johnson, *daf-16 integrates developmental and environmental inputs to mediate aging in the nematode Caenorhabditis elegans,* Current Biology **11**, 1975 (2001).

[123] T. Furuyama, T. NAKAZAWA, I. NAKANO, and N. MORI, *Identification of the differential distribution patterns of mrnas and consensus binding sequences for mouse daf-16 homologues,* Biochemical Journal **349**, 629 (2000).

[124] N. O. Burton, T. Furuta, A. K. Webster, R. E. Kaplan, L. R. Baugh, S. Arur, and H. R. Horvitz, *Insulin-like signalling to the maternal germline controls progeny response to osmotic stress,* Nature cell biology **19**, 252 (2017).

[125] J. Li, A. Ebata, Y. Dong, G. Rizki, T. Iwata, and S. S. Lee, *Caenorhabditis elegans hcf-1 functions in longevity maintenance as a daf-16 regulator,* PLoS Biol **6**, e233 (2008).

[126] M. A. Essers, L. M. de Vries-Smits, N. Barker, P. E. Polderman, B. M. Burgering, and H. C. Korswagen, *Functional interaction between ß-catenin and foxo in oxidative stress signaling,* Science **308**, 1181 (2005).

[127] R. G. Tepper, J. Ashraf, R. Kaletsky, G. Kleemann, C. T. Murphy, and H. J. Bussemaker, *Pqm-1 complements daf-16 as a key transcriptional regulator of daf-2-mediated development and longevity,* Cell **154**, 676 (2013).

[128] A. Bansal, E.-S. Kwon, D. Conte, H. Liu, M. J. Gilchrist, L. T. MacNeil, and H. A. Tissenbaum, *Transcriptional regulation of caenorhabditis elegansfoxo/daf-16 modulates lifespan,* Longevity & healthspan **3**, 5 (2014).

[129] D. Weinkove, J. R. Halstead, D. Gems, and N. Divecha, *Long-term starvation and ageing induce age-1/pi 3-kinase-dependent translocation of daf-16/foxo to the cytoplasm,* BMC biology **4**, 1 (2006).

[130] N. Libina, J. R. Berman, and C. Kenyon, *Tissue-specific activities of c. elegans daf-16 in the regulation of lifespan,* Cell **115**, 489 (2003).

[131] D. S. Patel, A. Garza-Garcia, M. Nanji, J. J. McElwee, D. Ackerman, P. C. Driscoll, and D. Gems, *Clustering of genetically defined allele classes in the caenorhabditis elegans daf-2 insulin/igf-1 receptor,* Genetics **178**, 931 (2008).

[132] H. Shankaran, D. L. Ippolito, W. B. Chrisler, H. Resat, N. Bollinger, L. K. Opresko, and H. S. Wiley, *Rapid and sustained nuclear–cytoplasmic erk oscillations induced by epidermal growth factor,* Molecular systems biology **5**, 332 (2009).

[133] S. Tay, J. J. Hughey, T. K. Lee, T. Lipniacki, S. R. Quake, and M. W. Covert, *Single-cell nf-κb dynamics reveal digital activation and analogue information processing,* Nature **466**, 267 (2010).

[134] J. C. Locke, J. W. Young, M. Fontes, M. J. H. Jiménez, and M. B. Elowitz, *Stochastic pulse regulation in bacterial stress response,* science **334**, 366 (2011).

[135] N. Hao and E. K. O'shea, *Signal-dependent dynamics of transcription factor translocation controls gene expression,* Nature structural & molecular biology **19**, 31 (2012).

[136] J. E. Purvis, K. W. Karhohs, C. Mock, E. Batchelor, A. Loewer, and G. Lahav, *p53 dynamics control cell fate,* Science **336**, 1440 (2012).

[137] N. Yissachar, T. S. Fischler, A. A. Cohen, S. Reich-Zeliger, D. Russ, E. Shifrut, Z. Porat, and N. Friedman, *Dynamic response diversity of nfat isoforms in individual living cells,* Molecular cell **49**, 322 (2013).

[138] J. H. Levine, Y. Lin, and M. B. Elowitz, *Functional roles of pulsing in genetic circuits,* Science **342**, 1193 (2013).

[139] S. T. Lamitina, R. Morrison, G. W. Moeckel, and K. Strange, *Adaptation of the nematode Caenorhabditis elegans to extreme osmotic stress,* American Journal of Physiology-Cell Physiology **286**, C785 (2004).

[140] T. Lamitina, C. G. Huang, and K. Strange, *Genome-wide rnai screening identifies protein damage as a regulator of osmoprotective gene expression,* Proceedings of the National Academy of Sciences **103**, 12173 (2006).

[141] S. K. Olson, G. Greenan, A. Desai, T. Müller-Reichert, and K. Oegema, *Hierarchical assembly of the eggshell and permeability barrier in c. elegans,* Journal of Cell Biology **198**, 731 (2012).

[142] A. F. Bird and J. Bird, *The structure of nematodes* (Academic Press, 2012).

[143] U. Aghayeva, A. Bhattacharya, and O. Hobert, *A panel of fluorophore-tagged daf-16 alleles,* microPublication Biology **2020** (2020).

[144] K. Hesp, G. Smant, and J. E. Kammenga, *Caenorhabditis elegans daf-16/foxo transcription factor and its mammalian homologs associate with age-related disease,* Experimental gerontology **72**, 1 (2015).

[145] C. T. Murphy, S. A. McCarroll, C. I. Bargmann, A. Fraser, R. S. Kamath, J. Ahringer, H. Li, and C. Kenyon, *Genes that act downstream of daf-16 to influence the lifespan of Caenorhabditis elegans,* Nature **424**, 277 (2003).

[146] Y. Matsunaga and T. Kawano, *The C. elegans insulin-like peptides (ilps),* AIMS Biophysics **5**, 217 (2018).

[147] A. Cornils, M. Gloeck, Z. Chen, Y. Zhang, and J. Alcedo, *Specific insulin-like peptides encode sensory information to regulate distinct developmental processes,* Development **138**, 1183 (2011).

[148] J. N. Landis and C. T. Murphy, *Integration of diverse inputs in the regulation of caenorhabditis elegans daf-16/foxo,* Developmental dynamics: an official publication of the American Association of Anatomists **239**, 1405 (2010).

[149] L. Ashall, C. A. Horton, D. E. Nelson, P. Paszek, C. V. Harper, K. Sillitoe, S. Ryan, D. G. Spiller, J. F. Unitt, D. S. Broomhead, *et al.*, *Pulsatile stimulation determines timing and specificity of nf-κb-dependent transcription,* Science **324**, 242 (2009).

[150] A. S. Hansen and E. K. O'shea, *Promoter decoding of transcription factor dynamics involves a trade-off between noise and control of gene expression,* Molecular systems biology **9** (2013).

[151] J. E. Purvis and G. Lahav, *Encoding and decoding cellular information through signaling dynamics,* Cell **152**, 945 (2013).

[152] S. L. Rea, D. Wu, J. R. Cypser, J. W. Vaupel, and T. E. Johnson, *A stress-sensitive reporter predicts longevity in isogenic populations of caenorhabditis elegans,* Nature genetics **37**, 894 (2005).

[153] M. O. Casanueva, A. Burga, and B. Lehner, *Fitness trade-offs and environmentally induced mutation buffering in isogenic c. elegans,* Science **335**, 82 (2012).

[154] S. Bjorklund and L. Ljung, *A review of time-delay estimation techniques,* in *42nd IEEE International Conference on Decision and Control (IEEE Cat. No. 03CH37475),* Vol. 3 (IEEE, 2003) pp. 2502–2507.

[155] B. M. Peterson, I. Wanders, K. Horne, S. Collier, T. Alexander, S. Kaspi, and D. Maoz, *On uncertainties in cross-correlation lags and the reality of wavelength-dependent continuum lags in active galactic nuclei,* Publications of the Astronomical Society of the Pacific **110**, 660 (1998).

SUMMARY

Multicellular development is a sequence of genetically programmed, intricately linked micro- and macroscopic events that start from a single cell - zygote - and lead to the formation of a functional individual, primed for survival and reproduction. All developmental events, from gene expression to cell division, differentiation and migration, as well as tissue and organ formation, have to follow a precise temporal and spatial order, as the smallest mistake can be detrimental. Development is remarkably reproducible, despite occurring under a wide variety of environmental conditions, such as nutrient availability and temperature, and being subject to a substantial amount of molecular noise. In this thesis, we use the nematode worm *Caenorabditis elegans* as a model system to investigate i) how the timing of development adjusts to changes in the outside world and ii) how organisms respond to external stresses that do not support normal developmental progression. *C. elegans* is an ideal model organism to address these questions, due to its simplicity, stereotypical developmental pattern and the vast extent to which its biology and genetics are known.

While studying *C. elegans* embryonic development is relatively straightforward, post-embryonic development presents a challenge to imaging as animals move around in order to feed. The lack of reliable long-term time-lapse microscopy techniques thus precluded the progress on studying many developmental processes in individual animals. In **Chapter 2** we introduce a time-lapse microscopy technique that allows following the full (post-)embryonic development of individual *C. elegans* larvae at single cell resolution. By placing single embryos inside microfabricated chambers, it is possible to apply controlled environments, including food, osmolarity or temperature. Fast image acquisition coupled with (semi-) automated image analysis then allows monitoring single cells inside the motile, normally developing larvae. This setup allows us to monitor tens of individual worms in parallel under identical conditions, which enables the investigation of processes and events that are not accessible by population studies. We further show two proof-of-principle examples that were technically challenging with previous approaches: studying the dynamics of oscillatory gene expression as well as the timing of cell divisions to obtain detailed lineages in individual animals. In subsequent chapters we use this time-lapse microscopy technique to address relevant questions in the fields of *C. elegans* development and stress response.

In spite of large variations in size, organisms maintain proportion through spatial scaling, where spatial patterns of gene expression scale with the size of the organ or embryo. As shown in **Chapter 3**, we now find that the concept of scaling also extends to the time dimension of development. We show that different individuals, while genetically identical and exposed to the same conditions, exhibit variability in their developmental progression but, remarkably, the relative timing of individual developmental events is preserved. Temporal scaling is even more evident when development is prolonged externally by changing the environmental conditions, such as

temperature and diet. Notably, temporal scaling is also observed in *lin-42/Period* mutants, in which developmental timing is strongly perturbed. Overall, these findings indicate that temporal scaling is a key strategy to maintain correct developmental timing under diverse conditions.

Larval development of *C. elegans* arrests at particular developmental checkpoints under conditions of environmental stress, such as starvation, osmotic shock and high temperature. An important mediator of these arrests is the highly conserved insulin/insulin-like growth factor-1 (IIS) pathway. This pathway not only induces arrests, but also mounts a protective response that is specific to different stresses, through proteins called transcription factors that turn many genes on or off as a response to stress. In **Chapter 4**, we study how the IIS pathway can discriminate between different stresses (starvation, heat or osmotic stress) to mount a tailored response, under conditions that result in developmental arrest in the L1 larval stage. The current view, based on population studies and static images, proposes that DAF-16, the major transcription factor involved in stress response and a key output of the IIS pathway, is localized in the cytoplasm during normal developmental conditions and translocates to the nucleus during stress. However, this model does not explain how a single pathway can discriminate between stresses. Our time-lapse microscopy technique enabled DAF-16 protein dynamics to be imaged for the first time in single animals, revealing an unexpected observation. Upon exposure to a constant level of stress, DAF-16 exhibits complex localization dynamics, shuttling back and forth between the nucleus and the cytoplasm in a pulsatile fashion. Pulse characteristics are different for diverse types and magnitudes of stress, suggesting a potential mechanism to discriminate between stresses in order to enable differential gene expression. Notably, DAF-16 pulses are highly synchronized among cells along the body, with a short anterior-posterior delay that suggests the presence of a synchronization signal that moves through the body. Finally, we show that the DAF-16 homolog FOXO3a exhibits pulsatile dynamics in mammalian cells at low nutrient levels, suggesting that DAF-16/FOXO translocation pulses are a general and so far unrecognized feature of insulin signalling.

SAMENVATTING

Meercellige ontwikkeling is een opeenvolging van genetisch geprogrammeerde, nauw met elkaar verbonden micro- en macroscopische gebeurtenissen die beginnen met een enkele cel – de zygote - en leiden tot de vorming van een functioneel individu, dat in staat is om te overleven en zich voort te planten. Alle ontwikkelingsprocessen, van genexpressie tot celdeling, differentiatie en migratie, evenals weefsel- en orgaanvorming, moeten een precieze temporele en ruimtelijke orde volgen, omdat de kleinste fout al schadelijk kan zijn. Ontwikkeling is opmerkelijk reproduceerbaar, gezien het feit dat het plaatsvindt onder een grote verscheidenheid aan omgevingscondities, zoals de beschikbaarheid van voedingsstoffen en temperatuur, en onderhevig is aan een aanzienlijke hoeveelheid moleculaire ruis. In dit proefschrift gebruiken we de nematode worm *Caenorabditis elegans* als modelsysteem om te onderzoeken: i) hoe de timing van ontwikkeling zich aanpast aan veranderingen in de buitenwereld en ii) hoe organismen reageren op externe stressoren die normale ontwikkeling verhinderen. *C. elegans* is een ideaal modelorganisme om deze vragen aan te pakken, vanwege zijn eenvoud, stereotype ontwikkelingspatroon en de grote mate waarin zijn biologie en genetica bekend zijn.

Terwijl het bestuderen van de embryonale ontwikkeling van *C. elegans* relatief eenvoudig is, vormt de postembryonale ontwikkeling een uitdaging voor het maken van microscopische afbeeldingen omdat de larven zich verplaatsen om zich te voeden. Het resulterende gebrek aan technieken om over lange perioden time-lapse microscopie te bedrijven maakte het daarom onmogelijk om veel van de ontwikkelingsprocessen in individuele larven te bestuderen. In **Hoofdstuk 2** introduceren we een time-lapse microscopietechniek die het mogelijk maakt om de volledige (post-)embryonale ontwikkeling van individuele *C. elegans* larven met enkele-cel resolutie te volgen. Door het plaatsen van individuele embryo's in gemicrofabriceerde kamertjes is het mogelijk om de omgevingscondities, zoals voedsel, osmolariteit of temperatuur, nauwkeurig te controleren. Snelle beeldregistratie in combinatie met (semi-) geautomatiseerde beeldanalyse maakt dan het observeren van enkele cellen in vrij bewegende en zich normaal ontwikkelende larven mogelijk. Deze opstelling stelt ons in staat om in parallel tientallen individuele wormen onder identieke omstandigheden te observeren, wat het mogelijk maakt om processen en gebeurtenissen te onderzoeken die niet toegankelijk zijn voor populatiestudies. Als voorbeeld, onderzochten wij twee processen, die met tot nu toe technisch ingewikkeld waren om te bestuderen: het meten van dynamiek van de oscillerende genexpressie en van de timing van celdelingen om hiervan gedetailleerde stambomen in individuele dieren te verkrijgen. In de daaropvolgende hoofdstukken gebruiken we deze time-lapse microscopietechniek om belangrijke vragen op het gebied van de ontwikkeling van *C. elegans* en stressrespons aan de orde te stellen.

Ondanks grote variaties in grootte, behouden organismen de juiste verhoudingen door middel van ruimtelijke schaling, waarbij ruimtelijke patronen van genexpressie schalen met de grootte van het orgaan of embryo. Zoals blijkt uit **Hoofdstuk 3**, vinden we nu dat het concept van schaalvergroting zich ook uitstrekt tot de tijdsdimensie van de ontwikkeling. We laten zien dat verschillende individuen, hoewel genetisch identiek en blootgesteld aan dezelfde omstandigheden, variabiliteit vertonen in het tempo van hun ontwikkeling, maar opmerkelijk genoeg blijft de relatieve timing van de individuele ontwikkelingsgebeurtenissen behouden. Temporele schaling is nog duidelijker wanneer de ontwikkeling extern wordt verlengd door de omgevingscondities, zoals temperatuur en dieet, te veranderen. Verrassend genoeg wordt temporele schaling ook waargenomen bij *lin-42/Period* mutanten, waarbij de ontwikkelingstiming sterk verstoord is. Over het algemeen geven deze bevindingen aan dat temporele schaling een belangrijke strategie is om de juiste ontwikkelingstiming te handhaven onder uiteenlopende omstandigheden.

De larvale ontwikkeling van *C. elegans* kan onder omstandigheden van omgevingsstress, zoals verhongering, osmotische shock en hoge temperatuur, op heel specifieke controlepunten worden stilgezet. Een belangrijke intermediar van dit soort ontwikkelingspauzes is de evolutionair sterk behouden insuline/IGF-1 (IIS) signaalsysteem. Dit signaalsysteem induceert niet alleen ontwikkelingspauzes, maar zet ook een beschermende respons op die specifiek is voor de verschillende stressoren, door middel van eiwitten die transcriptiefactoren worden genoemd en die vele genen aan- of uitzetten als reactie op stress. In **Hoofdstuk 4** bestuderen we hoe de IIS pathway een onderscheid kan maken tussen verschillende spanningen (voedselgebrek, hitte of osmotische stress) om een op maat gemaakte respons te genereren, onder omstandigheden die resulteren in ontwikkelingsstilstand in het L1 larvale stadium. In de bestaande visie, die gebaseerd is op populatiestudies en statische beelden, gaat DAF-16, de belangrijkste transcriptiefactor die betrokken is bij stressrespons en een belangrijke output van de IIS pathway, van het cytoplasma, waar het zich bevindt tijdens normale ontwikkelingscondities, over naar de celkern als gevolg van stress, in een process dat „translocatie“ wordt genoemd. Dit model verklaart echter niet hoe één enkel signaalsysteem een onderscheid kan maken tussen verschillende stressoren. Onze time-lapse microscopietechniek maakte het mogelijk om de dynamica van DAF-16 translocatie voor het eerst in beeld te brengen in individuele larven, met een verrassende observatie tot gevolg. Bij blootstelling aan een constant stressniveau vertoont DAF-16 een complexe translocatiedynamiek, waarbij het op een pulserende manier heen en weer pendelt tussen de celkern en het cytoplasma. De pulsdynamica vertoont bovendien karakteristieken die specifiek zijn voor de verschillende soorten en sterkten van stress en suggereert daarmee een potentieel mechanisme om onderscheid te maken tussen stressoren en daarmee de juiste genexpressierespons mogelijk te maken. Verrassend genoeg zijn de DAF-16 pulsen sterk gesynchroniseerd tussen cellen die op verschillende plekken in het lichaam zijn verspreid, met een korte vertraging tussen de cellen dichterbij het hoofd en die dichter bij de staart die de aanwezigheid suggereert van een synchronisatiesignaal dat door het lichaam beweegt. Tot slot tonen we aan dat de DAF-16 homoloog FOXO3 ook dynamische pulsen vertoont in zoogdiercellen bij lage nutriëntenniveaus, wat suggereert dat DAF-16/FOXO translocatiepulsen een algemeen, en tot nu toe niet herkend, kenmerk zijn van insulinesignalering.

ABOUT THE AUTHOR

Olga Filina was born in Petrozavodsk, Soviet Union (present day Russia), on April 5, 1990. In 2012 she obtained her Bachelor's degree in Engeneering and Technology from Saint Petersburg National Research University of Information Technologies, Mechanics and Optics. During her Bachelor's studies, she worked at the Institute for Analytical Instrumentation of the Russian Academy of Sciences under the supervision of Dr. Anatoly Evstrapov, where she researched processes and methods for polymer material sealing of microfluidic devices.

She then went to Germany to join the Master's program in Nanobiophysics at the Technische Universität Dresden, and obtained her Master of Science degree in 2014. During these studies, she carried out research at the Max Planck Institute of Molecular Cell Biology and Genetics, under the supervision of Dr. Gaia Pigino. Her project involved 3D structural analysis of eukaryotic flagellar components, by means of transmission electron microscopy and computational techniques.

Thereafter, she did an internship at the Vrije Universiteit Amsterdam in the group of Prof. Dr. Gijs J.L. Wuite, where she performed a single-molecule study of RNA polymerase combining optical tweezers and confocal fluorescence microscopy.

Finally, in 2015 she started her PhD at AMOLF under the supervision of Dr. Jeroen van Zon, which resulted in the work presented here.

LIST OF PUBLICATIONS

RELATED TO THIS THESIS

N. Gritti, S. Kienle, **O. Filina**, J.S. van Zon. (2016) *Long-term time-lapse microscopy of C. elegans post-embryonic development,* Nature Communications **7.1**: 1-9. (Chapter 2)

O. Filina, R. Haagmans, J.S. van Zon. *Temporal scaling in C. elegans larval development,* bioRxiv (2020). (Chapter 3)

O. Filina, B. Demirbas, M.A. Sánchez-Romero, M. Olmedo, J.S. van Zon. *Stress discrimination by body-wide, stochastic DAF-16/FoxO nuclear translocation pulses,* in preparation. (Chapter 4)

ACKNOWLEDGEMENTS

In this section I would like to express my gratitude towards various people that played a significant role during my PhD years at AMOLF. First of all, Jeroen, thank you for putting your trust in me and giving me the opportunity to be a part of your group. I honestly could not have wished for a better supervisor. You gave me the perfect balance between careful guidance and freedom to focus on what I like. I am truly inspired by your passion for science, which shows up in even the most casual conversations. You are also my role model for achieving a healthy work-life balance. Gijsje, thank you so much for taking up the role of my official promotor, giving me precious feedback on our yearly meetings and, of course, with the thesis. I am honored to be the first PhD student to graduate at the TU Delft under your supervision.

Some of the work presented in this thesis would not have been possible without our collaborators. María and M. Toñi, thank you for the many scientific discussions, for your priceless input into the project and for taking good care of us in Sevilla. I am also very grateful to all the committee members for taking their time to read and assess this dissertation and to participate in the ceremony.

Big thanks go to my dear paranymphs and close friends – Federica and Nicola. Thank you both for your time and effort to support me with various arrangements and preparations for the defense. I am looking forward to celebrating it with you. Fede, I feel like I have known you for ages. Thanks for being such a good friend who always notices when something is wrong and is willing to listen and give advice. I admire your passion for adventure and your talent in making every person in the room feel included. Nicola, I am lucky to have found a great friend in a fellow group member. Thank you for teaching me pretty much everything at the beginning of my PhD, for all the coffees we've had on the wooden bench next to AMOLF, sharing frustrations about failed experiments, for numerous conversations, parties, dinners and trips, for patiently standing my jokes, and for sneaking into my family album.

I would like to extend these acknowledgements to other past and present members of Quantitative Developmental Biology group. Simone, I have always enjoyed your company and the gatherings you organized. Thank you for trusting me with little Bao, I loved seeing you two on your morning walk from my window. Joleen, you are such a sweet and interesting person. I really enjoyed our time in USA, wandering through the streets of Boston, living the campus life in Fort Collins, and escaping the conference in L.A. to see Hollywood (sorry, Jeroen). Yvonne, thank you for your invaluable help in the lab and for many fun evenings we've had in the old Polder (those were good times!). Guizela, thank you for your friendliness and for always giving constructive feedback at group meetings. Burak and Timo, though we only overlapped shortly at AMOLF, I enjoyed working together and I am confident that the DAF-16 project is in good hands. Thank you for all the useful discussions. Also, special thanks to Timo for helping me distribute the books. Jason, Rutger and Xuan, it was really nice to have you as colleagues and I hope we stay in touch. I would also like to mention the talented Master students who I had a pleasure to work with during these years - Rayan, Rik and Muriel, as well as other students that enriched our group for brief periods of time, especially Jessica, Ana and Eleonora.

During these years I met a great deal of wonderful people, who have been absolutely essential to my overall PhD experience. Agata, your radiant energy, optimism and loud voice that can be heard from the other side of the building have brightened many boring days. Thank you for always remembering to write, for warming me up in a cold tent in the tundra and for your genuine interest in Ariadna. Laura, Olesia, Moritz and Thijs, I feel lucky to have had such wonderful neighbours and friends. I have greatly enjoyed our breakfast&parenthood club. Let's keep it up in the future, in spite of the distance! Giulia and Judith, your place has always been the hub for fun parties, delicious Italian food and lots of wine. I'm happy I got to know you both! Celine, you are an extremely kind and joyful person, and I wish you to remain that way in spite of whatever life brings you. Marco, I still remember our rotten shark eating adventure in Iceland, as well as the fun we had playing code names. We certainly share a passion for remote northern places. Good luck exploring Sweden with Aliona and hope to meet you guys many more times in the future! Mathijs, you are a kind and inquisitive person, and I would love to see where these qualities take you. Parisa, I always have great fun in your company and I'm happy we will soon again live in the same city. Jenny, thank you for being such a sunshine and always dragging people out to the dance floor.

I would love to write a little bit about every single person in the following list, but in view of time and space, I would just say big thanks to Fatemeh, Noreen, Yuval, Aditya I., Sebastian, Martijn, Joris, Johannes, Florian W., Ercag, Steffen, Douwe, Kevin, Alessandro, Masha, Cristina S., Cristina M.T., Lukas, Carolyn, Iarik, Sergey, Ad, Vanda. Also, thanks to Victor, Elena, Nastya and the rest of the Nanobio crew, as well as Yana, Yulia, Vasia, Vania, Andrei and many others.

Last but not least, some very special people deserve to be mentioned here. Mario, your endless support allowed me to go through the most difficult times. You know everything yourself, so I will keep it short. Thank you for taking such good care of me and our little girl, for our enriching conversations, for being my personal Python teacher, for a daily dose of random facts, and for always reminding me that the glass is half full. Ariadna, you challenged me in so many ways but, at the same time, made me believe that everything is possible. I am extremely grateful for that. Мои дорогие папа и Наташа, спасибо вам за поддержку и веру в меня. Мама, из всех людей на Земле ты гордилась бы мной больше всего. Твоя безграничная любовь навсегда в моём сердце.